Enhanced Subsea Acoustically Aided Inertial Navigation

Jørgensen, Martin Juhl

Publication date:
2016

Document Version
Publisher's PDF, also known as Version of record

Enhanced Subsea Acoustically Aided Inertial Navigation

Martin Juhl Jørgensen

Kongens Lyngby 2015
PHD-2015-392

Technical University of Denmark
Department of Applied Mathematics and Computer Science
Richard Petersens Plads, building 324,
2800 Kongens Lyngby, Denmark
Phone +45 4525 3031
compute@compute.dtu.dk
www.compute.dtu.dk PHD-2015-392

Summary (English)

This thesis deals with enhancing state-of-the-art underwater acoustic–inertial navigation systems that are necessary for deep water robotic operations. Throughout the project intelligent and simple operational solutions to complex real-world problems was emphasized.

Offshore hydrocarbon, oil and gas, exploration is advancing further into treacherous territories such as deeper waters and arctic region. Deep underwater navigation poses a deluge of challenges; there is no such luxury as Global Navigation Satellite Systems (GNSS) underwater. Many of these challenges have been solved, but vessel time is expensive so lots of effort is put into cutting down on time spent on all tasks. Accuracy demanding tasks such as subsea construction and surveying are subject to strict quality control requirements taking up a lot of time. Offshore equipment is rugged and sturdy as the environmental conditions are harsh, likewise should the use of it be simple and robust to ensure that it actually works.

The contributions of this thesis are all focused on enhancing accuracy and time efficiency while bearing operational reliability and complexity strongly in mind. The basis of inertial navigation, the inertial sensors are treated in a calibration study with three scenarios: factory, in-field and at-sea calibration. Factory calibration compensates for sensor misalignments during the manufacturing process and for intrinsic sensor biases etc. For calibration a precise two-axis turn-table is required. It is shown that long-term effects on inertial sensors can be calibrated and assessed in-field, on land without specialized equipment, or at sea with certain realistic limitations and assumptions.

Automatic calibration of complex multi-sensor acoustic-inertial navigation systems, using parameter estimation, is employed on unprecedented high dynamic trajectories collected from sea-trials. These are needed to increase navigation accuracy to the cm-level and beyond. The same techniques can also be used for regular navigation in order to minimize both time and human error in parameter measurements.

In a unifying *litmus test*, the entire body of work is applied in a novel and potentially revolutionary methodology for the most challenging of all subsea survey and construction tasks: spool piece and jumper metrology. Two distinct approaches are investigated: One seeks to eliminate acoustic seabed transponders, but keep transponders at desired survey points; the other uses a mapping sensor such as subsea lidar to simply map the area in question. Both approaches are shown to work in practice. Generating high resolution maps, as the latter approach, is how the author anticipates all subsea surveys will be conducted in the near future.

Resumé (Danish)

Denne afhandling beskæftiger sig med at forbedre avanceret akustisk-inertial undervandsnavigationsystemer, nødvendige for aktiviteter på dybt vand. Igennem projektet har der været lagt vægt på intelligente og simple operationelle løsninger på problemstillinger fra den virkelige verden.

Offshore kulbrinteudvinding bevæger sig ind på udfordrende territorier som dybt hav og arktiske egne. Undervandsnavigation i dybet medfører en overflod af udfordringer, f.eks. er der ingen luksus som GNSS under havoverfladen. Mange af disse udfordringer er løst, men skibstid er kostbart så derfor bestræber meget af arbejdet sig på at reducere den anvendte tid på tværs af alle relaterede opgaver. Nøjagtighedskrævende opgaver som undervandskonstruktion og -opmåling er underlagt strenge kvalitetssikringskrav der tager meget tid. Offshore materiel er robust og solidt da arbejdsmiljøet er barskt, ligeledes burde brugen heraf være lige til og robust for at sikre at det virker i praksis.

Bidragene fra afhandlingen er alle fokuseret på at forbedre navigationsnøjagtighed og tidseffektivitet, med operationel pålidelighed og kompleksitet i mente. Fundamentet for inertial navigation, inertial sensorerne, bliver behandlet i et kalibreringsstudie i tre scenarier: fabriks-, felt- og "til søs"-kalibrering. Fabrikskalibrering kompenserer sensor skævheder introduceret ved produktionen og for indre sensorfejl som bias. Kalibreringen kræver et to-akset præcisions rotationsbord. Det bliver vist at langsigtede fejl på inertial sensorerne kan kalibreres og evalueres i felten, på land uden specialiseret udstyr, eller til søs med realistiske begrænsninger og antagelser.

Automatisk kalibrering af komplicerede multisensor akustisk-inertial naviga-

tionsystemer ved brug af parameterestimering, bliver anvendt på hidtil uset højdynamiske navigations data indsamlet fra havforsøg. Dette er nødvendigt for at forøge navigationsnøjagtigheden til cm-niveau og hinsides. Samme teknik kan også bruges til regulær navigation for at mindske både tid og menneskelige fejl involveret i opmåling af parametrene.

I en samlet litmusprøve bliver hoveddelen af arbejdet anvendt i en ny og potentielt revolutionerende metodologi på det mest udfordrende af alle undervandsopmålings og -konstruktions opgaver: "spool piece" og "jumper" undervandsmetrologi. To forskellige tilgange er undersøgt: den første metode reducerer antallet af akustiske transponderer ved brug af akustisk inertial navigation; den anden metode benytter sig af en kortlægningssensor, f.eks. en lidar, til at kortlægge området. Begge metoder vises at virke i praksis. At producere højopløselige kort, som sidstnævnte metode, ser forfatteren som værende måden hvorpå alle undervandsopmålinger vil blive udført på i den nære fremtid.

Preface

This thesis was prepared at DTU Compute in fulfillment of the requirements for the Ph.D degree. This project was supervised by associate professor Niels Kjølstad Poulsen, Ph.D., M.Sc.EE with the Section for Dynamical Systems (DYNSYS), Department of Applied Mathematics and Computer Science, the Technical University of Denmark (DTU) and co-supervised by Mikael Blikstad Larsen, Ph.D, M.Sc.EE with Sonardyne International Ltd (hereafter Sonardyne). The work was jointly funded by DTU Compute and Sonardyne.

The thesis deals with subsea navigation and specifically applications of Acoustically Aided Inertial Navigation Systems (AAINS). My introduction to the subject was given by Mikael in a guest lecture in an advanced robotic course at DTU in 2008. I later went on to spend a significant amount of my time working on AAINS with Mikael and Niels, resulting in a M.Sc. thesis about non-linear Kalman filter techniques for AAINS in 2010. By the end of 2011 funding for the Ph.D. project was in place, and I was matriculated as a Ph.D. student at DTU Compute.

The thesis consists of two parts. The first part is a summary report giving an introduction to the problem at hand, the application domain and mathematical tools, as well as stating main contributions, a conclusion and an outlook toward the future. Second part is a collection of the scientific publications produced throughout the project.

Kgs. Lyngby, 08-September-2015

Martin Juhl Jørgensen

Acknowledgements

I would like to thank my family for always supporting me, even when neither of us knew exactly what I was doing. A special thank goes out to my brother for secretly narrating my endeavors and shenanigans with robots, satellites and offshore subsea navigation to all his non-scientific friends.

I have enjoyed working with my supervisors and wish to thank them for both for many hours of discussions and amusement. Telling fellow PhD students that I shared office with my supervisor, for more than three years, tends to give them goose bumps. I can honestly say that I have truly enjoyed my time in that office, and that I see Mikael as more of a mentor for me than a traditional co-supervisor. Both when it came to sharing knowledge and experience about aided inertial navigation systems, but also about life and career choices. For that I am grateful.

A big thank you to all my current and former coworkers at DYNSYS for creating such a social and fun work environment, as well as share insights of surviving the PhD life. This is also extended to my friends from different departments and sections that I have had numerous lunch meetings with over the years.

During the project I had the opportunity to co-supervise a large number of students in special courses, B.Sc and M.Sc. projects as well as giving a few guest lectures. There is no such eyeopener as trying to answer the multitude of questions from people who thinks peculiarly different from yourself.

I would also like to thank Sonardyne for believing enough in me to help fund my PhD project, as well as all the employees I had the chance to work with over

the years, in particular the INS team—Malik Chibah, Amy Thornton, Prashant Solanki, Alan Tombs, James Barnett, James Allan, Ashley Chapman and Chris Pearce. Especially Malik, whom I have had the pleasure of working with on two offshore trials, for being my offshore tour guide and for making stuff work under tough conditions, securing data for my work. The close technical collaboration throughout the project made it possible to quickly see advances, on both sides, being beneficial.

Thanks also goes out to the Steve Etchemendy, Dave Caress, Hans Thomas, and Giancarlo Troni with the Monterey Bay Aquarium Research Institute (MBARI) for knowledge sharing and for allowing me the opportunity to join for some very interesting data collection aboard the R/V Western Flyer.

Contents

Part I

Summary Report

Chapter 1

Introduction

The offshore industry is moving activity into deeper and deeper waters, mostly in the exploration of natural resources such as oil and gas. Working in the depths of the oceans presents a number of challenges: it is pitch black, the pressure is hundreds times more than above the surface, icy cold, seawater is corrosive and absorbs high-frequency electromagnetic waves denying use of global navigation satellite systems (GNSS).

Accurate and reliable surveys are necessary for subsea construction, but in deep water where it is infeasible to send divers, options are limited. The last two decades has cemented real-time kinematic (RTK) GNSS as an easy and available technology suitable for most survey task. As GNSS is denied underwater, accurate and reliable navigation becomes a considerable challenge and one that is impossible to solve with any single sensor. Conventional diver methods are either clumsy to perform with a subsea robot or time-consuming. Acoustic positioning has been known, applied and refined for decades, but is hitting fundamental limitations for time efficient highly dynamic operations and as water depth increases.

Vessel-time is of key concern offshore; a deep water survey and construction vessel can run into several hundred thousands Euro per day. Incentively the operators seeks to minimize survey time while maintaining accuracy and reliability. Not only is the offshore industry somewhat conservative when it comes

to incorporating new technology, but the environment often limits or inhibits their usefulness. An example of such is the use of lidar for surveys. Lidars are more or less standard within land and air surveys, but only recently has there been a development and commercialization of underwater survey grade lidars.

The motivation of this PhD project is to enhance current state-of-the-art navigation systems in terms of accuracy, robustness, time efficiency and practicality. Common demanding underwater survey applications are examined and improvements and methods are developed based on plenty of data from various trials, including two advanced sea-trials that the author participated in during the project.

1.1 Defining navigation

Defining the term *navigation* in this context is necessary in order to not cause confusion. Different professions and fields each have their own definition. The traditional maritime navigation task has been *getting from point* a *to point* b, which was the navigators job. In robotics navigation is often thought of as the answer to the questions *Where am I? Where am I going? How do I get there?*, which is solved by the navigation module. In the context of survey navigation, neither definition is precise enough.

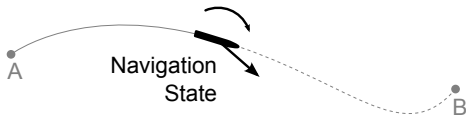

Figure 1.1: Navigation state: position, velocity and orientation (and possibly further derivatives hereof, e.g. angular rate and linear acceleration)

This thesis adopts the modern engineering definition, which originated from the field of aerospace engineering. This operates with the terms *guidance, navigation and control* (GNC; alternatively GN&C), from [21]:

Guidance refers to the determination of the desired path of travel (the *trajectory*) from the vehicle's current location to a designated target, as well as desired changes in velocity, rotation and acceleration for following that path.

Navigation refers to the determination, at a given time, of the vehicle's 3-dimensional position, velocity and orientation (the *navigation state*). Can also include orientation rate and linear acceleration.

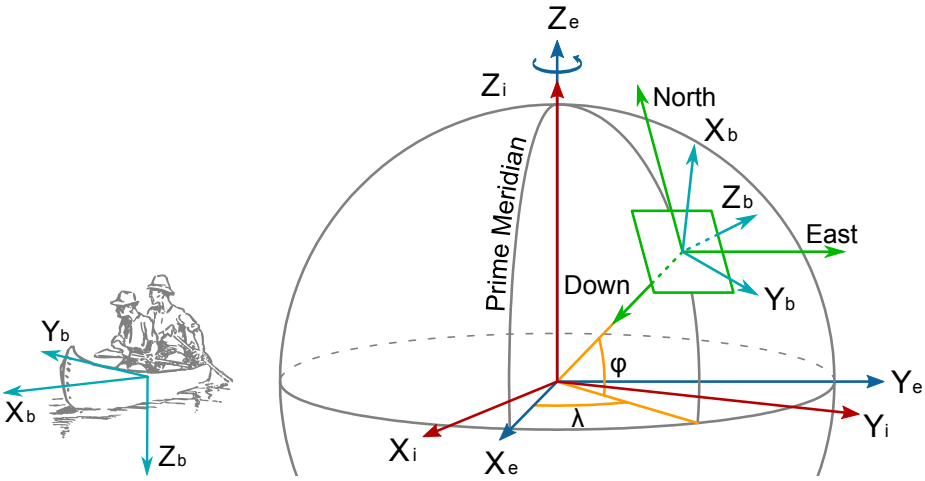

(a) Body frame coincident with a typical vehicle frame.

(b) Red is i-frame, blue is e-frame, the n-frame and the tangential plane is this green and the body frame b-frame is cyan. λ and ϕ, in orange, indicates longitude and latitude.

Figure 1.2: Reference frames typically used in inertial navigation.

Control refers to the manipulation of the forces, by way of steering controls, thrusters, etc., needed to track guidance commands while maintaining vehicle stability.

Note that given this definition, the question *Where am I going?* from robotics is not answered. This is because in robotics they also consider high-level autonomy where the robot should be able to deduce where to go given some more abstract input, e.g. *make me a milkshake*. Another peculiar note is that neither of the three functions, guidance, navigation or control is necessarily dependent on other functions. One can easily imagine a stabilizing system with no navigation, or a guidance strategy that does not rely on navigation, e.g. following colored tape on the floor[1].

1.2 Navigation frames

There are typical four different co-ordinate frames in play when mechanizing an INS. These can be divided into abstract frames and specific mechanizations, all

[1] A common strategy used by hospital and undergraduate robots alike.

which are right hand orthogonal:

i-frame The inertial frame's origin is at the inertial mass of Earth and its axes are fixed with respect to the fixed stars. This is also called an Earth-Centered Inertial (ECI) frame co-ordinate frame. A common mechanization, and the one used in this project, has the z-axis coincident with Earth's polar axis.

e-frame The Earth frame is a so-called Earth-Centered-Earth-Fixed (ECEF) co-ordinate frame which has its origin at the center of the Earth. As the axes are fixed with respect to Earth, the frame rotates at a rate $\boldsymbol{\Omega}$ with respect to or near the inertial frame. It is usually chosen so its z-axis is coinciding with Earth's polar axis and the x-axis goes through the intersection of the equatorial plane and the Greenwich meridian, which makes it easy to reference latitude and longitude. In this mechanization, and given the choice of inertial frame, the rotation is only about the z-axis at a rate Ω.

n-frame When navigating relative to Earth it is convenient to have a co-ordinate frame which is local geographic, also called the navigation frame. Three common mechanizations exist: East-North-Up (ENU), North-East-Down (NED) and wander azimuth (see [5, 10, 20]). In this project the NED mechanization is chosen. In this frame the navigation data are expressed in terms of north, east and down velocities and the position is given in latitude, longitude and depth.

b-frame The Body frame represents the Inertial Measurement Unit (IMU) output frame, i.e. the frame wherein accelerometer and gyroscope measurements are sensed and expressed. In the realization of practical AAINS it is often necessary to introduce further frames, e.g. a vehicle frame. However, these can and has been omitted from this text without loss of generality of the principles described. In this project it is defined by the x-axis pointing toward the front (fore), y-axis to the right side (starboard) and the z-axis downwards, as shown in Fig. 1.2a.

The choice of reference frames is application specific, but typical reference frames are shown in Fig. 1.2. Often it is convenient to choose a certain frame, both for deriving the mathematics, but also for the application. Sometimes it is just not feasible to choose a specific frame: going to mars is not the same problem as exploring the Mariana Trench.

Superscripts attached to vectors and matrices denote the reference frame in which the vector is belongs, e.g. $\boldsymbol{\omega}_{\text{ie}}^{\text{n}}$ is the e-frame's rotation (Earth's rotation) with respect to the inertial frame, expressed in navigation frame co-ordinates.

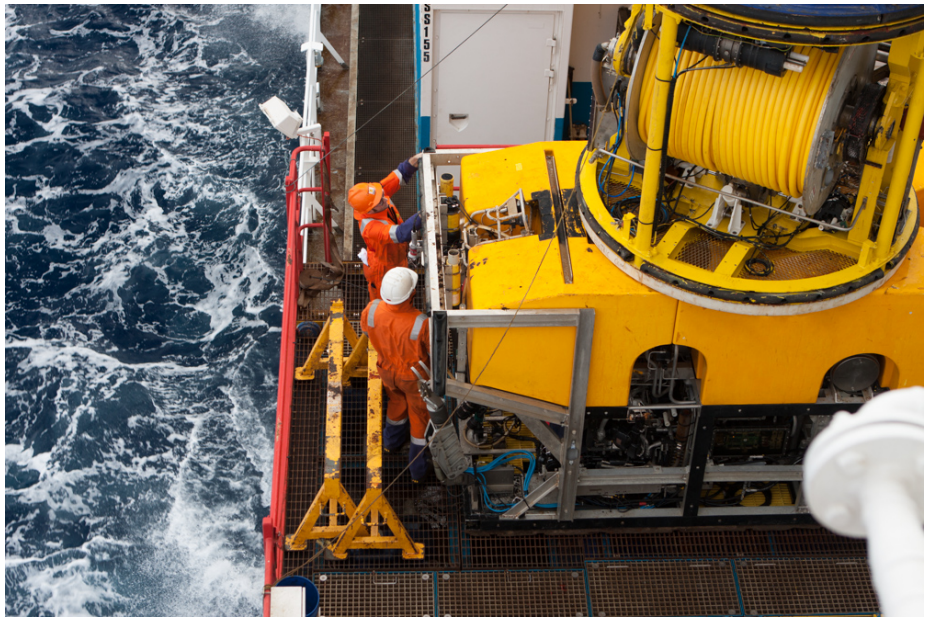

Figure 1.3: ROV pilots working on the ROV

1.3 Underwater robots

Underwater survey robots can be divided into two main categories: Remotely Operated Vehicles (ROV) and Autonomous Underwater Vehicles (AUV).

ROVs are normally tethered, providing power and a fast data link, with video streams allowing the human operators to see what they are doing. Fiber optics are commonly used as data link. Work-class ROVs have one or more manipulator arms fitted to carry out subsea work, and for the same reason are over-actuated in order to independently control motion along and around all three axis. Tooling, sensors, etc, are changes often on an ROV to deal with varying offshore work.

AUVs are generally smaller than ROVs and battery powered; they carry out preplanned well defined missions. While AUVs and ROVs can carry much of the same instrumentation, system integration on AUVs is much harder than for ROVs. This leads to AUVs using the same sensor suite, e.g. surveying but being optimized for that.

ROVs are typically employed for subsea survey tasks. Every offshore sur-

vey/construction vessel have at least one ROV for normal operations, i.e. non-survey tasks.

Other underwater robots with navigation requirements that merits honorable mentions: crawlers[14], tow-fish[18], remote equipment such as mining machines [6]).

1.4 Thesis Outline

The thesis is structured into two parts. Part I introduces and summarizes the scientific publications that forms the basis of the thesis. The relevant concepts for underwater navigation is presented in Chapter 2, including inertial navigation using strap-down sensors. Chapter 3 introduces the concept of sensor fusion and provides a framework for AAINS, as well as presenting estimation techniques commonly used within inertial navigation and sensor fusion, particular non-linear filters. Chapter 4 summarizes the main results of the publications. Finally Chapter 5 concludes Part I, including an outlook to the future of underwater navigation.

Part II is a collection of scientific publications:

Paper A is a paper presented at the *IEEE/ION Position, Location and Navigation Symposium - PLANS* in 2014. The topic of this paper is calibration of the inertial measurement unit at both a manufacturing level as well as without specialized on land and at sea.

Paper B is a journal article submitted to *IEEE Journal of Oceanic Engineering*. This paper introduces a new concept for determining subsea metrology baselines while maintaining the ability to quality checking the results.

Paper C is a journal article submitted to *IEEE Transactions on Robotics*. This paper presents state-of-the-art subsea navigation, approaching sub-cm level relative accuracy using wide-band acoustics.

Paper D is a journal article submitted to *IEEE Journal of Oceanic Engineering*. The paper presents initial results of subsea metrology, using a Lidar on a ROV.

Chapter 2

Concepts of Underwater Navigation

This chapter gives a short overview of current concepts used for underwater navigation, for a more comprehensive overview see [8]. Underwater navigation is 3-dimensional problem, but with a pressure depth sensor this essentially becomes a 2-dimensional problem. Given the small price tag compared to both accuracy and reduced complexity, almost[1] every subsea vehicle is equipped with one.

[1] Especially small and/or cheap vehicles may not, but those are generally not used for surveying tasks.

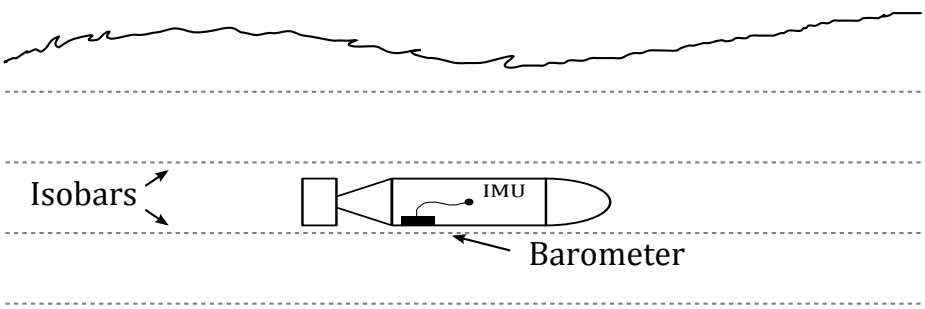

Figure 2.1: Pressure depth sensor

Due to high electromagnetic absorption, radio communication and positioning is limited to short distances—a 100 dB propagation loss alone will limit range to 3 km at 1 Hz to 1 m at 10 MHz [13]. This leaves three main categories of underwater navigation: dead reckoning, acoustic positioning and map/feature based navigation.

Real-time operation of ROVs is almost entirely done with video based human navigation. External sensors provides information to the ROV pilots, and to control systems e.g. station keeping, guidance is done from the watching the video feed. While it seems like a trivial task to implement closed-loop control systems based on reliable navigation it has yet to become industry standard. This may in part be due to a lack of trust in the robustness of the navigation sensors and in part due to by the conservatism of the industry.

2.1 Dead reckoning

Dead reckoning is a navigational technique wherein position is estimated by advancing last position with measurements or estimates of velocity and course (orientation). This integration leads to a large cumulative position error if the orientation is incorrect. Consequently dead reckoning is practically limited by the orientation uncertainty, since position error is not bounded. However, this relative navigation can be restarted at will (if permissible) or whenever a new position fix can be taken.

2.1.1 Hydrodynamic vehicle models

Kinematic vehicle models can be used for dead reckoning. This way the navigation state can be advanced based on, e.g. thrust and rudder angle or similar control inputs. Models works best if vehicle hydrodynamics are under full control such as AUVs. ROVs would require new models every time modifications are made, which in the offshore construction industry can be multiple times per day, and handle cases where the robot is dynamic, i.e. articulated arms. Vehicle models are not treated further in this thesis, but [4] serves as good introduction to hydrodynamic kinematic modeling.

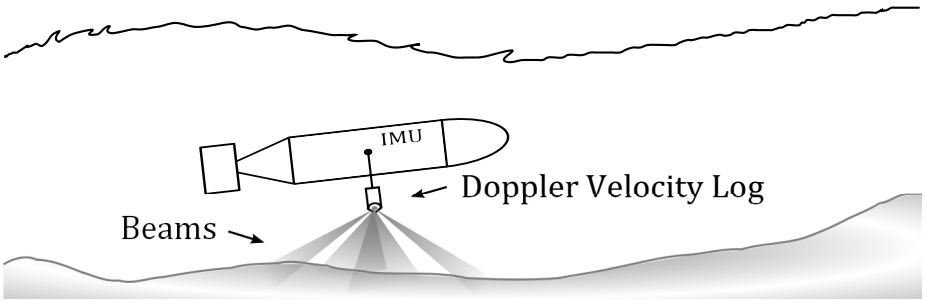

Figure 2.2: A DVL typically emits four beams which reflects of the seabed. From the acoustic scatter (Doppler shift) 3D velocity can be derived.

2.1.2 Doppler velocity log (DVL)

A DVL is an acoustic instrument that can measure its 3D velocity relative to a surface such as the seabed, ship hull or ice, or alternatively to a water layer. Most high performance DVLs use a 4-beam Janus configuration with 90 degrees between transducers in the horizontal plane, angling all transducers in the range of 30 degrees from vertical. The instrument is capable of measuring the Doppler shift of the acoustic scatter per beam. With four beam velocities the sensor velocity can be derived with a quantity commonly referred to as error velocity, which can be used to asses the observation quality. Typical long-term accuracy is often stated as $\pm 0.2\ \% \pm 0.1$ cm/s, but as error characteristics are stable this can be improved upon with careful modeling and calibration.

With a maximum altitude of 30–150 m, the DVLs are regularly used near the bottom but not during ascent/descent. While water-layer tracking is available, it is seldom the velocity relative to the water-layer, but Earth that is of interest.

DVLs can be used for high-accuracy short-term dead reckoning with a suitable attitude and heading reference system (AHRS). DVLs are commonly found on medium and up AUVs and ROVs.

Algorithms for DVL-INS based dead-reckoning have been refined in this project and the resulting systems, in operation on many commercial ROVs, routinely achieve a performance of 0.1 % distance traveled or < 3m/hr, whatever is more.

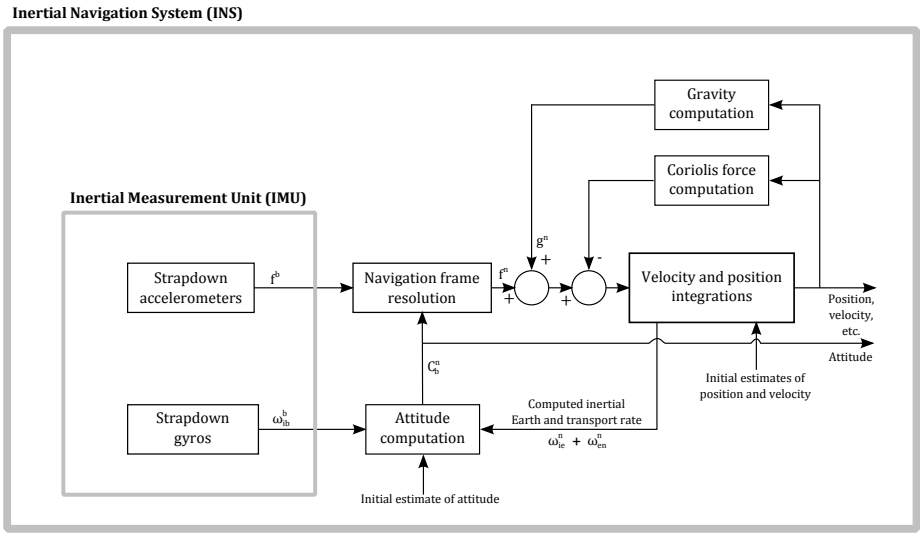

Figure 2.3: Typical INS framework

2.1.3 Inertial navigation system (INS)

An INS is a general purpose dead-reckoning system, requiring no knowledge about host vehicle dynamics or extrinsic sensors. At the core of an INS is the IMU, often comprised of triads of gyroscopes and accelerometers. Gyroscopes measures angular velocity and accelerometers specific force, both relative to an inertial space. Through proper integration of angular velocity and specific force, i.e. handling moving and rotating reference frames, terrestrial dead reckoning is made possible.

If the IMU is of sufficient high quality for it to detect the rotating of Earth over time, it is said to be gyro-compassing grade. A gyro-compass grade IMU can be used to create a self-contained AHRS. State-of-the-art micro-electromechanical system (MEMS) IMUs are just on the verge of breaking into the gyro-compass level of performance, but are not quite there yet. Consequently the two most common gyro-compass grade gyroscope technologies are ring-laser gyroscopes (RLG) and fiber-optic gyroscopes (FOG). In contrast to gimballed gyroscopes, MEMS, RLG and FOG are all strap-down sensors that follows vehicle motion.

IMUs suitable for inertial navigation are generally divided into four grades [5]: *Marine-grade* covers systems installed in military high-demand applications such as warships, submarines and intercontinental ballistic missiles (ICBM), and to some extend space-crafts. The navigation drift is less than 1.8 km per day

and comes with a price-tag on the order of 100k–1M €. *Navigation-grade*, or *aviation-grade*, INSs are used in aircrafts, military and commercial alike. Navigation-grade horizontal error is around 1.5 km per hour[2] and costs around 50k–100k €. *Intermediate-grade* IMUs provides roughly one order of magnitude worse performance, with a price tag of less then 50 000 € these are employed in helicopters and smaller aircrafts. *Tactical-grade* IMUs can only provide realistic navigation in order of minutes and are often used in systems where to gap short outages in GNSS for example in small unmanned aerial vehicles (UAV), or for short-lived systems i.e. guided weapons. High performance as well as compact and high-g rating capable IMUs are subject to strict export license control due to their potential use for weaponry such as long range missiles. This limits their practical commercial use, especially within the offshore business.

2.2 Acoustic positioning

The underwater environment is favorable for acoustics. Though bandwidth is very limited compared to modern radio technology, acoustic modems are often employed for underwater communications, e.g. between surface and subsurface vehicles. Acoustic positioning systems have been used since the beginning of the offshore hydrocarbon industry. Early systems used tone signals, but like developments within radio systems, modern day acoustics rely on spread-spectrum techniques[3], also known as wideband.

Here just the two most common acoustic positioning methods are described: USBL and LBL.

2.2.1 Ultra short baseline (USBL)

A USBL system consists of three components, a transceiver, a responder/transponder and communication. The transceiver, mounted on a surface vehicle, emits a ping which the responder, mounted on a subsea target, responds to. Using an array of hydrophones, either phased array or spherical array, the signal direction and range can be deduced from signal phase and time-of-flight, respectively. Since the responder can be quite small and self-contained, this method is the most common used for subsea target tracking, i.e. crane hooks, divers, AUVs, ROVs, etc.

[2] often given as *in the first hour* or *after loss of aiding*.
[3] Such as Sonardyne's 6G product line.

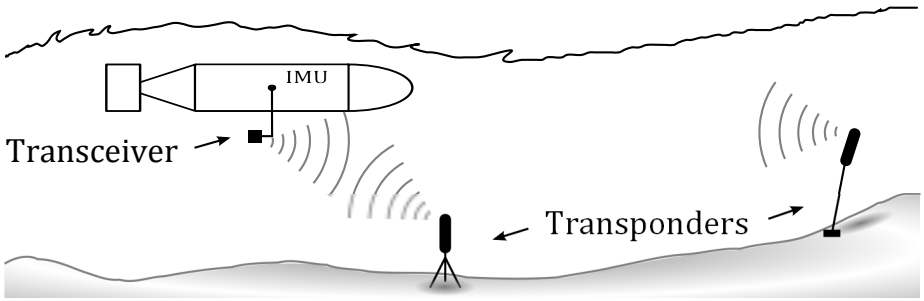

Figure 2.4: Acoustic ranging to seabed transponders

To facilitate subsea navigation, the subsea vehicle's absolute position is derived from the surface vehicle's position, often GNSS, and the USBL measured vector. Using the communication link the position is fed to the subsea vehicle. AUVs usually employ an acoustic link, if USBL is used at all. ROVs use the high-bandwidth tethered link, which minimizes the position latency.

With an optimized USBL system the typical accuracy is given as 0.1 % of slant range, which is 3 m in 3000 m water depth. However, USBL is prone to potentially large error sources: speed of sound through the entire water column, acoustic disturbances at the surface e.g, thrusters, which are not always easy to rectify.

There is a some confusion about naming, since the term USBL is also used for surface positioning using an array of transponders on the seabed. Tracking a subsea target is therefore sometimes referred to as remote, inverse or subsea USBL.

2.2.2 Long baseline (LBL)

Subsea target tracking to centimetric accuracy, independent of depth, is possible with LBL positioning. Using an array of subsea transponders the position of an acoustic transceiver can be determined through trilateration. This however requires a well calibrated transponder array and stationary conditions.

The range to a transponder can be determined with knowledge of sound speed and measurement of the acoustic two-way travel-time. In practice this time-of-flight method also needs to handle a response time delay introduced by the transponder, which is configurable and known. Ranging accuracy is therefor heavily dependent on accurate timing. With wideband acoustics the stated

range precision is better than 0.015 m. Other techniques than pure ranging can be used, such as Doppler shift and range rate [10, 11, 22].

With modern transponders the baseline, the distance between two transponders, can be measured by the transponders themselves. With a large enough array this is enough for calibration, finding the relative positions. If georeferenced navigation is desired, a surface vehicle must be used during calibration.

Accurate LBL positioning is heavily dependent on the geometry of transponders and transceiver position at interrogations. For conventional LBL, covering a large area often means lots of transponder deployments. As mentioned vessel-time is expensive and transponder deployment is a time-consuming task. Instead of ensuring good geometry with transponders, the geometry can be ensured by moving the transceiver. Essentially using three transponders to get a position fix of a transceiver is the same as using one transponder with the transceiver at three different positions. This is known as sparse LBL [10, 15]. Though this promises fewer transponder deployments, it also requires constant movement to ensure good navigation.

2.3 Map based navigation

Map based navigation is basically exploiting knowledge of geophysical properties or artificial features. As maps tends to be created with a lower resolution than what the vehicle sensor can deliver, navigation accuracy is mostly limited by map resolution and accuracy. Both global and local maps can be used.

Terrain relative navigation (TRN) can be accomplish with a mapping sensor such as a lidar or a multibeam echo sounder (MBES), a high-resolution sonar, scanning the terrain underneath the vehicle. The scans and current position estimate are then correlated against a known map. This technique has been used in aircrafts for decades using radar. Instead of matching the height map, or methods such as shadow matching can be used [5, 12].

Anomalies in Earth's magnetic field can be used for navigation by employing a magnetometer [8]. This may be feasible for AUVs where rigorous magnetic field calibration can be carried out, given that a precise enough magnetic map can be provided. For subsea construction where a varying magnetic field is guaranteed, this is simply not practical nor feasible.

Similarly, anomalies in the gravitational field can be used for navigation. Navigation with a gravimeter and an INS has been suggested [8]. This kind of in-

strumentation is targeted towards submarines with long-term navigation needs. But recent advances has used inertial sensors to measure the gravitational field [1]. This would eliminate the need for the large and complex gravimeter, making gravity based navigation possible for smaller and cheaper vehicles. Precise navigation would require a map of higher resolution than what is currently globally available from satellites. As gravity is to find hydrocarbons sub-bottom, offshore production fields are accurately mapped. But since USBL is always available for the offshore industry, the need is not there.

Using artificial landmarks without human interaction requires a framework to do so. One such framework is known in the field of robotics as simultaneous localization and mapping (SLAM) [19]. In such a framework no a priori knowledge of the position of features is needed as the map is built while navigating. This has introduced the use of cheap sensors, such as cameras, for subsea navigation. Features can be anything, due to the generality of the the framework, as well as observed by different sensors. For example a lidar and a camera can both detect the same feature, but with different error characteristics. Drawbacks of SLAM is long-term instability, processing requirements i.e. large amount of features, and loop-closure. Loop-closure is tying two observations of the same feature together, on a revisit. This is no easy task depending on feature matching and navigation errors, unfortunately it is also the core of SLAM.

Chapter 3

Aided Inertial Navigation

This chapter introduces sensor fusion for inertial navigation and particularly the AAINS. Since the INS is a dead-reckoning system it will eventually drift, but it exhibits great short-term relative accuracy. To constrain the position error aiding sensors with complementary properties are employed. The INS solution is then fused together with the aiding sensors in a statistically "optimal" sense.

The following structure applies to this chapter:

Section 3.1 gives brief introduction and overview of state estimation techniques, the core of sensor fusion.

The error-state framework is introduced in Section 3.2, which cleverly uses an INS and aiding sensors for sensor fusion, while making sure that the state estimation filter is nominally correct.

Integration with aiding sensors is dicussed in Section 3.3 along with state augmentation for sensor error modeling.

3.1 State estimation

State estimation theory seeks to estimate the internal condition of a given system. State estimation is applicable to virtually all areas of engineering. In the case of navigation this is most likely the navigation state as previously defined. A system can be represented in many different forms, but a common form used in state estimation is the state-space linear form:

$$\dot{\boldsymbol{x}} = \boldsymbol{A}\boldsymbol{x} + \boldsymbol{B}\boldsymbol{u} + \boldsymbol{w} \tag{3.1}$$

$$\boldsymbol{y} = \boldsymbol{C}\boldsymbol{x} + \boldsymbol{v} \ , \tag{3.2}$$

or non-linear form:

$$\dot{\boldsymbol{x}} = \boldsymbol{f}(\boldsymbol{x}, \boldsymbol{u}, \boldsymbol{w}) \tag{3.3}$$

$$\boldsymbol{y} = \boldsymbol{h}(\boldsymbol{x}, \boldsymbol{v}) \ , \tag{3.4}$$

with state-vector $\boldsymbol{x}$ and output $\boldsymbol{y}$. Process noise $\boldsymbol{w}$ and measurement noise $\boldsymbol{v}$ are stochastic processes, often assumed to be independent and identically distributed random variables. Note that the systems can be either time-varying or time-invariant, linear or non-linear, and continuous or discrete.

Batch processing such as the least-squares method can be used as estimator, but for time-series systems which data should be included? Including all historic data becomes unbearable for long-running systems, but some degree of memory could improve estimates.

Contrary to batch processing is filtering, that is time-series processing. The well-known Kalman filter is an optimal estimator for linear systems, which literally means that it cannot be outperformed. In essence the Kalman filter propagates the estimated state mean and covariance through the system, using a Bayesian approach. For work in this thesis the system is treated as continuous, non-linear and time-varying, while the measurements are treated as discrete, non-linear and time-varying. For non-linear systems there is no such thing as general optimality, so other techniques most be employed to handle the non-linearities.

To successfully apply filtering in practice a number of challenges must be overcome such as asynchronous observations, time-delays, numerical issues and high integrity validation, which is very difficult but of critical importance for trusted survey solutions. These challenges will not be discussed there and the reader is referred to Kalman filter textbooks such as [2, 5, 16] for practical implantation hints.

Using an incorrect system model or process measurement outliers, can lead to filter divergence. Filter divergence is when the estimated state mean and covariance are not in agreement, i.e. the filter can become over-confident about its

estimates. Depending on application this can have major consequences, especially in closed-loop systems with humans, such as space-crafts and dynamically positioned (DP) surface vessels.

3.1.1 Non-linear Kalman filters

Non-linear extensions to the Kalman filter using different principles exists. The best known and most widely used, is the extended Kalman filter (EKF). Soon after the Kalman filter was introduced, work on applying it to non-linear systems began. The EKF is a bootstrap method that linearizes the system around the state estimate, which in turn is based on the linearized system.

This brings up the dilemma: if the estimate is way off the linearization will be wrong, thus, will the new estimates will be even more wrong? Therefore with an EKF it is important to make sure that the filter operates close to its linearization point at all times. It is worth noting that the non-linearities also will have a negative effect on filter divergence, if the nominal state is incorrect.

The work presented in this thesis and carried out in this project has only dealt with the EKF. With careful design and operation the filter will perform just fine for navigation purposes. Alternatively, it can be run iteratively to pull-in states with large uncertainty, although convergence is not guaranteed.

Since the EKF is based on a simple linearization approach multiple attempts at making at high-order filter has been made, with two noteworthy mentions here, i.e. the unscented Kalman filter (UKF) and divided-differences (DD2). Comparisons between the UKF and DD2 shows similar performance, both with the capability to handle non-linear systems to a much higher degree than the EKF. Both are also capable of handling non-Gaussian process and measurement noise.

Multi-hypothesis filters such as Gaussian mixture filters and the particle filter have been used for more complex problems that are highly non-linear with non-Gaussian noise terms. These tend to require a hefty amount of processing power and memory. Such filters are just beginning to be used online, but most applications are still offline processing.

3.1.2 Smoothing

When post-processing data one is not constraint by time-causality of the measurements, i.e. all the measurements are available at all times. The knowledge of all past and future measurements can be used to enhance the state estimates. Furthermore, due to the nature of the Kalman filter measurement updates, navigation output will be jagged if the corrections are applied directly. For mapping applications jagged maps are undesirable, as they do not reflect the real-world but is an artifact of the navigation system.

State estimation smoothers satisfy both needs. Two common modes of operation are used: fixed interval or fixed lag. Fixed lag smoothing can be run online, by smoothing over a constant sliding window or lag. This type of smoothing does not guarantee stability so should be used with caution. Fixed interval smoothing concentrates on a specific non-sliding window, normally chosen as the entire data set for post-processing.

One such smoother is the Rauch–Tung–Striebel (RTS) which is a two-pass smoother. The regular Kalman filter is used for the forward pass and filtered state estimates and covariances are stored along with state transition matrices. These are then propagated backwards in a simple fashion that ignores measurement updates entirely.

If the backward pass should include measurement updates as well, smoothers such as the modified Bryson-Frazier (MBF) smoother can be used. Since the forward pass also consist of the Kalman filter, only the backward pass differs from RTS, except the need for storing measurement update matrices as well.

The RTS smoother is often used on basis of its simplicity, stability and speed. The improved estimates, both propagated mean and covariance, comes virtually free. Smoothing AAINS with RTS is so fast that the author recommends to always use smoothing for post-processing.

3.2 Error-state framework

In an error state Kalman filter (ESKF) the estimator tries to correct the errors on the underlying system. For an AAINS the INS would be the underlying system. Instead of estimating full states as in *depth*, the *depth error* is estimated by the ESKF. Figure 3.1 shows such a set-up. The ESKF can be any type of estimator, but in the work presented in this thesis an EKF is employed.

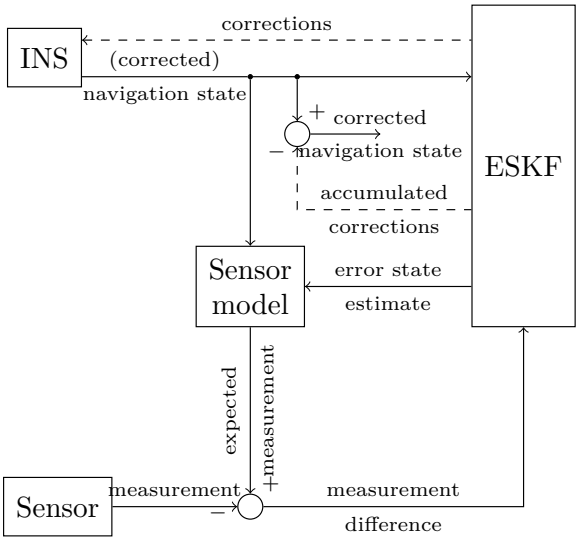

Figure 3.1: General AINS framework. The corrections, dashed connections, are either applied to the INS output or alternatively fed back to the INS. If the latter is true, the error state must be reset.

Advantages of this framework includes low update rate and modularity. If the INS outputs navigation data at hundreds of hertz and the aiding sensors outputs data an order or two slower, there is no need to run the filter faster, which would lead to unnecessary numerical error built-up. Furthermore, the full state is more likely to develop faster than the error state, e.g. consider a vehicle in motion with an INS on-board, it is more likely that the vehicle would have moved farther than the corresponding INS position error. The low update rate allows for more elaborate filters to be implemented on lower performance processing platforms compared to their full state equivalent—also one of the reasons for the concept in the early days of Kalman filtering and inertial navigation.

Modularity comes in the form of separating the INS unit and aiding sensors from the ESKF. This allows the either one to be replaced by a similar subsystem with the same interface. The preceding statement only holds true for similar systems, different INS mechanization is clearly an issue, i.e. different navigation state definitions. Modularity is important for engineers when integrating systems.

The EKSF states are derived from a chosen INS mechanization, In this work a local level geodetic frame mechanization has been used [5, 20], where the local level axes are aligned with North and East. This mechanization is widely used, but suffers from singularity near the geographic poles. In practice this limits

the use in very high latitude regions, as estimation error becomes be intolerable. Other mechanizations such as *wander azimuth* can resolve these singularities by mathematical abstraction.

3.3 Aiding

An aiding sensor is said to have a coupling with the ESKF that can either be loose, tight, ultra tight or deep. Taking GNSS integration as example, a loose coupling would mean that the input to the ESKF is the GNSS estimated position. Knowing that that position is actually derived from pseudo-ranges, much like LBL, it is a fair assumption using these raw ranges instead of the positions would benefit the estimation. This would be an example of a tightly coupled aiding sensor. Ultra tight coupling is when the IMU measurements and quantities derived from these are used to assist the aiding sensor operation, e.g. knowing acceleration and/or velocity from an IMU can aid signal tracking loops in an aiding sensor. When using the INS or ESKF to aid the aiding sensor, e.g. in a tracking control-loop, the coupling is said to be deep. From a modularity point of view it is clear that the deeper the coupling, the harder integration with other aiding sensor might be. Deeper coupling means better estimation, robustness and likely access to more correct error metrics.

As mentioned in Chapter 2 using a depth sensor, the navigation problem becomes 2D instead of 3D. In practice all AINSs are aided by depth/altitude as the vertical channel of the INS is the most unstable.

DVLs have exemplary good performance and with bounded velocity error the synergistic effect when aiding is tangible. AAINS performance is more or less based on DVL/INS performance. Since their introduction into underwater navigation by AUV manufactures two decades ago, the combination DVL and INS is stronger than ever and is becoming a standard instrument on ROVs. DVLs can output 3D velocity which can be used for loose coupling or the four beams can be used for tight integration. In this work the former is used.

Although GNSS is denied underwater, USBL positioning functions similarly to stand-alone single receiver GNSS. It is easy to integrate and puts an upper bound on position error. USBL systems are often loosely coupled due to the nature of the processing chain, see Section 2.2.1.

LBL range aiding is regularly used which constitutes a tight coupling with the ESKF. This is also true for this project. Others use range-rate or delta ranges for aiding, but all are examples of tightly coupled systems. LBL aiding puts an

upper bound on position error, through ranges error bounds, that are superior to USBL aiding.

Although no work has been done in this project, mapping sensors could be integrated into AAINS to provide a SLAM solution. Whether the sensor would need to be loosely or tightly coupled the author will speculate on, but merely point out that SLAM filters tend to use features as aiding and not the underlying mapping sensor information, i.e. range and bearing.

Initialization of the INS is done with appropriate observations. Orientation is taken from the AHRS, position estimates can be taken from the USBL system, a transponder position or manually input, all with large uncertainty, i.e. hundreds of meter. Depth is simply taken from the pressure depth sensor. This procedure allows for potential restart of the ESKF and thus the AAINS, with almost instantaneous start-up if the AHRS has settled.

By simply augmenting the ESKF with a model of the parameters the framework can be used to estimate sensor errors and parameters such as accelerometer bias and DVL scale factor error. Throughout this work low order models, typically first-order Gauss-Markov models, are exclusively used, due to simplicity and generality: it is possible to model both random constants, white noise, and degrees of "colored" noise that lie between the two extremes.

During this project a number of sensor parameters have been modeled. These include intrinsic parameters such as inertial sensor biases and scale-factor, DVL scale-factor and LBL speed-of-sound errors; and extrinsic parameter such as lever arms, mounting angles and transponder positions. These are not all necessarily applied for all applications, but they have all been used for the publications in Part II. Some of these are regularly modeled by AAINS manufacturers and some, like lever arms, are rare in the literature. An ESKF with many aiding sensors can easily consist of 30 states. Even larger states-spaces are known to estimated by commercial AINS manufacturers in other domains.

3.4 Simulation

The work methodology has been to implement new features, i.e. sensor error models, first in simulation then in the estimator. Once both have been verified against each other, real data is processed. If there is a large discrepancy between simulation–estimation results and data–estimation results, the simulation is analyzed to check that the truth model captures enough dynamics. This methodology ensures that the simulation model is close enough to the real world

that it can be trusted, while having simpler models in the ESKF.

Our simulation tool allows us to generate consistent "true" IMU and navigation data from any reference navigation state, be it an AAINS post-processed solution, a simple trajectory design by hand or the output of hydrodynamic models. This method is exploited in all the papers in Part II as this allows to capture realistic dynamics, but with full control of the aiding sensors, errors and noise with perfect knowledge of truth.

Planning operations can be tricky since AINS performance is highly dependent on the trajectory. The most reliable course is to run a covariance simulation. In this manner, exploring different scenarios such as trajectories or sensor configuration is quick and relatively painless.

When estimating lots of parameters (see Section 4.2) it is important that the parameters can actually be estimated. With too high degrees-of-freedom the filter will incorrectly use those states to compensate for false estimation errors. The observability/estimability of the states can be ensured by planning the trajectory using simulation. Using real-time output of state covariances would also allow operators to perform dynamic maneuvers to increase observability. Alternatively, the trajectories can be designed to minimize the influence of certain errors, i.e. lever arm errors.

Chapter 4

Application Results

This chapter highlights the research results presented in Part II of this dissertation. The structure is as follows:

Section 4.1 deals with IMU calibration from multiple perspectives, i.e. manufacturer to end-user. IMU calibration is the foundation on which inertial navigation is built upon. Approaching practical cm-level relative accuracy is discussed in Section 4.2. Section 4.3 looks at the subsea survey task known as *metrology*. In Section 4.3.1 a method using based on SLAM and sparse LBL is presented and Section 4.3.2 investigates lidar based contactless metrology.

Throughout the project Sonardyne has provided lots of data and experience. Data from both Sonardyne's trials facility in Plymouth, UK and from customers has been used in this work. Experience has been provided by a mix between Sonardyne engineers and survey support group, and interaction with commercial offshore costumers.

4.1 IMU calibration

Intrinsic IMU calibration aims to compensate for systematic and predictable errors and imperfections in the inertial sensors and assembly, also known as the

inertial sensor assembly (ISA). Which parameters are observable from sensor data and compensational are highly dependent on sensor technology. The very high performance mechanical sensors of the last century were rigorously modeled to handle the heap of effects the observed. Optical gyroscopes such as FOGs and especially RLGs are less sensitive to acceleration induced effects for example, which simplifies calibration and sensor characterization. Current MEMS sensor technology also requires rigorous calibration to handle non-linear effects.

In Paper A we consider IMU calibration with RLGs. Specifically we look at each sensor bias and scale-factor as well as inter-sensor alignment. Inter-sensor alignment is important as the INS assumes orthogonal IMU axes. Furthermore the algorithms presented also considers ISA to IMU mounting; with orthogonal IMU (output) axes that are aligned with the mechanical ISA housing, IMU/INS replacement becomes very practical. Alternatively, if the IMU axes are "arbitrarily" defined, replacing an INS more or less voids all extrinsic sensor calibrations, i.e. sensor mounting relative to INS, and INS to vessel, etc., or requires more elaborate methods for "hot-swapping" INSs. Temperature dependency is not considered. The sensors could already be compensated for temperature or alternatively the calibration could be carried out over a given temperature interval and interpolation could be used.

Three scenarios are considered: factory calibration, calibration at remote site and at-sea calibration/quality assessment. Factory calibration is the most comprehensive and also requires access to a two-axis rotation table. Both a conventional least-squares approach and a Kalman filter approach is evaluated and compared. Since a previously used proprietary algorithm that does not calibrate to ISA housing, is used as benchmark, extensive effort is used to make sure comparison between algorithms are truthful towards accuracy. Using experimental data we show that both approaches achieves similar accuracy as the benchmark, reprinted in Table 4.1 and 4.2. This means all three algorithms, very different in nature, are cross-validated.

For the two other scenarios only a Kalman filter AINS approach is employed. These are meant for rental companies, off-site offices, etc. at land to calibrate IMUs using limited equipment, and for assessment of the IMU while at sea. Per the nature of the domain, some marine inertial systems are frequently subjected to rough transport, handling and harsh operational conditions. Other systems may be in continuous operation for years. This introduces a special need to reliably validate and calibrate INS performance at customer storage facilities on land or at times offshore. In these scenarios it is assumed that the IMU is nominally calibrated so that any inertial sensor axis misalignments have been corrected. To the author's best knowledge neither scenario have been described in the scientific literature prior. We conclude in Paper A that in-field calibration both on land and at sea is feasible, with certain limitations. Furthermore at-

Table 4.1: Attitude and heading performance for factory calibration.

	Orientation RMSE (mili-°)		
IMU#	AINS	NLSQ	Proprietary
1	10.7668	11.0004	12.8470
2	20.3281	20.9816	21.9415
3	26.6626	26.1676	27.4034
4	22.3295	23.0129	22.6769
5	28.8444	27.5539	25.1533
6	26.3689	26.5847	26.5428
Mean	22.5500	22.5502	22.7608

Table 4.2: Acceleration performance for factory calibration.

	Acceleration RMSE (μg)		
IMU#	AINS	NLSQ	Proprietary
1	16.7683	16.4582	21.9174
2	29.9454	26.5149	29.7009
3	28.5088	22.1025	89.6507
4	33.2744	29.1359	28.2366
5	25.6030	23.4516	31.6360
6	31.9135	30.0562	34.0508
Mean	27.6689	24.6199	39.1987

sea requires good gravity models or local gravity observations, beyond a GNSS receiver or exploiting knowledge about vessel station-keeping. The results interestingly shows comparable calibration accuracy between the two scenarios.

4.2 Approaching cm-level accuracy

Achieving 10 cm relative accuracy has become common by employing AAINS with LBL. Optimizing, tuning and calibrating by experts can yield somewhat better accuracy, under good conditions. Approaching the 1 cm or even sub-cm level requires better models to account for effects that would normally be considered unimportant. To some extent this can be paralleled with the advancement within GNSS, although the same level of modeling detail is not currently necessary[1].

Paper C investigates how far we are from practically achieving 1 cm level navigation. Practically, in the sense that competent LBL/AAINS offshore personnel should be able to reach this level of performance without necessarily consulting experts. Since the DVL/INS combination provides accurate and robust dead-reckoning navigation and the raw acoustic ranging precision is quite good, i.e. cm-level, centimetric subsea navigation is within reach.

Unfortunately, having analyzed lots of real-life navigation data, one of the most common AAINS problems is incorrect measurement and application of extrinsic aiding sensor parameters, e.g. lever arm and orientation sign errors and axis confusion. Not only do these for obvious reasons need to be correct, but to push the limit, accuracies beyond what is practically obtainable off-shore[2] is needed. These reasons lead us to allow for both completely unknown parameters and roughly known parameters. In both cases the parameters are refined by augmenting the KF during calibration.

ROVs and especially AUVs have limited maneuverability due to design choices, i.e. buoyancy and thrust, which means that they operate mostly as leveled platforms with near zero pitch and roll. We used real-world data collected from a deep sea ROV to analyze the expected accuracy, as parameters requires excitation to become adequately observable. Unprecedented data sets were collected on separate dives with the same ROV, but different pilots. During the dive the ROV pilots were asked to perform specific tasks, some of which was with the highest permissible dynamic. Prior to and following the trials the au-

[1] e.g. solid earth tides and similar effects, that seemed unrealistic to model and estimate a decade or two ago.

[2] Measuring on a large complex robot midst of an uneasy sea is not trivial.

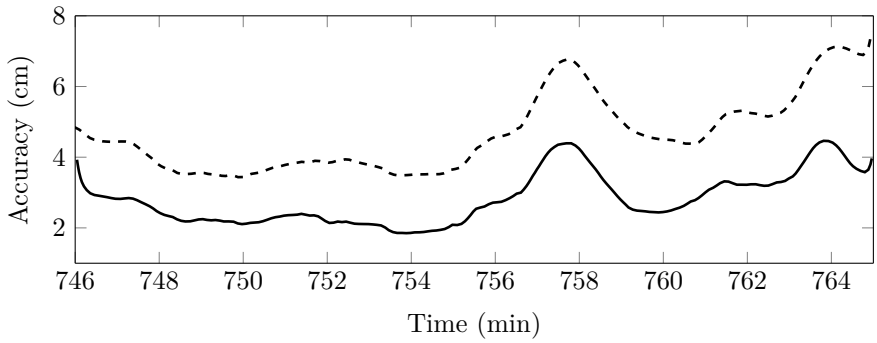

Figure 4.1: Navigation 1-DRMS accuracy for trial II. Dashed line is the RMS value for 50 simulation runs.

thor inquired several people including ROV pilots, party chief, AUV systems integrators and builders, etc. on their expectations for actual dynamics. Interestingly everyone overestimated maximum achievable roll and pitch angle. The consequence is that some parameters will have limited estimation accuracy, e.g pressure depth lever arm estimation.

Furthermore we show that by using a calibrated LBL array for calibration, an uncalibrated sparse LBL array can be used for subsequent accurate relative navigation. This bears resemblance to the work in Paper B (or Section 4.3.1) where uncertain but static transponders were used for relative navigation using SLAM sparse LBL.

Simulation results shows that both parameter estimation and cm-level navigation is achievable. Additionally, comparing parameters estimated with our proposed method on real data with measurements and other calibration methods, for two separate trials, shows a clear correspondence and convergence (reprinted in Table 4.3). Unfortunately the data collected was not suitable to use as a robust reference for this level of navigation accuracy, but via a trusted simulation platform with the same real-world dynamics as input, the navigation have been verified. Fig. 4.1 compares the Monte Carlo simulation output with the real-world processed AAINS output.

We argue that ideally separating each sensor for calibration would eliminate cross-calibration errors as well as simplify any trouble-shooting. On the other hand, it is crystal clear that having DVL/INS that can be trusted solves many problems. Since DVL/INS assemblies and co-located and pre-calibrated systems are available from multiple manufacturers, these should be preferred.

Table 4.3: Trial I and II, difference $\Delta\theta = \hat{\theta} - \tilde{\theta}$, between the estimated and measured parameters. Estimation std.dev. σ is taken from the AAINS.

	Trial I		Trial II		
Parameter	$\lvert\Delta\theta\rvert$	σ	$\lvert\Delta\theta\rvert$	σ	Unit
${\tau_{\mathrm{pd}}}^{*}$	0.22	0.08	0.23	0.09	s
${\tau_{\mathrm{dvl}}}^{*}$	2.31	0.93	0.25	0.89	ms
${r^{\mathrm{b}}_{\mathrm{dvl,x}}}^{\dagger}$	0.22	0.44	0.27	0.46	cm
${r^{\mathrm{b}}_{\mathrm{dvl,y}}}^{\dagger}$	0.58	0.43	0.23	0.45	cm
${r^{\mathrm{b}}_{\mathrm{dvl,z}}}^{\dagger}$	10.45	1.35	10.69	0.99	cm
k^{*}	0.09	0.12	0.10	0.15	%
${\alpha_{\mathrm{dvl}}}^{\dagger}$	0.10	0.09	0.02	0.11	°
${\beta_{\mathrm{dvl}}}^{\dagger}$	0.02	0.09	0.01	0.11	°
${\gamma_{\mathrm{dvl}}}^{\dagger}$	0.07	0.07	0.01	0.09	°
${r^{\mathrm{b}}_{\mathrm{lbl,x}}}^{\ddagger}$	4.55	0.30	3.31	0.35	cm
${r^{\mathrm{b}}_{\mathrm{lbl,y}}}^{\ddagger}$	3.33	0.27	2.45	0.29	cm
${r^{\mathrm{b}}_{\mathrm{lbl,z}}}^{\ddagger}$	3.36	0.99	4.55	1.70	cm

* measured quantity assumed zero.
† measured quantity from schematic.
‡ measured with hand held laser ranger.

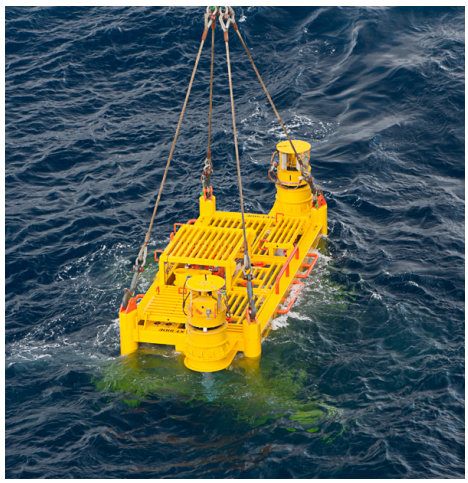

Figure 4.2: Subsea structure pre-installation on seabed, with the two hubs clearly visible

4.3 Metrology

Subsea construction, like land construction, involves a lot of accurate surveying. This type of accurate surveying is also known as subsea (spool piece and jumper) metrology. A common task is to connect two subsea structures using a pipe section manufactured to the dimensions obtained from a metrology operation. An *as-built* survey is then carried out to check how close to the plans the site actually is, but foremost to get the measurements necessary to construct the connecting pipe. This pipe is constructed on-shore and brought out to sea, often by barge and a handful of tugboats. A crane on-board a construction vessel will then lower it down while an ROV will inspect and fit it to the subsea structures.

The implications if this pipe does not fit should be clear. On that account great care is taken while performing metrologies to ensure everything is correctly measured and recorded. Quality control is ensured by having independent and/or redundant measurements, careful planning and double checking results at all levels[3]. That being said, current conventional methods involves a lot tedious time-consuming work that screams for smarter solutions[4].

[3] including spending expensive vessel time waiting for on-shore surveyors to verify results, when the communication link is horribly slow.

[4] especially when you have a background in control and robotics.

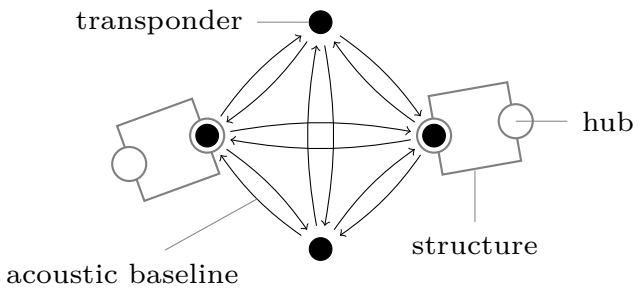

Figure 4.3: Conventional acoustic metrology set-up with transponders in a braced quadrilateral configuration.

The subsea metrology problem [7] can be boiled down to finding the distance between two objects, known as the baseline, their relative orientation and the seabed profile along the baseline. Conventional acoustic metrology deploys an array of LBL transponders, often in a *braced quadrilateral* (see Figure 4.3), with two transponders located in or near the points of interest. The baseline is derived from repeated LBL observations, at different transponder orientations. Vertical and horizontal metrologies can use different techniques for measuring the relative orientation. One solution is to dock the ROV with the structures and read-out the AHRS orientation. A calibrated pressure depth sensor is used to sample the seabed profile, holding the sensor in the articulated ROV arm, back-and-forth in what is known as a *depth-loop*. By starting and ending in the same the location the depth-loop improves the measurements by eliminating any difference.

4.3.1 SLAM Metrology

In paper B we investigate a metrology method using only two transponders, i.e. sparse LBL. The reasoning being that fewer transponders would lead to less vessel time spent on deployments. To further increase operational flexibility and efficiency, we also assume that the transponder positions are only partially known, or known with a given uncertainty. This work only considers metrology baselines, as only the number of transponders are reduced compared to conventional metrology.

Since the baseline is not required to be georeferenced a relative navigation solution is used. One transponder is chosen as datum and the other automatically calibrated with respect to the datum. The array is then calibrated in a SLAM sense i.e. by running the navigation filter the position is found.

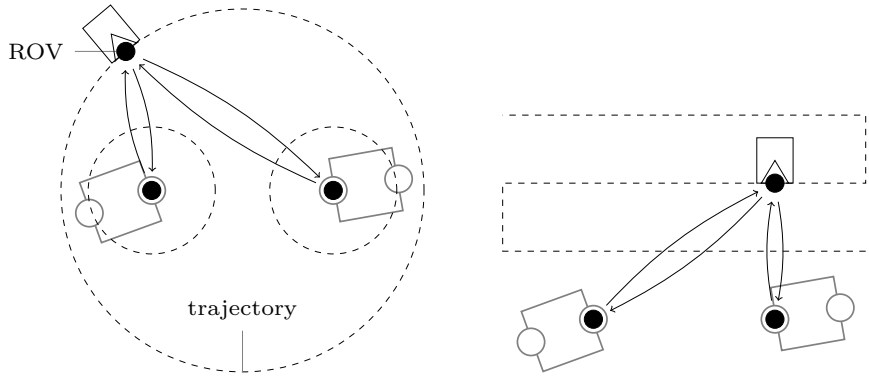

(a) Circular trajectory **(b)** Meander trajectory

Figure 4.4: Trajectories suggested for sparse LBL-inertial SLAM metrology

There is a duality in the observability of ROV position and that of the transponder position. In both cases they require a dynamic trajectory and consideration for geometry for sparse LBL. Two trajectories are suggested: a circular trajectory encircling both the array and each individual transponders; and a meander type of trajectory. The former is trying to maximize observability of navigation and transponder errors, while the latter tries to keep navigational errors to a minimum, i.e. leverarms have no influence if there is no orientation changes.

The proposed method was both tried out in simulation prior, during and after a sea-trial. The sea-trial carried out in the Mediterranean sea consisted of two full, and very similar, metrologies. Paper B compares simulation with real data, results reprinted in Table 4.4, and shows that the proposed method works within the tolerances of set-out by the survey companies, when comparing to the conventional acoustic approach.

Different kind of realistic error sources were examined and resulted in an in-depth error budget (Table B.3, page 93). This error budget revealed some interesting insights regarding correlation and especially uncorrelation—the investigated method turned out to be more tolerant towards errors than originally assumed.

The concept now included in Sonardyne's product line *SPRINT Inertial Metrology* [17].

Table 4.4: SLAMBL results compared by trajectory and baseline. σ is the std.dev. of the baseline and Δ the difference between the SLAMBL and the conventional acoustic baseline. The subscripts $_{\mathrm{h}}$ and $_{\mathrm{v}}$ indicate horizontal and vertical baseline components, respectively.

	Baselines			
	Horizontal		Vertical	
Trajectory	σ_{h} (cm)	Δ_{h} (cm)	σ_{v} (cm)	Δ_{v} (cm)
	Trial I			
Circles	1.2	2.1	2.4	0.2
Meander	4.5	3.2	5.2	0.1
	Trial II			
Circles	1.2	2.3	1.8	1.0
Meander	4.4	3.4	5.9	1.3

4.3.2 Lidar Metrology

Another approach to the metrology problem is to generate a high resolution and high accuracy map, from which the surveyors can measure the baseline, relative orientation and seabed profile. This approach qualifies as contactless metrology, where the ROV never touches or comes near the subsea structures, which can be a prerequisite for some operations, e.g. close to a drilling riser[5].

Offshore surveyors already use 3D maps, e.g. for pipe out-of-straightness and flow-line as-built surveys. These maps are currently generated using sonars, not necessarily high-resolution MBES. However, for metrology the resolution and accuracy requirements are higher.

As of writing a handful companies has the capability of provide 3D scanning sensors suitable for subsea metrology. The 3D sensors are either subsea lidar, high resolution MBES, camera combined with structured light or photogrammetry. Except for photogrammetry, the techniques all require that the sensor is static during data collection. To cover the area and or structures multiple scans are often necessary. To stitch the scans together to a full model, called *registration*, multiple known targets are needed to be visible in overlapping scans. Registration targets are often highly reflective spheres placed on stands or struc-

[5]The vertical pipe connecting subsea infrastructure to the surface.

tures. Photogrammetry is not considered due to excessive processing time and since underwater photogrammetry is hard due to visibility, color shifts and the boundary layers between air, glass and water [9].

In Paper D we investigate high resolution high accuracy mapping from a roving platform, using a 2D scanning sensor[6]. This method obviate registration targets all together, thus require less set-up time subsea. Land and aerial high resolution mapping have seen fast growth due to multiple enabling technologies such as accessible survey-grade GNSS, drone technology and processing software tools. This has led to a change towards dynamic mapping instead of conventional static mapping.

This paradigm shift has yet to happen for subsea surveying. With the underwater survey community still considering static scanning a new technology, roving applications would seem out of reach. But the work herein shows that the accurate navigation required for high accuracy and high resolution maps is obtainable with an optimized AAINS. The techniques from Paper C and Paper B can be used to enhance and simplify mapping operations.

The work specifically concentrates on lidar mapping for subsea metrology surveys, demonstrated through both a simulation study and on sea-trial data. Using 3D models of (or parts of) the subsea structures to estimate the structures' location and orientation, the metrology results are straightforwardly derived. The 3D models are matched to operator selected regions-of-interest (ROI) by using an iterative approach called point-to-patch, which minimizes the distance between points and triangles in the 3D model.

A simulation study showed that the required metrology baseline accuracy (5-15 cm) and relative orientation (1 deg) are met, even in the presence of realistic measurement errors: 5 cm on lever arms, 5 deg misalignment and 0.1 s latency—concurrently. The simulation results are reprinted in Table 4.5.

The sea-trial was carried out together with MBARI during a cruise on-board the R/V Western Flyer. This was part of MBARI's 1 cm mapping project [3], in which they evaluate a whole array of mapping sensors: lidar, stereo cameras and MBES. The lidar metrology results from the sea-trial, reprinted in Table 4.6, verifies that the method works well within the baseline tolerance (5-15 cm) required by the surveyors.

[6]also known as a line scanner or profile scanner.

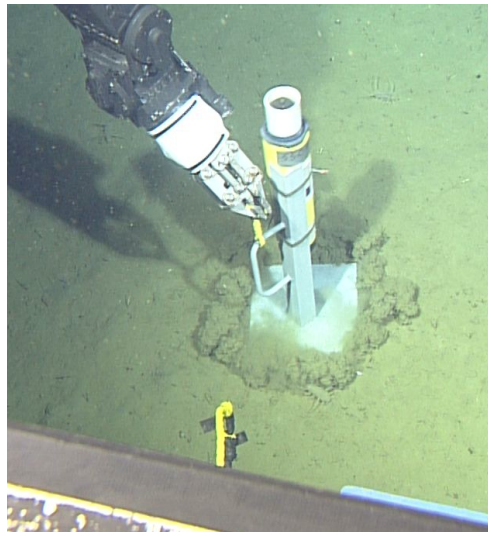

(a) Mini transponder deployment with ROV manipulator. Image courtesy of MBARI.

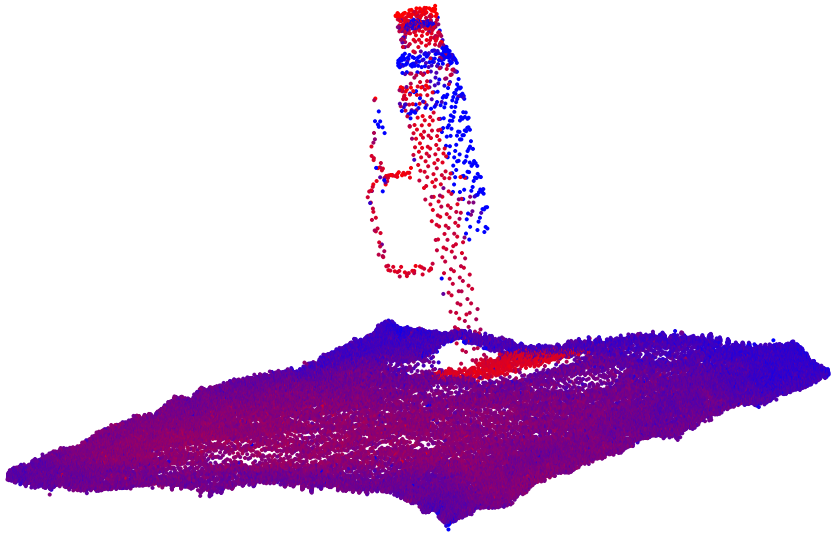

(b) Lidar point cloud of transponder 2 colored by the amplitude of the return signal. Redder equals higher amplitude. Notice how the metal stand and bright plastic area have the highest amplitude and the rubber sleeve (yellow part in Fig. 4.5a) has the lowest.

Figure 4.5: Trial survey trajectories. Begins at the circle and ends at the triangle. Transponder positions are marked with diamonds.

Table 4.5: Simulation study metrology baseline error $\delta\zeta$ and relative orientation error components $\delta\alpha$ and $\delta\beta$, for each pass in opposite direction. The error scenario was repeated 10 times with the mean and worst case highlighted here.

Scenario	$\delta\zeta$ (cm)	$\delta\alpha$ (°)	$\delta\beta$ (°)
1st pass			
No error (mean)	3.82	0.23	0.25
No error (worst)	6.44	0.60	0.66
Error (mean)	4.68	0.22	0.25
Error (worst)	9.81	0.45	0.49
2nd pass			
No error (mean)	4.40	0.22	0.62
No error (worst)	7.32	0.36	0.98
Error (mean)	4.67	0.35	0.73
Error (worst)	11.30	0.70	1.02

Table 4.6: MBARI metrology trial results. The baseline difference $\Delta\zeta$ is derived from the LBL reference for trial data and from the truth model for the simulation scenario.

Scenario	$\Delta\zeta$ (cm)
Nominal parameters	-1.4
Latency corrected	-3.6
Simulation	1.4

Chapter 5

Conclusion

The main objective of the project presented in this thesis has been to enhance current state-of-the-art subsea navigation, with a focus on AAINS. The work herein could fortunately consider holistic solutions to challenging real-world commercial problems; a good example of this is the use of operational procedures to simplify estimation problems.

In summary, this thesis provides an overview of the plethora of challenges working deep underwater bring about, along with the tools currently employed. An outline of current underwater navigation concepts is presented in Chapter 2. Three different general types of navigation were discussed: dead-reckoning, acoustic positioning and map based navigation. Their applications and practically was discussed.

Prevalent practice is to incorporate and integrate a multitude of sensors to improve navigation performance by exploiting synergies between the different sensor types. Sensor fusion has as a general concept matured and become common, even GNSS is commonly fused with IMUs to increase usefulness. Within underwater navigation, AINS and especially AAINS, are gaining more ground and are accepted as a requirement for high accuracy navigation. Chapter 3 gives an overview of (A)AINS, with a brief discussion about different state estimators and the most commonly used framework.

Finally, Chapter 4 outlines specific applications of AAINS that has been realized during the project. A new Kalman filter based method for IMU calibration is presented for factory calibration, and for in-field calibration at remote sites and at sea. For factory calibration the method is validated and compared to two other methods. The subsea construction survey problem *metrology* was examined with two different methods, both notably different from conventional practice. Lastly, work on increasing state-of-the-art subsea navigation accuracy with an order of magnitude, in practically, was presented. This work use system identification techniques which has the potential to decrease normal (human) operational errors.

5.1 Contributions

The scientific contributions from this thesis and the project as a whole, are largely covered by the publications in Part II:

IMU calibration has been around for decades. What this work contributes with is a Kalman filtering approach, i.e. time-series estimation, versus conventional batch processing. If more advanced compensation models were implemented, this technique has the potential to easily account for those. Furthermore, we have introduced two new calibration scenarios for the scientific community as well as proposed solutions which allows for in-field calibration or assessment with limited external information. In-field calibration and assessment can potentially save end-users much time and frustration if they come upon a faulty IMU, and adds value for long-term applications.

In an attempt to make AAINS more practical usable whilst increasing accuracy, system identification has been employed to real-life scenarios from unprecedented ROV maneuvers. Experience and data analysis have shown that trying to trouble-shoot an AAINS, even with a strong background in state estimation, is quite challenging. By providing operational procedures, automating parameter estimation can become very robust and mistakes hopefully avoided. Additionally, the contribution proposes how to increase accuracy of state-of-the-art subsea navigation in an attempt to approach 1 cm-level accuracy.

To the field of subsea metrology, two main contributions have been made: SLAM sparse LBL inertial metrology and lidar mapping. While inertial metrology with sparse LBL has developed into commercial products and services, high-resolution mapping from a roving platform has yet some work ahead. The results presented for lidar mapping together with the work of MBARI is novel in the subsea domain and has attracted considerable interest and acceptance

from the subsea survey domain.

A real-world operational improvement of ROV dynamic mapping accuracy by about an order of magnitude has been demonstrated. At least as important, the robustness, safety (no contact) and time efficiency is also considerably better than current state of the art. Reducing the time taken for doing a meteorology by more than 50 % will save several tens of thousands €per job and with hundreds of metrology jobs per year the cost (and environmental) saving is significant.

Beside the main scientific contributions mentioned above, during the course of the project the author has been the main driver of a navigation post-processing software package. This software is currently in use by both commercial customers and used for internal development of testing etc. Moreover, the author has together with the external partners planned and successfully executed multiple experimental data collection trials, both on-shore and off-shore.

5.2 Perspective and outlook

With the last decade's evolution within MEMS technology, gyro-compassing grade MEMS IMUs should become available within the next 2–5 years. These will eventually shrink the size, power consumption and price of IMUs. This trend will make new applications possible where current technology is prohibited due to either reason, or all. Another interesting inertial sensor technology is the hemispherical resonating gyroscope (HRG), which has so far only seen limited use. Published results shows remarkable performance with a very small sensor, but so far the price-tag has been astronomical. If mass production is feasible, these are likely candidates to take over the high-performance gyroscope market that is currently dominated by FOGs and RLGs. Alas, with new technology also comes new challenges, among those are especially IMU calibration and characterization of interest–not much have been publish so far.

As processing power increases more elaborate estimation techniques can be applied. This would be both non-linear estimators to minimize linearization errors and thus handle larger uncertainty in initial parameters. While non-linear filtering could in itself lead to more robustness, looking at other industries and domains for their solutions will be beneficial. Applying more elaborate outlier rejection schemes and concepts from the GNSS and aerospace industry is an obvious choice.

Offshore, ROV real-time navigation is generally different from the real-time nav-

igation used by the surveyors, and often by an almost complete redundant set of sensors. One reason could be that they simply have slightly worse performing, thus cheaper, but dedicated navigation sensors for the ROV and then mount better sensors if they need to perform surveys. But interestingly enough almost all commercial ROV navigation and guidance is carried out visually and manually, which can limits operations. Dynamic positioning (DP) is a well known concept for surface vessels, but thorough implementation for ROVs has not happened yet. 3D positioning is easily gained through the use of either a complete navigation system such as an AAINS or by simply using the different sensors, and it is the author's opinion that this will happen sooner or later—but is remarkable that it has not happened already, seems like a low-hanging fruit.

Following the trend from land and aerial based surveying, dynamic high resolution mapping seems likely to evolve for the subsea domain within the next couple of years and be mature within four. Since most of the technology is already there, it is mostly a matter of applying it to the subsea domain. Besides subsea construction, multiple application areas are already looking at improving mapping: oceanic oceanography e.g. MBARI, ship wrecks for e.g. treasure hunts and salvage, and archeology preservation and munition watch.

Subsea mapping sensor technology will eventually improve following interest and growth in applications. One particular sensor technology that does not yet exist for underwater application is the multibeam lidar. This type of lidar shoots multiple beams out in swath, akin to MBES. For land applications these are often scanning mode sensors delivering an almost full view of the surroundings, with an overwhelmingly amount of data. This technology is employed on self-driving cars to get a real-time 3D world around it, and could in principle be use for the same type of situational awareness subsea, or for fast data acquisition with surveys.

Bibliography

[1] Diogo Ayres-Sampaio et al. "A Comparison Between Three IMUs for Strapdown Airborne Gravimetry". In: *Surveys in Geophysics* (Mar. 2015). ISSN: 0169-3298. DOI: 10.1007/s10712-015-9323-5. URL: http://link.springer.com/10.1007/s10712-015-9323-5.

[2] Robert Grover Brown and Patrick Y. C. Hwang. *Introduction to Random Signals and Applied Kalman Filtering*. 3rd ed. Wiley, 1996, p. 496. ISBN: 0471128392.

[3] D.W. Caress et al. *Repeat 1-cm Resolution Topographic And 2.5-mm Resolution Photomosiac Surveys Of A Chemosynthetic Clam Community In Monterey Canyon*. 2014.

[4] Thor I. Fossen. *Handbook of Marine Craft Hydrodynamics and Motion Control*. John Wiley & Sons, Ltd, 2011. ISBN: 9781119991496. DOI: 10.1002/9781119994138.

[5] Paul D. Groves. *Principles of GNSS, Inertial, and Multisensor Integrated Navigation Systems, Second Edition*. Artech House, 2013, p. 800. ISBN: 1608070050.

[6] IHC Marine and Mineral Projects. *Subsea Mining Crawlers*. URL: http://www.ihcmmp.com/mining/offshore-mining/subsea-mining-crawlers/ (visited on 05/01/2015).

[7] IMCA. *Guidance on Subsea Metrology*. London, 2012. URL: http://www.imca-int.com/media/70581/imcas019.pdf.

[8] James C Kinsey, Ryan M Eustice, and Louis L Whitcomb. "A survey of underwater vehicle navigation: Recent advances and new challenges". In: *IFAC Conference of Manoeuvering and Control of Marine Craft*. 2006.

[9] Tom Kwasnitschka et al. “Doing fieldwork on the seafloor: Photogrammetric techniques to yield 3D visual models from ROV video”. In: *Computers & Geosciences* 52 (Mar. 2013), pp. 218–226. ISSN: 00983004. DOI: 10.1016/j.cageo.2012.10.008. URL: http://www.sciencedirect.com/science/article/pii/S0098300412003482.

[10] Mikael Bliksted Larsen. “Autonomous navigation of underwater vehicles”. PhD. Technical University of Denmark, 2001.

[11] P. Newman and J. Leonard. “Pure range-only sub-sea SLAM”. In: *2003 IEEE International Conference on Robotics and Automation* 2 (2003), pp. 1921–1926. ISSN: 1050-4729. DOI: 10.1109/ROBOT.2003.1241875.

[12] J Padial, S G Dektor, and S M Rock. “Correlation of Imaging Sonar Acoustic Shadows and Bathymetry for ROV Terrain-Relative Localization”. In: *MTS/IEEE OCEANS Conference*. Taipei, Taiwan, 2014. URL: https://web.stanford.edu/group/arl/sites/default/files/public/publications/PadialDR2014.pdf.

[13] Alejandro Palmeiro et al. “Underwater radio frequency communications”. In: *OCEANS 2011 IEEE - Spain*. IEEE, June 2011, pp. 1–8. ISBN: 978-1-4577-0086-6. DOI: 10.1109/Oceans-Spain.2011.6003580.

[14] Autun Purser et al. “Temporal and spatial benthic data collection via an internet operated Deep Sea Crawler”. In: *Methods in Oceanography* 5 (2013), pp. 1–18. ISSN: 22111220. DOI: 10.1016/j.mio.2013.07.001.

[15] A.P. Scherbatyuk. “The AUV positioning using ranges from one transponder LBL”. In: *’Challenges of Our Changing Global Environment’. Conference Proceedings. OCEANS ’95 MTS/IEEE*. Vol. 3. IEEE, 1995, pp. 1620–1623. ISBN: 0-933957-14-9. DOI: 10.1109/OCEANS.1995.528728.

[16] Dan Simon. *Optimal State Estimation: Kalman, H-infinity, and Nonlinear Approaches*. John Wiley & Sons, Inc, 2006, pp. 1–526. ISBN: 0471708585. DOI: 10.1002/0470045345.

[17] *Sonardyne International Ltd.* URL: http://www.sonardyne.com.

[18] A. R. Talukder et al. “High-resolution, deep tow, multichannel seismic and sidescan sonar survey of the submarine mounds and associated BSR off Nicaragua pacific margin”. In: *Marine Geology* 241.1-4 (2007), pp. 33–43. ISSN: 00253227. DOI: 10.1016/j.margeo.2007.03.002.

[19] Sebastian Thrun and John J. Leonard. “Simultaneous localization and mapping”. In: *Springer handbook of robotics* (2008), pp. 871–889. DOI: 10.1007/978-3-540-30301-5_38.

[20] David Titterton. *Strapdown Inertial Navigation Technology, 2nd Edition*. IET, 2004, p. 558. ISBN: 0863413587.

[21] The Free Encyclopedia Wikipedia. *Guidance, navigation and control*. 2015. (Visited on 05/01/2015).

[22] Are B. Willumsen, Oddvar Hallingstad, and Bjørn Jalving. "Integration of range, bearing and doppler measurements from transponders into underwater vehicle navigation systems". In: *Oceans 2006* Dvl (2006). DOI: 10.1109/OCEANS.2006.306851.

Part II

Publications

Paper A

IMU Calibration and Validation in a Factory, Remote on Land and at Sea

Authors:
Martin J. Jørgensen, Dario Paccagnan, Mikael B. Larsen and Niels K. Poulsen

Presented at:
IEEE/ION Position Location and Navigation Symposium 2014.

IMU Calibration and Validation in a Factory, Remote on Land and at Sea

Martin J. Jørgensen[1], Dario Paccagnan[1], Mikael B. Larsen[2] and Niels K. Poulsen[1]

Abstract

This paper treats the IMU calibration and validation problem in three settings: Factory production line with the aid of a precision multi-axis turntable, in-the-field on land and at sea, both without specialist test equipment. The treatment is limited to the IMU calibration parameters of key relevance for gyro-compassing grade optical gyroscopes and force-rebalanced pendulous accelerometers: Scale factor, bias and sensor axes misalignments. Focus is on low-dynamic marine applications e.g., subsea construction and survey.

Two different methods of calibration are investigated: Kalman smoothing using an Aided Inertial Navigation System (AINS) framework, augmenting the error state Kalman filter (ESKF) to include the full set of IMU calibration parameters and a least squares approach, where the calibration parameters are determined by minimizing the magnitude of the INS error differential equation output.

A method of evaluating calibrations is introduced and discussed. The two calibration methods are evaluated for factory use and results compared to a legacy proprietary method as well as in-field calibration/verification on land and at sea.

The calibration methods shows similar navigation performance as the proprietary method. This validates both methods for factory calibration. Furthermore it is shown that the AINS method can calibrate in-field on land and at sea without the use of a precision multi-axis turntable.

[1]Department of Applied Mathemantics and Computer Science, Technical University of Denmark, DK-2800 Kgs. Lyngby, Denmark
[2]Sonardyne International Ltd., Yateley, United Kingdom

A.1 Introduction

The core of a strap-down Inertial Navigation System (INS) is an Inertial Measurement Unit (IMU) which is composed of gyroscope and accelerometer triads mounted along nominally orthogonal axes. This paper treats the IMU calibration and validation problem in three substantially different settings:

- Factory production line with the aid of a precision multi-axis turntable.
- On land without specialist test equipment.
- At sea without specialist test equipment.

The treatment is limited to the IMU calibration parameters of key relevance for gyro-compassing grade optical gyroscopes and force-rebalanced pendulous accelerometers: Scale factor, bias and sensor axes misalignments. The latter are determined with respect to precision machined mounting fixtures on the IMU housing enabling easy in the field system replacement. Furthermore, this paper focuses on the low-dynamic marine domain such as subsea survey and construction using Autonomous Underwater Vehicles (AUVs) and Remotely Operated Vehicles (ROVs), and as a supplement to Global Navigation Satellite System (GNSS) to satisfy the redundancy requirements of Dynamic Positioning (DP) drill ships and semi-submersible platforms. Calibration methods for other types of IMU sensor including more complex sensor models for higher dynamics can be found in [A5, A7].

The three settings considered are vastly different. Factory calibration using a multi-axis precision turntable benefit from effectively perfect knowledge of absolute orientation, position, (zero) velocity, angular rate and local gravity. Orientation can be controlled arbitrarily to approximately 0.001° accuracy, although some restrictions are imposed if using a dual axis table. Per the nature of the domain, some marine inertial systems are frequently subjected to rough transport, handling and harsh operational conditions. Other systems may be in continuous operation for years. This introduces a special need to reliably validate and calibrate INS performance at customer storage facilities on land or at times offshore. At typical customer sites on land, the reference observation set is limited to fixed position, zero velocity and zero angular rate, relative to Earth. Orientation can be controlled via manual handling and the read-out of the INS itself but no reference is available. At sea the reference observations are severely limited. Approximate position can be provided by GNSS or from knowledge of DP station keeping at a fixed location. Position accuracy is limited by antenna lever arm uncertainty or DP (wave) excursions away from the reference location.

An overview of the different frames used for navigation in this paper is given

in section A.2. Two different methods of calibration are investigated. Both relies on the principle of INS given in section A.3: Kalman smoothing using a conventional AINS framework, augmenting the ESKF to include the full set of IMU calibration parameters is given in section A.4, also investigated in [A5]; and a conventional batch least squares optimization approach in section A.5, where the calibration parameters are determined by minimizing the magnitude of the INS error differential equation output. This technique has been proposed by [A1, A3] for similar IMU sensors.

Section A.6 describes the experimental calibration set-up that forms the basis of the analysis. A method of evaluating calibrations is introduced and discussed in section A.7. The two calibration methods are evaluated for factory use and results compared to in-field calibration/verification on land and at sea in section A.8. The calibration trajectory used was chosen to compare a legacy proprietary method with the two presented herein. Alternatively, the trajectory could be chosen as in [A3] or even optimized for observability of the estimated parameters as partly examined in [A4, A8]. The presented methods are compared and advantages over other methods are discussed in section A.9.

A.2 Reference Frames

The inertial sensor triads gives rise to two non-orthogonal reference frames. Besides the inertial sensor frames the following frames are used in this paper [A10]:

- i Inertial frame. Origin is at the center of the Earth with the z-axis coincident with Earth's rotation axis.
- e Earth frame, with origin at the center of the Earth, z-axis coincident with Earth's rotation axis and x-axis through the Greenwich meridian where it intersects the equatorial plane. The e-frame rotates about the z-axis, with respect to the i-frame, at a rate of Ω.
- n North–East–Down (NED) local geographic navigation frame. Rotates with respect to the e-frame with the transport rate, $\boldsymbol{\omega}_{\mathrm{en}}$, which is dependent on motion of the position with respect to Earth.
- b IMU body frame. This is the post-calibrated orthogonal IMU axis set.
- m orientation "sensor" NED local geographic navigation frame. This is not necessarily coincident with the n-frame.

The rotation from b-frame to n-frame can be expressed with the direction cosine matrix (DCM) $\boldsymbol{C}_{\mathrm{b}}^{\mathrm{n}}$. If the DCM is derived from a small angle approximation,

also known as the cross-product form, the notation $\boldsymbol{\delta C}^{\mathrm{n}}_{\mathrm{b}} = \boldsymbol{\Psi} = [\boldsymbol{\psi}\times]$, is used, where $\boldsymbol{\psi}$ is the equivalent vector form.

If a vector expressed in b-frame, y^{b}, is to be converted to n-frame, the DCM can be used: $y^{\mathrm{n}} = \boldsymbol{C}^{\mathrm{n}}_{\mathrm{b}} y^{\mathrm{b}}$. This notation is used throughout this paper. Furthermore, the quantity can be explicitly represented e.g., $\boldsymbol{\omega}^{\mathrm{n}}_{\mathrm{en}}$ which means that it is the rotation rate of the e-frame with respect to the n-frame, expressed in n-frame.

A.3 Inertial Navigation

An INS allows any vehicle to be positioned, in the short term, precisely without having to rely on models of vehicle dynamic. Earth bound navigation using a strap-down IMU can be described with a set of ordinary differential equations (ODEs), derived from the laws of motion within moving coordinate frames. For the chosen n-frame mechanization, the inertial navigation equations (INEs), velocity $\boldsymbol{v}$, position $\boldsymbol{p}$ and orientation $\mathrm{C}^{\mathrm{n}}_{\mathrm{b}}$, can be written as

$$\dot{\boldsymbol{v}}^{\mathrm{n}}_{\mathrm{e}} = [v_{\mathrm{N}} \; v_{\mathrm{E}} \; v_{\mathrm{D}}]^{\top} \tag{A.1}$$

$$= \underbrace{\mathrm{C}^{\mathrm{n}}_{\mathrm{b}} \boldsymbol{f}^{\mathrm{b}}}_{\text{Inertial}} - \underbrace{(2\boldsymbol{\omega}^{\mathrm{n}}_{\mathrm{ie}} + \boldsymbol{\omega}^{\mathrm{n}}_{\mathrm{en}}) \times \boldsymbol{v}^{\mathrm{n}}_{\mathrm{e}}}_{\text{Coriolis}} + \underbrace{\boldsymbol{g}^{\mathrm{n}}_{\mathrm{l}}}_{\text{Local gravity}} \tag{A.2}$$

$$\dot{\boldsymbol{p}}^{\mathrm{n}}_{\mathrm{e}} = [L \; \ell \; d]^{\top} \tag{A.3}$$

$$= \left[\underbrace{\frac{v_{\mathrm{N}}}{R_0 - d}}_{\text{Latitude}} \; \underbrace{\frac{v_{\mathrm{E}} \sec L}{R_0 - d}}_{\text{Longitude}} \; \underbrace{- v_{\mathrm{d}}}_{\text{Height}} \right]^{\top} \tag{A.4}$$

$$\dot{\mathrm{C}}^{\mathrm{n}}_{\mathrm{b}} = \mathrm{C}^{\mathrm{n}}_{\mathrm{b}} \boldsymbol{\Omega}^{\mathrm{b}}_{\mathrm{nb}} \; , \tag{A.5}$$

following the notation of [A10], with

$\boldsymbol{f}^{\mathrm{b}}$	specific force as observed by the accelerometers, in $\mathrm{m/s^2}$
v_{N}	local horizontal velocity the in North direction in m/s
v_{E}	local horizontal velocity the in East direction in m/s
v_{D}	vertical velocity in the down direction in m/s
L	latitude in radians
ℓ	longitude in radians
d	depth in meters from mean sea level of the reference ellipsoid
R_0	radius of the reference ellipsoid at equator, in meters
$\mathrm{C}^{\mathrm{n}}_{\mathrm{b}}$	platform orientation, direction cosine matrix (DCM) from b-frame to n-frame, with the Euler angles $[\alpha \; \beta \; \gamma]^{\top}$

$\boldsymbol{\Omega}_{\text{nb}}^{\text{b}}$ rotation rate of the n-frame with respect to the b-frame, in rad/s. Calculated from the navigation frame rate $\boldsymbol{\Omega}_{\text{in}}$ and from the absolute body rate $\boldsymbol{\Omega}_{\text{ib}}$ observed by the gyroscopes
$\boldsymbol{g}_{\text{l}}^{\text{n}}$ local gravity vector, in m/s^2. Often simplified to $[0\ 0\ g]^\top$.

The IMU together with the INEs makes up the core of an INS. The INS outputs the *navigation state*; the three dimensional position, attitude, heading, and velocity. Any navigation state can be found by performing dead-reckoning navigation from the previous state. The dead-reckoning navigation can be performed by propagating the IMU measurements through the INEs.

It requires a good initial navigation state for these non-linear equations to work properly, since they are highly dependent on position and orientation. In order to simplify the INS algorithms, the orientation is initialized with an attitude and heading reference system (AHRS). This is a simple, robust and self contained system. The AHRS determines North by use and sensing of the Earth's gravitational acceleration and rotation.

Ultimately, the goal of any IMU calibration is to minimize the navigation errors.

A.4 AINS framework

Dead-reckoning navigation inhibits poor long term precision performance and will eventually drift off due to sensor errors, modeling errors, initial errors, etc. Errors propagate through the INEs and build up over time according to the navigation error equations [A6, A10]:

$$\dot{\boldsymbol{\delta\psi}} = -\boldsymbol{\omega}_{\text{in}}^{\text{n}} \times \boldsymbol{\psi} + \boldsymbol{\delta\omega}_{\text{in}}^{\text{n}} - \text{C}_{\text{b}}^{\text{n}} \boldsymbol{\delta\omega}_{\text{ib}}^{\text{b}} \tag{A.6}$$

$$\begin{aligned} \dot{\boldsymbol{\delta v}}_{\text{e}}^{\text{n}} = {} & [\boldsymbol{f}^{\text{n}}\times]\, \boldsymbol{\psi} + \text{C}_{\text{b}}^{\text{n}} \boldsymbol{\delta f}^{\text{b}} - (2\boldsymbol{\omega}_{\text{ie}}^{\text{n}} + \boldsymbol{\omega}_{\text{en}}^{\text{n}}) \times \boldsymbol{\delta v}_{\text{e}}^{\text{n}} \\ & - (2\boldsymbol{\delta\omega}_{\text{ie}}^{\text{n}} + \boldsymbol{\delta\omega}_{\text{en}}^{\text{n}}) \times \boldsymbol{v}_{\text{e}}^{\text{n}} - \boldsymbol{\delta g}_{\text{l}}^{\text{n}} \end{aligned} \tag{A.7}$$

$$\dot{\boldsymbol{\delta p}}_{\text{e}}^{\text{n}} = \boldsymbol{\delta v}_{\text{e}}^{\text{n}} \tag{A.8}$$

with

$\boldsymbol{\psi}$ platform misalignment vector $[\delta\alpha\ \delta\beta\ \delta\gamma]^\top$
$\boldsymbol{\delta\omega}_{\text{ib}}^{\text{b}}$ gyroscope measurement error
$\boldsymbol{\delta\omega}_{\text{ie}}^{\text{n}}$ error in Earth's spin rate, which is negligible for navigation purposes
$\boldsymbol{\delta f}^{\text{b}}$ accelerometer measurement error
$\boldsymbol{\delta g}_{\text{l}}^{\text{n}}$ error in the local gravity
$\boldsymbol{\delta v}_{\text{e}}^{\text{n}}$ velocity error

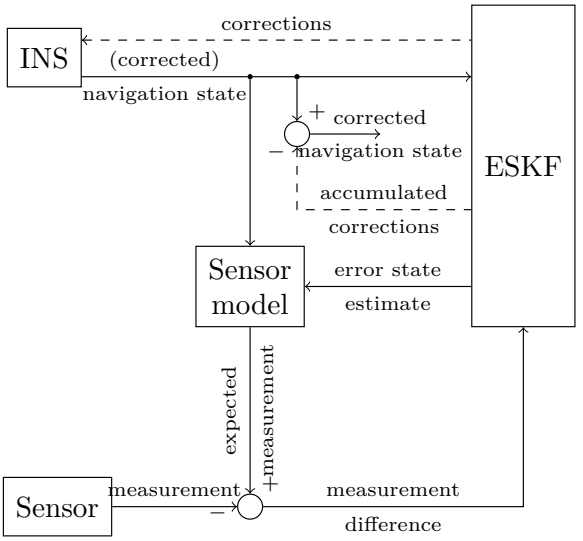

Figure A.1: General AINS framework. The corrections, dashed connections, are either applied to the INS output or alternatively fed back to the INS. If the latter is true, the error state must be reset.

where the last three errors are defined similar to (A.11). These are found e.g., by differencing the estimated INEs and the true INEs.

The complementary properties of extrinsic sensors and the intrinsic can be combined to get the best from both worlds: bounded navigation error with good precision; this is the definition of AINS. An ESKF [A2, A6, A10] framework is used, allowing the estimator to have a slower update rate than the INS, which relaxes requirements for both hardware and algorithms. The states in the ESKF are models of errors, instead of the full states e.g. *estimated depth error* compared to *estimated depth*. Since the INS errors are evolving much slower than the navigational dynamics, it makes sense to make the computational harder estimation task only track the errors. Fig. A.1 shows such a processing framework. Aiding sensors make navigation state errors observable. The difference between the expected and the actual observation is fed into the ESKF. The estimated navigational state errors are used as INE corrections. The corrections can be fed back to the INS to let the INS deal with correcting the navigation state. Alternatively the ESKF accumulated corrections can be used to correct the INS navigation state. In the former set-up the ESKF resets the error state vector to zero every time a correction is given to the INS.

An extended Kalman filter (EKF) [A2] is employed, as the system is non-linear,

here expressed in state-space form

$$\dot{\boldsymbol{x}}(t) = \boldsymbol{f}(\boldsymbol{x}, \boldsymbol{u}_{\mathrm{d}}, t) + \boldsymbol{g}(\boldsymbol{u}, t) \tag{A.9}$$

$$\boldsymbol{z}(t) = \boldsymbol{h}(\boldsymbol{x}, t) + \boldsymbol{v}(t)\ . \tag{A.10}$$

The EKF requires knowledge of a nominal state, $\boldsymbol{x}^*$, in order to estimate the true state. The nominal state is defined as being equal to the true state plus an error

$$\boldsymbol{\delta x} = \boldsymbol{x} - \boldsymbol{x}^*. \tag{A.11}$$

Since the goal is to estimate INS errors, the nominal state is the INS navigation state. Linearizing the system in (A.9) and (A.10) with respect to the nominal state gives

$$\boldsymbol{\delta}\dot{\boldsymbol{x}}(t) = \boldsymbol{F}\boldsymbol{\delta x}(t) + \boldsymbol{G}\boldsymbol{u}(t) \tag{A.12}$$

$$\boldsymbol{\delta z}(t) = \boldsymbol{H}\boldsymbol{\delta x}(t) + \boldsymbol{v}(t), \tag{A.13}$$

where δ denotes error state and observation error, both from the navigation state, and $\boldsymbol{F}$, $\boldsymbol{G}$ and $\boldsymbol{H}$ are formed from the partial derivatives of $\boldsymbol{f}$, $\boldsymbol{g}$ and $\boldsymbol{h}$, respectively, with respect to $\boldsymbol{x}$; all evaluated in the nominal state. With this linearized system the EKF estimates the error state, $\boldsymbol{\delta}\hat{\boldsymbol{x}}$ and the associated estimation error covariance $\boldsymbol{P}$. it should be emphasized that the EKF should be operating close to the linearization point to minimize non-linear effects.

The resulting parameters are refined by using the Rauch-Tung-Striebel (RTS) fixed interval smoothing technique [A2]. For offline processing the RTS interval spans the entire data set, thus making two passes, one forward and one backward. The backward pass is effectively running the KF backwards in time, with the a priori information coming from the forward pass.

A.4.1 IMU sensor error models

The ESKF can be used as a parameter estimator for e.g. sensor error models, by augmenting the navigational state-space model:

$$\boldsymbol{\delta x}' = \left[\frac{\boldsymbol{\delta x}_{\mathrm{nav}}}{\boldsymbol{\delta x}_{\mathrm{sens}}}\right] \tag{A.14}$$

$$\boldsymbol{\delta}\dot{\boldsymbol{x}}'(t) = \boldsymbol{f}'(\boldsymbol{\delta x}'(t)) + \boldsymbol{g}'(\boldsymbol{u}'(t)), \tag{A.15}$$

where prime, $'$, denotes augmented quantities. Gauss-Markov processes are commonly used for error modeling in ESKFs as they only require a single state, are

easy to implement and versatile. A first order Gauss–Markov process, with time-constant τ and variance σ^2, is exponentially-correlated and can be described by the system

$$x(0) \sim \mathcal{N}(0, \sigma^2) \tag{A.16}$$

$$\dot{x}(t) = -\frac{1}{\tau}x(t) + \sqrt{\frac{2\sigma^2}{\tau}}u(t), \tag{A.17}$$

where $u(t)$ is unity white noise . This allows modeling the errors as anything from a random constant, $\tau = \infty$, to almost zero time auto-correlation for $\tau \to 0$ i.e., every sample independently and identically Normal-distributed.

Both the gyroscopes and the accelerometers are modeled as having biases, scale-factor errors and axis misalignment errors, all modeled as first order Gauss–Markov processes. For the calibration problem these are all modeled as random constants. These are applied to the IMU to correct the output with fixed parameters. Unmodeled effects and degradation is accounted for by estimating some or all of the IMU sensor errors as time-varying parameters, when navigating using AINS. These values should be much smaller than the calibrated values for the type of inertial sensors discussed in this article; not necessarily true for other sensor types.

The errors are defined such that the observed quantity ($\widetilde{\ }$) equals the truth plus an error (δ). Thus, the accelerometer model defined as:

$$\widetilde{\boldsymbol{f}}^{\mathrm{b}} = \boldsymbol{f}^{\mathrm{b}} + \boldsymbol{\delta f}^{\mathrm{b}} = \boldsymbol{f}^{\mathrm{b}} + \left(\boldsymbol{\delta f}^{\mathrm{b}}_{\mathrm{bias}} + \boldsymbol{\delta M}_{\mathrm{a}}\boldsymbol{f}^{\mathrm{b}}\right), \tag{A.18}$$

where $\boldsymbol{f}^{\mathrm{b}}$ is the true specific force in body frame,

$$\boldsymbol{\delta f}^{\mathrm{b}}_{\mathrm{bias}} = \begin{bmatrix} \delta f_{\mathrm{bias,x}} \\ \delta f_{\mathrm{bias,y}} \\ \delta f_{\mathrm{bias,z}} \end{bmatrix} \tag{A.19}$$

the accelerometer biases with each element modeled with a variance $\sigma^2_{\mathrm{abias}}$ and

$$\boldsymbol{\delta M}_{\mathrm{a}} = \begin{bmatrix} \delta m^{\mathrm{a}}_{11} & \delta m^{\mathrm{a}}_{12} & \delta m^{\mathrm{a}}_{13} \\ \delta m^{\mathrm{a}}_{21} & \delta m^{\mathrm{a}}_{22} & \delta m^{\mathrm{a}}_{23} \\ \delta m^{\mathrm{a}}_{31} & \delta m^{\mathrm{a}}_{32} & \delta m^{\mathrm{a}}_{33} \end{bmatrix}, \tag{A.20}$$

with the the diagonal elements modeled with the variance σ^2_{asfe} and the off-diagonal elements σ^2_{ama}. Note that $\boldsymbol{\delta M}_{\mathrm{acc}}$ contains both the sensor axes misalignments and the scale-factor errors, which is seen in the structure of the associated variances. Note that this resembles the cross-product form for small angle approximations, but is not quite the same. Also, using this model the diagonal terms will contain a contribution from physical axis misalignments and scale factor errors.

It should be clear that the Gauss–Markov process, (A.17), only affects its own state in (A.14). The coupling into the navigation states are found by applying the sensor error model to the navigation error equations. Taking (A.7) and ignoring products of errors, the tiny contribution from the Coriolis error term and substituting (A.18) in gives:

$$\boldsymbol{\delta\dot{v}}_{\mathrm{e}}^{\mathrm{n}} = [\boldsymbol{f}^{\mathrm{n}}\times]\,\boldsymbol{\psi} + \mathrm{C}_{\mathrm{b}}^{\mathrm{n}}\boldsymbol{\delta f}_{\mathrm{bias}}^{\mathrm{b}} + \mathrm{C}_{\mathrm{b}}^{\mathrm{n}}\boldsymbol{\delta M}_{\mathrm{acc}}\boldsymbol{f}^{\mathrm{b}} \tag{A.21}$$

Equation (A.21) is linearized, when using EKF, to find the couplings in the state transition matrix

$$\begin{aligned}\frac{\partial\boldsymbol{\delta\dot{v}}_{\mathrm{e}}^{\mathrm{n}}}{\partial\boldsymbol{\delta f}^{\mathrm{b}}} &= \frac{\partial\begin{bmatrix}\delta\dot{v}_{\mathrm{N}} & \delta\dot{v}_{\mathrm{E}} & \delta\dot{v}_{\mathrm{D}}\end{bmatrix}^{\top}}{\partial\begin{bmatrix}\delta f_{\mathrm{bias,x}} & \delta f_{\mathrm{bias,y}} & \delta f_{\mathrm{bias,z}} & \delta m_{11}^{\mathrm{a}} & \cdots & \delta m_{33}^{\mathrm{a}}\end{bmatrix}^{\top}} \\ &= \mathrm{C}_{\mathrm{b}}^{\mathrm{n}}\begin{bmatrix}\mathrm{I}_{\mathbf{3}} & \mathrm{I}_{\mathbf{3}}f_x & \mathrm{I}_{\mathbf{3}}f_y & \mathrm{I}_{\mathbf{3}}f_z\end{bmatrix},\end{aligned} \tag{A.22}$$

where $\mathrm{I}_{\mathbf{3}}$ is the 3x3 identity matrix.

Similarly, the gyroscope sensor model is defined:

$$\widetilde{\boldsymbol{\omega}}_{\mathrm{ib}}^{\mathrm{b}} = \boldsymbol{\omega}_{\mathrm{ib}}^{\mathrm{b}} + \boldsymbol{\delta\omega}_{\mathrm{ib}}^{\mathrm{b}} = \boldsymbol{\omega}_{\mathrm{ib}}^{\mathrm{b}} + \left(\boldsymbol{\delta\omega}_{\mathrm{ib,bias}}^{\mathrm{b}} + \boldsymbol{\delta M}_{\mathrm{g}}\boldsymbol{\omega}_{\mathrm{ib}}^{\mathrm{b}}\right), \tag{A.23}$$

with $\boldsymbol{\omega}_{\mathrm{ib}}^{\mathrm{b}}$ being the true angular velocity of the body frame with respect to the inertial frame, expressed in body frame,

$$\boldsymbol{\delta\omega}_{\mathrm{ib,bias}}^{\mathrm{b}} = \begin{bmatrix}\delta\omega_{\mathrm{bias,x}} \\ \delta\omega_{\mathrm{bias,y}} \\ \delta\omega_{\mathrm{bias,z}}\end{bmatrix} \tag{A.24}$$

the gyroscope biases with each element modeled with a variance $\sigma_{\mathrm{gbias}}^2$ and

$$\boldsymbol{\delta M}_{\mathrm{g}} = \begin{bmatrix}\delta m_{11}^{\mathrm{g}} & \delta m_{12}^{\mathrm{g}} & \delta m_{13}^{\mathrm{g}} \\ \delta m_{21}^{\mathrm{g}} & \delta m_{22}^{\mathrm{g}} & \delta m_{23}^{\mathrm{g}} \\ \delta m_{31}^{\mathrm{g}} & \delta m_{32}^{\mathrm{g}} & \delta m_{33}^{\mathrm{g}}\end{bmatrix}, \tag{A.25}$$

with the the diagonal elements modeled with the variance σ_{gsfe}^2 and the off-diagonal elements σ_{gma}^2. Taking (A.6) and ignoring products of errors and substituting with (A.23)

$$\boldsymbol{\delta\dot{\psi}} = -\boldsymbol{\omega}_{\mathrm{in}}^{\mathrm{n}} \times \boldsymbol{\psi} + \boldsymbol{\delta\omega}_{\mathrm{in}}^{\mathrm{n}} - \mathrm{C}_{\mathrm{b}}^{\mathrm{n}}\boldsymbol{\delta\omega}_{\mathrm{ib,bias}}^{\mathrm{b}} - \mathrm{C}_{\mathrm{b}}^{\mathrm{n}}\boldsymbol{\delta M}_{\mathrm{g}}\boldsymbol{\omega}_{\mathrm{ib}}^{\mathrm{b}}, \tag{A.26}$$

yields the system combined equation. Again, the gyroscope error states influence on the navigation states are found by linearizing (A.26):

$$\begin{aligned}\frac{\partial\boldsymbol{\delta\dot{\psi}}}{\partial\boldsymbol{\delta\omega}_{\mathrm{ib}}^{\mathrm{b}}} &= \frac{\partial\begin{bmatrix}\delta\dot{\alpha} & \delta\dot{\beta} & \delta\dot{\gamma}\end{bmatrix}^{\top}}{\partial\begin{bmatrix}\delta\omega_{\mathrm{bias,x}} & \delta\omega_{\mathrm{bias,y}} & \delta\omega_{\mathrm{bias,z}} & \delta m_{11}^{\mathrm{g}} & \cdots & \delta m_{33}^{\mathrm{g}}\end{bmatrix}^{\top}} \\ &= -\mathrm{C}_{\mathrm{b}}^{\mathrm{n}}\begin{bmatrix}\mathrm{I}_{\mathbf{3}} & \mathrm{I}_{\mathbf{3}}\omega_{\mathrm{ib,x}}^{\mathrm{b}} & \mathrm{I}_{\mathbf{3}}\omega_{\mathrm{ib,y}}^{\mathrm{b}} & \mathrm{I}_{\mathbf{3}}\omega_{\mathrm{ib,z}}^{\mathrm{b}}\end{bmatrix},\end{aligned} \tag{A.27}$$

where $\mathbf{I_3}$ is the 3x3 identity matrix. The similarity between (A.22) and (A.27) is expected since the sensor models are identical and as both couple sensor errors into identical state dynamic, i.e., accelerometer to velocity and gyroscope to angular velocity.

A.4.2 Factory observations

The AINS is initialized with knowledge of the absolute orientation and position. Knowledge of local gravity is used to adjust the depth, so it fits with the reference frame, WGS-84 in this case.

Whenever stationary the AINS is aided by orientation from the turn table, mean depth and zero velocity. The two latter are pseudo sensors. They provide aiding information, but relies on the operator to satisfy/verify the assumptions. In case these assumptions does not hold true and the aiding is enabled, the ESKF will be provided with wrongful information that "can not escape". So once the information is there it will flow to the least observable states, leading to estimation errors perhaps even loss of integrity i.e., when the true estimation error is not consistent with the propagated covariance.

A.4.2.1 Orientation

An orientation sensor observes the body frame orientation with respect to the orientation sensor local navigation frame, that is $\mathrm{C}_{\mathrm{b}}^{\mathrm{m}}$. The actual orientation observation is taken from the reference platform, the two-axis turntable, although the following mechanization is general in nature.

$$\widetilde{\mathrm{C}}_{\mathrm{b}}^{\mathrm{m}} = \left[\begin{bmatrix} \alpha_{\mathrm{att}} \\ \beta_{\mathrm{att}} \\ \gamma_{\mathrm{att}} \end{bmatrix} \times \right] + w_{\mathrm{att}}, \tag{A.28}$$

where $w_{\mathrm{att}} \sim \mathcal{N}(\mathbf{0}, \mathrm{I}_3 \sigma_{\mathrm{att}})$. The related expected observation is given by

$$\widehat{\mathrm{C}}_{\mathrm{b}}^{\mathrm{m}} = \widehat{\mathrm{C}}_{\mathrm{n}}^{\mathrm{m}} \widehat{\mathrm{C}}_{\mathrm{b}}^{\mathrm{n}}. \tag{A.29}$$

The estimated navigation frame orientation with respect to the orientation sensor local navigation frame is defined as

$$\widehat{\mathrm{C}}_{\mathrm{n}}^{\mathrm{m}} = [\mathrm{I}_3 - \boldsymbol{\Sigma}]\, \mathrm{C}_{\mathrm{n}}^{\mathrm{m}}, \tag{A.30}$$

where $\boldsymbol{\Sigma} = [\boldsymbol{\varsigma}\times]$ and

$$\boldsymbol{\varsigma} = \begin{bmatrix} \delta\alpha_{\mathrm{att}} \\ \delta\beta_{\mathrm{att}} \\ \delta\gamma_{\mathrm{att}} \end{bmatrix} \tag{A.31}$$

are small misalignment angles modeled as Gauss–Markov processes with variance σ^2_{att}. The ESKF observation is modeled as the small misalignment angles between the estimated and observed orientation,

$$\boldsymbol{\delta}\mathrm{C}_{\mathrm{n}}^{\mathrm{m}} = \mathrm{I}_3 - \widehat{\mathrm{C}}_{\mathrm{b}}^{\mathrm{m}}\mathrm{C}_{\mathrm{b}}^{\mathrm{m}\top}, \tag{A.32}$$

which comes from the definition of orientation errors i.e., same as (A.30). Expanding and ignoring products of errors

$$\begin{aligned}\boldsymbol{\delta}\mathrm{C}_{\mathrm{n}}^{\mathrm{m}} &= \mathrm{I}_3 - \widehat{\mathrm{C}}_{\mathrm{n}}^{\mathrm{m}}\widehat{\mathrm{C}}_{\mathrm{b}}^{\mathrm{n}}\mathrm{C}_{\mathrm{b}}^{\mathrm{m}\top} \\ &= \mathrm{I}_3 - [\mathrm{I}_3 - \boldsymbol{\Sigma}]\,\mathrm{C}_{\mathrm{n}}^{\mathrm{m}}\,[\mathrm{I}_3 - \boldsymbol{\Psi}]\,\mathrm{C}_{\mathrm{b}}^{\mathrm{n}}\mathrm{C}_{\mathrm{b}}^{\mathrm{m}\top} \\ &\approx \mathrm{C}_{\mathrm{n}}^{\mathrm{m}}\boldsymbol{\Psi}\mathrm{C}_{\mathrm{n}}^{\mathrm{m}\top} + \boldsymbol{\Sigma}\end{aligned} \tag{A.33}$$

or on vector form

$$\boldsymbol{\delta\xi} = \mathrm{C}_{\mathrm{n}}^{\mathrm{m}}\boldsymbol{\psi} + \boldsymbol{\varsigma}, \tag{A.34}$$

where $\boldsymbol{\delta\xi}$ is the misalignment angles corresponding to the DCM $\boldsymbol{\delta}\mathrm{C}_{\mathrm{n}}^{\mathrm{m}}$. The corresponding observation matrix is found by linearizing (A.34),

$$\boldsymbol{H}(\boldsymbol{\psi}, \boldsymbol{\varsigma}) = \frac{\partial \boldsymbol{\delta\xi}}{\partial \boldsymbol{\delta x}} = \begin{bmatrix}\mathrm{C}_{\mathrm{n}}^{\mathrm{m}} & \mathrm{I}_3\end{bmatrix}, \tag{A.35}$$

which is trivial in this case.

A.4.2.2 Zero velocity

If completely stationary an observation of zero velocity, relative to Earth, is a rather good approximation. This is also known as zero velocity update (ZUPT). The observed zero velocity is simply

$$\tilde{\boldsymbol{v}}^{\mathrm{n}} = \mathbf{0}, \tag{A.36}$$

and the expected observation

$$\hat{\boldsymbol{v}}^{\mathrm{n}} = \mathbf{0} + \boldsymbol{\delta v}^{\mathrm{n}}, \tag{A.37}$$

with $\boldsymbol{\delta v}^{\mathrm{n}}$ modeled as with a variance of σ^2_{zupt}. The observable difference is simply

$$\begin{aligned}\boldsymbol{\delta v}^{\mathrm{n}} &= \hat{\boldsymbol{v}}^{\mathrm{n}} - \tilde{\boldsymbol{v}}^{\mathrm{n}} \\ &= (\mathbf{0} + \boldsymbol{\delta v}^{\mathrm{n}}) - \mathbf{0} \\ &= \boldsymbol{\delta v}^{\mathrm{n}}\end{aligned} \tag{A.38}$$

and the observation matrix

$$\boldsymbol{H}(\boldsymbol{\delta v}^{\mathrm{n}}) = \frac{\partial \boldsymbol{\delta v}^{\mathrm{n}}}{\partial \boldsymbol{\delta x}} = \mathrm{I}_3. \tag{A.39}$$

As seen from (A.38) and (A.39) the ESKF estimate is directly the estimation error, with corresponding noise.

A.4.2.3 Mean depth

With ZUPT aiding the position drift of the AINS is minimized, but the vertical channel is unstable [A6, A10] will diverge if not aided. Using the same principle as with ZUPT, the observed depth is

$$\tilde{d} \sim \mathcal{N}(d_0, \sigma_\mathrm{d}), \tag{A.40}$$

where d_0 is the constant depth found from the local gravity. With the expected observation

$$\hat{d} = d_0 + \delta d, \tag{A.41}$$

the observable difference is found

$$\begin{aligned} \delta d &= \hat{d} - \tilde{d} \\ &= (d_0 + \delta d) - d_0. \\ &= \delta d \end{aligned} \tag{A.42}$$

The observation matrix is simply

$$\boldsymbol{H}(\delta d) = \frac{\partial \delta d}{\partial \boldsymbol{\delta x}} = 1. \tag{A.43}$$

The final augmented system consists of 36 states: 9 navigation error states, 24 IMU sensor error states and 3 orientation sensor platform misalignment states.

A.4.3 On land

Even without orientation observations, the AINS described in the previous section will be able to calibrate the IMU, but the lacking orientation information makes the IMU housing orientation unobservable and thus indeterminable.

A gravity model must be used, as it is unlikely that the remote site has surveyed local gravity. In order to achieve good estimates for the accelerometer scale-factor errors, a gravity model accounting for the spherical harmonics must be employed. Such models are readily available in public domain. For navigational performance an error in the order of deci-micro-g is insignificant and the models should suffice.

The AINS is initialized with orientation from the AHRS and position from an approximately known fixed position and aided with ZUPT and mean depth. Constant orientation aiding using the knowledge of rotational stationarity, much

like ZUPT, is believed to increase observability of the calibration parameters, but is not being investigated in this paper.

The final augmented system consists of 33 states: 9 navigation error states, 24 IMU sensor error states.

A.4.4 At sea

The only partly known quantities are the horizontal position, and mean depth equal to roughly the mean sea level. The latter is derived in section A.4.2.3.

The position is aided by a GNSS. These vessels tend to place the GNSS receiver as high as possible, operationally resulting in a large sensor lever arm. Errors will be introduced if the lever arm is incorrectly compensated for e.g., erroneous surveyed, if the vessel is unstable.

A.4.4.1 Position

Using the same principle as with ZUPT, the observed position is

$$\widetilde{\boldsymbol{p}} = \boldsymbol{p} = \begin{bmatrix} p_{\text{lat}} \\ p_{\text{lon}} \end{bmatrix} \tag{A.44}$$

where $\boldsymbol{p}$ is the true position. With the expected observation

$$\widehat{\boldsymbol{p}} = \boldsymbol{p} + \boldsymbol{\delta p}, \tag{A.45}$$

where δp_{lat} is modeled with a variance σ^2_{lat} and δp_{lon} with σ^2_{lon}. The observable difference is derived:

$$\begin{aligned} \boldsymbol{\delta p} &= \widehat{\boldsymbol{p}} - \widetilde{\boldsymbol{p}} \\ &= (\boldsymbol{p} + \boldsymbol{\delta p}) - \boldsymbol{p} \\ &= \boldsymbol{\delta p} \end{aligned} \tag{A.46}$$

The observation matrix is simply

$$\boldsymbol{H}(\boldsymbol{\delta p}) = \frac{\partial \boldsymbol{\delta p}}{\partial \boldsymbol{\delta x}} = \mathrm{I}_2. \tag{A.47}$$

The final augmented system consists of 33 states: 9 navigation error states, 24 IMU sensor error states.

A.5 Batch/least squares processing

The fundamental idea behind the least-squares calibration method is adjusting the calibration parameter such that the error of the INEs is minimized rather than directly comparing the IMU sensor output with a computed reference. This technique has the advantage of being robust with respect to errors in the experimental setup. Furthermore, it does not require elaborate IMU sensor noise models unlike the AINS method. The measurable difference in acceleration error for two different IMU orientations is a function of the calibration parameters, as seen from (A.6) and (A.7). If the rotations are carefully chosen, the full set of parameters is observable. In the simplest case, this yields an algebraic system of equations, which can be solved using a least-squares technique [A9]. Alternatively, a larger and more complex set of rotations can be chosen e.g., optimized for observability, and the parameters estimated using optimization. Both approaches assumes that the IMU is stationary relative to Earth, at the start, T_0, and end, T, of each rotation, which greatly simplifies (A.7). Thus, the i'th residual $\boldsymbol{r}_i$ can be written as

$$\boldsymbol{r}_i = \underbrace{\boldsymbol{C}_{\mathrm{b}}^{\mathrm{n}}(T_{0,i})}_{\text{table}} \underbrace{\widetilde{\boldsymbol{f}}^{\mathrm{b}}(T_{0,i})}_{\text{acc.}} - \underbrace{\widehat{\boldsymbol{C}}_{\mathrm{b}}^{\mathrm{n}}(T_i)}_{\text{gyro.}} \underbrace{\widetilde{\boldsymbol{f}}^{\mathrm{b}}(T_i)}_{\text{acc.}} , \tag{A.48}$$

where $\widetilde{\boldsymbol{f}}^{\mathrm{b}}$ are accelerometer measurements, $\boldsymbol{C}_{\mathrm{b}}^{\mathrm{n}}(T_{0,i})$ is the absolute orientation from the turn table at the beginning of the rotation and $\widehat{\boldsymbol{C}}_{\mathrm{b}}^{\mathrm{n}}(T_i)$ the INS estimated orientation at the end of the rotation. The IMU measurements are compensated applying current parameter estimates before any calculations. The gyroscope sensor errors will propagate through the estimated orientation in (A.48), making all IMU sensor errors observable in the residual.

The optimization problem for the calibration parameter set $\boldsymbol{\theta}$ is then formulated as:

$$\arg\min_{\boldsymbol{\theta}} \|\boldsymbol{r}\|_2^2 , \tag{A.49}$$

and solved using classical nonlinear least squares techniques. Note that the minimization of the residuals defined in (A.48) only guarantees internal consistency of the IMU data, but does not estimate the IMU sensor orientation with respect to a predetermined external frame of reference e.g., the IMU housing. If the value of the gravity vector $\boldsymbol{g}$ is known with sufficient precision, then minimizing the (new) residuals

$$\tilde{\boldsymbol{r}}_i = \begin{bmatrix} \boldsymbol{C}_{\mathrm{b}}^{\mathrm{n}}(T_{0,i})\widetilde{\boldsymbol{f}}^{\mathrm{b}}(T_{0,i}) - \boldsymbol{g}^{\mathrm{n}} \\ \widehat{\boldsymbol{C}}_{\mathrm{b}}^{\mathrm{n}}(T_{\infty,i})\widetilde{\boldsymbol{f}}^{\mathrm{b}}(T_{\infty,i}) - \boldsymbol{g}^{\mathrm{n}} \end{bmatrix} , \tag{A.50}$$

allows also to determine the orientation of the sensors with respect to the table frame of reference.

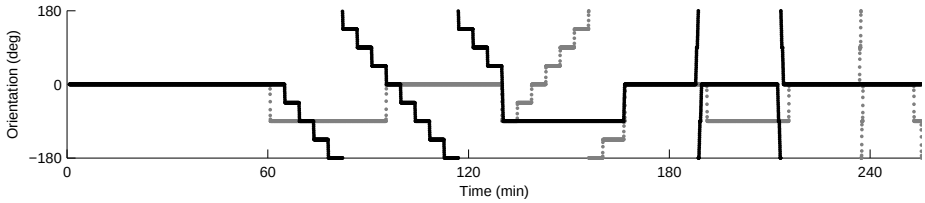

Figure A.2: Calibration fixture, two-axis turn table, example rotation sequence. Black is the inner axis and gray the outer axis.

The least-squares approach is only used for the factory setting. Major rework would be necessary to make it work for the other settings, as it is not as easily reconfigured for different observations as the AINS.

A.6 Calibration set-up

The basis of the calibration is experimental data from six IMUs on a two-axis turn table. The pre-calibrated 100 Hz IMU data is collected after the coning and sculling algorithm [A6, A10] is applied. The IMUs are undergoing a rotation sequence similar to that in Fig. A.2. This sequence of rotations can be realized in all three settings, either by hand or with help of a fixture. Having the reference data from the table serves as a mean to evaluate the calibration methods in all settings.

For the factory setting the table orientation is available for the calibration methods, as well as surveyed local gravity. Both the AINS and the least-squares methods are compared to a third proprietary calibration method. This method does not determine the IMU sensor orientation with respect to the IMU housing, but it does ensure an orthogonal calibrated body frame.

Note that the processing for the on land and at sea settings does not require the IMU to follow the referenced example trajectory absolutely, as only the stationary periods matter.

Using the data sets for the at sea setting is justified by the fact that large vessels with DP systems in calm waters have negligible attitude motion, thus any GNSS lever arm errors will have no influence. GNSS observations are simulated by taking the table position and adding 30 cm white noise.

Gyroscope biases are not calibrated for all methods and all settings, due to small

biases for the available IMUs.

All calibration methods output the calibration parameter set and produces pertaining compensated IMU data.

A.7 Evaluation

Evaluating the navigational performance of IMU calibrations is non-trivial due to different definitions of e.g., calibrated body frame. A calibration should be penalized if the calibrated body frame is non-orthogonal, but not if it is not calibrated to IMU housing frame. An evaluation method using calibrated IMU data is presented in this section.

Two metrics are evaluated: the navigation frame misalignment and the acceleration error in navigation frame. Evaluating errors in navigation frame makes comparison easier than dealing with different definitions of body frame. The references are the IMU motion from the calibration platform and the surveyed gravity, respectively.

The IMU body frame orientation with respect to the navigation frame, $\boldsymbol{C}_{\mathrm{b}}^{\mathrm{n}}[t]$, is found by running ZUPT aided INS. The initial orientation and position are taken from the reference platform. The body frames of the platform and the IMU might not be perfectly aligned. Additionally the available calibration fixture had a small but unknown heading misalignment. Consequently the platform orientation reference, $\boldsymbol{C}_{\mathrm{bp}}^{\mathrm{np}}[t]$, can not be directly compared to $\boldsymbol{C}_{\mathrm{b}}^{\mathrm{n}}[t]$. These misalignments are small and constant throughout the entire procedure, and are fitted with the residuals

$$\boldsymbol{r}_{\mathrm{att}}[t] = \boldsymbol{C}_{\mathrm{b}}^{\mathrm{n}}[t] \left[\boldsymbol{C}_{\mathrm{np}}^{\mathrm{n}}(\gamma_{\mathrm{np}}) \boldsymbol{C}_{\mathrm{bp}}^{\mathrm{np}}[t] \boldsymbol{C}_{\mathrm{b}}^{\mathrm{bp}}(\theta_{\mathrm{bp}}) \right]^{\top}, \tag{A.51}$$

where the Euler angle γ_{np} is the heading difference and $\theta_{\mathrm{bp}} = \begin{bmatrix} \alpha_{\mathrm{bp}} & \beta_{\mathrm{bp}} & \gamma_{\mathrm{bp}} \end{bmatrix}^{\top}$ the body frame misalignments. The minimization problem

$$\underset{\{\gamma_{\mathrm{np}}, \theta_{\mathrm{bp}}\}}{\arg\min} \left\| \boldsymbol{j}(\boldsymbol{r}_{\mathrm{att}}) \right\|_2^2, \tag{A.52}$$

with function $\boldsymbol{j}$ resolving the residuals into Euler angles and taking the 2-norm of the three Euler elements, is solved by a conventional non-linear least-squares algorithm. Running the AINS as part of the minimization increases the execution time immensely, as a result a slightly different approach is used. Running the AINS with an initial heading error will converge with time, so using RTS smoothing on the result gives an improved initial heading. This mitigates the

initial heading error effect on the AINS and the optimization executes fast. The appertaining root–mean–square–error (RMSE) is calculated as the RMS of the minimized residuals of (A.51), for stationary periods.

The navigation frame acceleration error is evaluated by resolving the body frame output of the accelerometers, $\boldsymbol{\Delta v}^{\mathrm{b}}$, into navigation frame using the gyroscopes

$$\boldsymbol{\Delta v}^{\mathrm{n}}[t] = \boldsymbol{C}_{\mathrm{b}}^{\mathrm{n}}[t]\boldsymbol{\Delta v}^{\mathrm{b}}[t], \tag{A.53}$$

and compensated for gravity

$$\boldsymbol{\delta a}^{\mathrm{n}}[t] = \frac{\boldsymbol{\Delta v}^{\mathrm{n}}[t]}{\Delta T_{\mathrm{IMU}}} - \begin{bmatrix} 0 \\ 0 \\ g \end{bmatrix}, \tag{A.54}$$

where ΔT_{IMU} is the IMU sample interval. Taking the RMSE of the magnitude of the acceleration will unfairly weight longer stationary periods more than shorter periods. Both problems are mitigated by taking the mean of $\boldsymbol{\Delta v}^{\mathrm{n}}$ for each stationary period, weighting each period equally, before calculating the RMSE.

A.8 Results

The calibration methods are evaluated according to the metrics defined in section A.7, using the set-up described in section A.6.

Table A.1 and A.2 shows orientation and acceleration performance, respectively, for the factory calibration setting. In this setting the two calibration methods described in this paper has been verified against a third proprietary calibration method. Calibration performance for the on land setting is shown in table A.3 and at sea in table A.4.

Comparing the results shows that all three methods perform similarly for the factory setting. Furthermore, it is also seen that the performance of the AINS method performs almost identically in all three settings.

A.9 Conclusion

Analyzing the results from the experimental data shows that both methods presented herein can be used to achieve high accuracy for factory calibration.

Table A.1: Attitude and heading performance for factory setting.

	Orientation RMSE (mili-°)		
IMU#	AINS	NLSQ	Proprietary
1	10.7668	11.0004	12.8470
2	20.3281	20.9816	21.9415
3	26.6626	26.1676	27.4034
4	22.3295	23.0129	22.6769
5	28.8444	27.5539	25.1533
6	26.3689	26.5847	26.5428
Mean	22.5500	22.5502	22.7608

Table A.2: Acceleration performance for factory setting.

	Acceleration RMSE (μg)		
IMU#	AINS	NLSQ	Proprietary
1	16.7683	16.4582	21.9174
2	29.9454	26.5149	29.7009
3	28.5088	22.1025	89.6507
4	33.2744	29.1359	28.2366
5	25.6030	23.4516	31.6360
6	31.9135	30.0562	34.0508
Mean	27.6689	24.6199	39.1987

Table A.3: Calibration performance for on land setting.

	RMSE	
IMU#	Orientation (mili-°)	Acceleration (μg)
1	30.1818	67.6954
2	20.4200	29.8001
3	26.4714	26.8985
4	22.9644	27.8462
5	28.0645	28.9807
6	25.4839	29.7186
Mean	25.5977	35.1566

Table A.4: Calibration performance for at sea setting.

	RMSE	
IMU#	Orientation (mili-$^\circ$)	Acceleration (μg)
1	17.6468	28.5954
2	20.0357	32.6557
3	25.8094	34.5786
4	25.2287	31.4044
5	27.4300	24.9405
6	27.9529	33.9529
Mean	24.0173	31.0213

Furthermore, utilizing two substantially different algorithms is a useful aid in validation of correctness of implementation. Both algorithms are found to perform on par or better than a proprietary and previously used method.

In-the-field calibration on land is shown to be feasible without a multi axis precision turn table, by merely doing a nominally similar series of rotations and leaving the IMU stationary in-between and making use of the flexibility of the AINS KF. Without absolute knowledge of orientation, calibration to the IMU housing is unattainable.

In-field calibration at sea is shown feasible if certain conditions are met. Results shows that the IMU can be field calibrated with just a GNSS receiver and knowledge of local gravity or a good model hereof.

Compared to the least-squares method, the AINS KF approach benefits from the ESKF's ability to process a wide range of external observations. The framework's flexibility allows easy adaptation to the available set of observations for each of the settings. Using the KF covariance matrix to evaluating parameter observability/accuracy and optimizing the sequence of rotations might increase calibration accuracy. A drawback of applying the AINS Kalman filter technique is dependence on accurate IMU sensor noise models. A disadvantage that the least-squares method does not share.

Finally, an evaluation method has been developed that allows for a robust comparison of IMU performance.

References A

[A1] Alison Brown, Robert Ebner, and John Mark. "A Calibration Technique for a Laser Gyro Strapdown Inertial Navigation System". In: *SYMPOSIUM GYRO TECHNOLOGY 1982 conference proceedings* (1982), pp. 12–12.20.

[A2] Robert Grover Brown and Patrick Y. C. Hwang. *Introduction to Random Signals and Applied Kalman Filtering*. 3rd ed. Wiley, 1996, p. 496. ISBN: 0471128392.

[A3] J DIESEL. "Calibration of a ring laser gyro inertial navigation system". In: *Test Group(6585 th), 13 th Biennial Guidance Test ...* I (1987).

[A4] M. Grewal. "Optimal selection of trajectories for parameter estimation in dynamical systems". In: *1982 21st IEEE Conference on Decision and Control*. Vol. 21. IEEE, 1982, pp. 1140–1141. DOI: 10.1109/CDC.1982.268332.

[A5] M.S. Grewal, V.D. Henderson, and R.S. Miyasako. "Application of Kalman filtering to the calibration and alignment of inertial navigation systems". In: *IEEE Transactions on Automatic Control* 36.1 (1991), pp. 3–13. ISSN: 00189286. DOI: 10.1109/9.62283.

[A6] Paul D. Groves. *Principles of GNSS, Inertial, and Multisensor Integrated Navigation Systems, Second Edition*. Artech House, 2013, p. 800. ISBN: 1608070050.

[A7] DK Joos and U.K. Krogmann. "Estimation of strapdown sensor parameters for inertial system error-compensation". In: *... Precision Positioning and Inertial Guidance Sensors ...* (1981).

[A8] Louis J. Lintereur. "Optimal Test Trajectories for Calibrating Inertial Systems". PhD thesis. Massachusetts Institute of Technology, 1996.

[A9] R.M. Rogers. "Applied mathematics in integrated navigation systems". In: *AIAA Education series* (2003).

[A10] David Titterton. *Strapdown Inertial Navigation Technology, 2nd Edition*. IET, 2004, p. 558. ISBN: 0863413587.

Paper B

Subsea Metrology Using SLAM sparse LBL Acoustically Aided INS

Authors:
Martin J. Jørgensen, Mikael B. Larsen and Niels K. Poulsen

Submitted to:
IEEE Journal of Oceanic Engineering 2015.

Subsea Metrology Using SLAM sparse LBL Acoustically Aided INS

Martin J. Jørgensen[1], Mikael B. Larsen[2] and Niels K. Poulsen[1]

Abstract

This paper investigates and experimentally determines the feasibility of performing subsea metrology via a combination of Simultaneous Localization And Mapping (SLAM) techniques and Acoustically Aided INS (AAINS) technology. In this context, subsea metrology is principally the task of determining the slant range between two subsea structures as a means for onshore construction of an interconnecting section of pipe. Accuracy (5–15 cm) and integrity requirements are stringent since incorrect measurement, fabrication and subsequent misfit is exceedingly expensive. Conventional metrology use transponders to compute the distance between structures from measurement of two-way acoustic time of flight. 4 transponders placed in a braced quadrilateral configuration are needed to provide redundancy for QC.

We describe how use of SLAM, AAINS and Kalman smoothing can meet requirements with just 2 transponders, one placed on each structure. A Remotely Operated Vehicle (ROV) is equipped with a high-end commercial grade Doppler-Inertial dead-reckoning based navigation system. While maneuvering, the ROV uses a Long Baseline (LBL) acoustic transceiver to periodically measure its distance to the two transponders. Using the two transponders for navigation while simultaneously determining their unknown, but fixed, (relative) positions is a simple example of SLAM. Obtainable accuracy and its dependency on the ROV trajectory and key sensor parameters is investigated.

Two sea trials were performed to obtain important high fidelity experimental validation of the proposed method. Independently performed conventional full braced quadrilateral acoustic metrology provides a trusted reference. The experimental results are shown to

[1]Department of Applied Mathemantics and Computer Science, Technical University of Denmark, DK-2800 Kgs. Lyngby, Denmark
[2]Sonardyne International Ltd., Yateley, United Kingdom

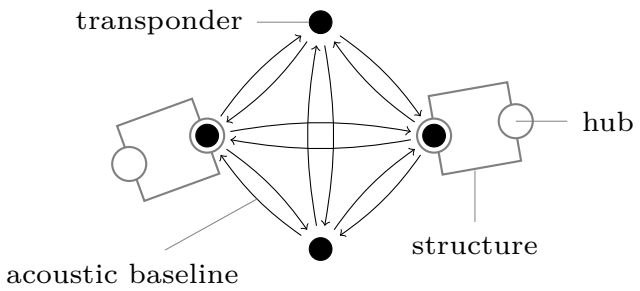

Figure B.1: Conventional acoustic metrology set-up with transponders in a braced quadrilateral configuration.

be consistent with expectations from Monte Carlo and covariance simulation and are robustly within requirements, i.e. $\ll$ 5–15 cm. The paper holds some concluding remarks on practical considerations, potential time efficiency gains and limitations of the investigated method.

B.1 Introduction

IN the offshore hydrocarbon construction industry, subsea structures often need to be connected with sections of rigid pipe. The pipe (or "jumper") is manufactured onshore, transported offshore and fitted to the two subsea structures. Ensuring accurate measurements is paramount, as it can be a costly operation to repeat. Known as *subsea metrology*, these surveys generally determine relative orientation, seabed profile and the distance between two structures. In this paper, subsea metrology is referred to as: The subsea surveying discipline of measuring the distance between two hubs, i.e. hub baseline. Typical required hub–hub relative position accuracies are 5–15 cm in each axis [B4]. The surveyors require means of validating the accuracy by some amount of redundancy.

Subsea metrologies generally employ an acoustic transponder array, known as LBL. Ranges are computed from measurements of the two-way travel-time between transceiver and transponder, or transponder and transponder, and from knowledge of the speed of sound. LBL positioning relies on trilateration with an array of minimum three transponders. The array is calibrated by collecting baselines between all transponders in the array and measuring the relative transponder depths.

For metrology, an array of four transponders is commonly used for redundancy to enable detection of an incorrectly measured baseline. The braced quadrilateral configuration, as shown in Fig. B.1, is commonly used where acoustic line-of-sight is not a problem. The acoustic baselines form a hub–hub baseline least-squares problem. Depth differences are determined by using a pressure depth sensor in a closed loop to points of interest, which allows the slant range to be resolved into horizontal and vertical components.

INS is seeing increasing use in the offshore industry. One concept for inertial metrology is based on bounding INS drift by performing periodic Zero velocity UPdaTeS (ZUPTs), with the INS being held completely stationary. This concept can be made to work, but requires use of a very high performance INS (stringent export restrictions) and a large amount of difficult manual ROV manipulation carrying the INS back and forth between hubs a number of times [B1, B3]. This solution effectively handles non-line-of-sight surveys and minimizes the amount of equipment, but struggles with large surveys, as accuracy depends on time elapsed and time between ZUPTs.

We describe how use of SLAM, AAINS and Kalman smoothing can meet requirements with just 2 transponders, one placed on each structure. A ROV is equipped with a high-end commercial grade Doppler-Inertial dead-reckoning based navigation system. While maneuvering, the ROV uses a LBL acoustic transceiver to periodically measure its distance to the two transponders. Using the two transponders for navigation while simultaneously determining their unknown, but fixed, (relative) positions is a simple example of SLAM. Obtainable accuracy and its dependency on the ROV trajectory and key sensor parameters is investigated.

This paper investigates a two-transponder hybrid acoustic-inertial indirect method of inferring the hub–hub baseline. One transponder is placed at either end of the hub-hub baseline. The transponder position difference and hence sought-after slant range is determined via combination of SLAM techniques with concept known as “sparse” or “synthetic” LBL [B8–B10, B13]. Sparse LBL utilize a ROV dead reckoning navigation means, ROV motion and acoustic range measurements to just one or a few seabed transponders with known positions to provide accurate and bounded navigation. The dead-reckoning means is typically a Doppler Velocity Log (DVL) and pressure depth sensor AAINS. The DVL measures ROV vehicle frame velocity relative to the seabed to a typical accuracy of a few mm/sec [B5]. In SLAM sparse-LBL one or more partly unknown, but fixed, seabed transponder positions can be determined relative to one, or more, reference transponders by maneuvering the ROV while doing acoustic ranging. Due to the stringent accuracy requirements for metrology, great care must be taken when modeling and implementing the AAINS. Integrity, the truthfulness of the stated accuracy of the solution, is paramount to ensure that the strict

requirements are met.

This paper is organized by first giving a description of subsea metrology and introduction to state-of-the-art AAINSs in section B.2, followed by a discussion in section B.3 about the baseline calculation. Section B.4 discusses trajectory design and results are presented in section B.5. Finally, a conclusion is given in section B.6, along with a discussion of the results.

B.2 Conventional strapdown AAINS mechanization

An INS is a dead-reckoning system that allows any vehicle to be navigated accurately in the short term, without having to rely on models of vehicle dynamics. Motion is sensed by three accelerometers and three gyroscopes inside the INS, referred to as the Inertial Measurement Unit (IMU). In a strapdown system, the IMU follows the motion of the vehicle, i.e. unlike mechanical stable-platform inertial systems. Linear acceleration and angular rate measured by the IMU is integrated to velocity $\boldsymbol{v}$, position $\boldsymbol{p}$ and orientation $\mathrm{C}_{\mathrm{b}}^{\mathrm{n}}$ according to e.g. [B3, B12]:

$$\dot{\boldsymbol{v}}_{\mathrm{e}}^{\mathrm{n}} = \frac{\mathrm{d}\left[v_{\mathrm{N}}\ v_{\mathrm{E}}\ v_{\mathrm{D}}\right]^{\top}}{\mathrm{d}t} \tag{B.1}$$

$$= \underbrace{\mathrm{C}_{\mathrm{b}}^{\mathrm{n}}\boldsymbol{f}^{\mathrm{b}}}_{\text{Inertial}} - \underbrace{(2\boldsymbol{\omega}_{\mathrm{ie}}^{\mathrm{n}} + \boldsymbol{\omega}_{\mathrm{en}}^{\mathrm{n}}) \times \boldsymbol{v}_{\mathrm{e}}^{\mathrm{n}}}_{\text{Coriolis}} + \underbrace{\boldsymbol{g}_{\mathrm{l}}^{\mathrm{n}}}_{\text{Local gravity}} \tag{B.2}$$

$$\dot{\boldsymbol{p}}_{\mathrm{e}}^{\mathrm{n}} = \frac{\mathrm{d}\left[L\ \ell\ d\right]^{\top}}{\mathrm{d}t} \tag{B.3}$$

$$= \left[\underbrace{\frac{v_{\mathrm{N}}}{R_{\mathrm{N}} - d}}_{\text{Latitude}}\ \underbrace{\frac{v_{\mathrm{E}} \sec L}{R_{\mathrm{E}} - d}}_{\text{Longitude}}\ \underbrace{-v_{\mathrm{d}}}_{\text{Height}}\right]^{\top} \tag{B.4}$$

$$\dot{\mathrm{C}}_{\mathrm{b}}^{\mathrm{n}} = \mathrm{C}_{\mathrm{b}}^{\mathrm{n}}\boldsymbol{\Omega}_{\mathrm{ib}}^{\mathrm{b}} - \boldsymbol{\Omega}_{\mathrm{in}}^{\mathrm{n}}\mathrm{C}_{\mathrm{b}}^{\mathrm{n}}\ , \tag{B.5}$$

with

$\boldsymbol{f}^{\mathrm{b}}$	specific force as measured by the accelerometers
v_{N}	velocity in North direction
v_{E}	velocity in East direction
v_{D}	velocity in down direction
L	latitude
ℓ	longitude

d depth

$\mathrm{C}_{\mathrm{b}}^{\mathrm{n}}$ platform orientation, direction-cosine matrix (DCM) from INS body-frame to navigation-frame

$\boldsymbol{\omega}_{\mathrm{ie}}^{\mathrm{n}}$ turn rate of Earth with respect to inertial frame $\begin{bmatrix}\Omega\cos L & 0 & -\Omega\sin L\end{bmatrix}^{\top}$

$\boldsymbol{\omega}_{\mathrm{en}}^{\mathrm{n}}$ turn rate of the navigation frame with respect to the Earth frame, also called transport rate $\begin{bmatrix}\dot{\ell}\cos L & -\dot{L} & -\dot{\ell}\sin L\end{bmatrix}^{\top}$

$\boldsymbol{\Omega}_{\mathrm{nb}}^{\mathrm{b}}$ turn rate of the n-frame with respect to the b-frame. Calculated from the navigation frame rate $\boldsymbol{\Omega}_{\mathrm{in}}$ and from the absolute body rate $\boldsymbol{\Omega}_{\mathrm{ib}}$ measured by the gyroscopes

$\boldsymbol{\Omega}_{\mathrm{ib}}^{\mathrm{b}}$ body rate measured by the gyroscopes

$\boldsymbol{\Omega}_{\mathrm{in}}^{\mathrm{n}}$ skew-symmetric form of the turn rate of the navigation frame with respect to inertial frame $\boldsymbol{\omega}_{\mathrm{in}}^{\mathrm{n}} = \boldsymbol{\omega}_{\mathrm{ie}}^{\mathrm{n}} + \boldsymbol{\omega}_{\mathrm{en}}^{\mathrm{n}}$

$\boldsymbol{g}_{\mathrm{l}}^{\mathrm{n}}$ local gravity vector. Often simplified to $[0\ 0\ g(L,d)]^{\top}$,

and $R_{\mathrm{N}} = \frac{R(1-e^2)}{(1-e^2\sin^2 L)^{3/2}}$, $R_{\mathrm{E}} = \frac{R}{(1-e^2\sin^2 L)^{1/2}}$ with semi-major axis length R and eccentricity of the ellipsoid e, both given by the geodetic model, e.g. WGS-84.

Being a dead-reckoning system, inertial navigation will eventually drift off due to integration of sensor errors, modeling errors, etc. Thus, free inertial metrology is only suitable for relatively short distances and carried out with a high performance IMU. In an AINS, the complementary properties of inertial navigation and other navigation sensors are combined to obtain navigation with good accuracy and bounded error.

The generic framework used to fuse the external aiding sensors with the INS is shown in Fig. B.2. Since INS errors are evolving much slower than the navigational dynamics, it makes sense to make the computationally harder estimation task only track errors. This is the main idea behind the error-state Kalman filter (ESKF) [B2, B3, B12]. The states in the ESKF are models of errors, instead of the full states e.g. *estimated depth error* compared to *estimated depth*. This set-up allows the ESKF to have a slower update rate than the INS, relaxing both hardware and algorithm requirements, while allowing aiding sensor latency to be handled. Errors propagate and build up over time according to the navigation error equations [B3, B12]:

$$\dot{\boldsymbol{\psi}} = -\boldsymbol{\omega}_{\mathrm{in}}^{\mathrm{n}} \times \boldsymbol{\psi} + \boldsymbol{\delta\omega}_{\mathrm{in}}^{\mathrm{n}} - \mathrm{C}_{\mathrm{b}}^{\mathrm{n}}\boldsymbol{\delta\omega}_{\mathrm{ib}}^{\mathrm{b}} \tag{B.6}$$

$$\begin{aligned}\boldsymbol{\delta\dot{v}}_{\mathrm{e}}^{\mathrm{n}} = {} & [\boldsymbol{f}^{\mathrm{n}}\times]\,\boldsymbol{\psi} + \mathrm{C}_{\mathrm{b}}^{\mathrm{n}}\boldsymbol{\delta f}^{\mathrm{b}} - (2\boldsymbol{\omega}_{\mathrm{ie}}^{\mathrm{n}} + \boldsymbol{\omega}_{\mathrm{en}}^{\mathrm{n}}) \times \boldsymbol{\delta v}_{\mathrm{e}}^{\mathrm{n}} \\ & - (2\boldsymbol{\delta\omega}_{\mathrm{ie}}^{\mathrm{n}} + \boldsymbol{\delta\omega}_{\mathrm{en}}^{\mathrm{n}}) \times \boldsymbol{v}_{\mathrm{e}}^{\mathrm{n}} - \boldsymbol{\delta g}_{\mathrm{l}}^{\mathrm{n}}\end{aligned} \tag{B.7}$$

$$\boldsymbol{\delta\dot{p}}_{\mathrm{e}}^{\mathrm{n}} = \boldsymbol{\delta v}_{\mathrm{e}}^{\mathrm{n}} \tag{B.8}$$

with

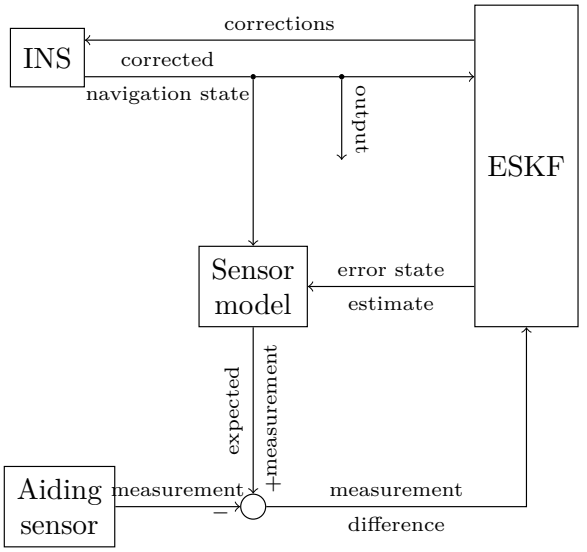

Figure B.2: General AINS framework. The corrections are either fed back to the INS, or alternatively applied to the INS output. If the former is true, the error state must be reset for each feedback. INS output is the *navigation state*: position, velocity, orientation, turn rate and acceleration.

$[\boldsymbol{v}\times]$	Skew-symmetric form of the vector $\boldsymbol{v}$
$\boldsymbol{\psi}$	platform misalignment vector $[\delta\alpha\ \delta\beta\ \delta\gamma]^\top$
$\boldsymbol{\delta\omega}_{\mathrm{ib}}^{\mathrm{b}}$	gyroscope measurement error
$\boldsymbol{\delta\omega}_{\mathrm{ie}}^{\mathrm{n}}$	error in Earth's spin rate, which is negligible for navigation purposes
$\boldsymbol{\delta f}^{\mathrm{b}}$	accelerometer measurement error
$\boldsymbol{\delta g}_{\mathrm{l}}^{\mathrm{n}}$	local gravity error
$\boldsymbol{\delta v}_{\mathrm{e}}^{\mathrm{n}}$	velocity error.

The ESKF dynamic system model and measurement models are

$$\boldsymbol{\delta\dot{x}}(t) = \boldsymbol{f}(\boldsymbol{\delta x}, \boldsymbol{x}, \boldsymbol{u}, t) + \boldsymbol{g}(\boldsymbol{w}, t) \tag{B.9}$$

$$\boldsymbol{z}(t) = \boldsymbol{h}(\boldsymbol{\delta x}, \boldsymbol{x}, t) + \boldsymbol{v}(t)\ , \tag{B.10}$$

with state $\boldsymbol{x}$ (position, velocity, orientation), error-state $\boldsymbol{\delta x}$, stochastic forcing function $\boldsymbol{w}$ from the inertial sensors, deterministic forcing function $\boldsymbol{u}$ from inertial measurements and aiding sensor measurement $\boldsymbol{z}$ with noise $\boldsymbol{v}$. The non-linear functions $\boldsymbol{f}$ and $\boldsymbol{g}$ are given by (B.6)–(B.8); $\boldsymbol{h}$ depends on the aiding sensor(s). As in a regular extended Kalman filter (EKF) the state vector

estimate is propagated by

$$\boldsymbol{\delta\hat{x}}_{k|k-1} = \boldsymbol{\delta\hat{x}}_{k-1|k-1} + \int_{t_{k-1}}^{t_k} \boldsymbol{f}(\boldsymbol{\delta\hat{x}}(t), \hat{\boldsymbol{x}}(t), \boldsymbol{u}(t), t)\,\mathrm{d}t \tag{B.11}$$

and measurement update

$$\boldsymbol{\delta\hat{x}}_{k|k} = \boldsymbol{\delta\hat{x}}_{k|k-1} + \boldsymbol{K}_k\left(\boldsymbol{z}_k - \boldsymbol{h}(\boldsymbol{\delta\hat{x}}_{k|k-1}, \hat{\boldsymbol{x}}_k, t_k)\right) \tag{B.12}$$

with Kalman gain

$$\boldsymbol{K}_k = \boldsymbol{P}_{k|k-1}\boldsymbol{H}_k^\top\left(\boldsymbol{H}_k\boldsymbol{P}_{k|k-1}\boldsymbol{H}_k^\top + \boldsymbol{R}_k\right)^{-1} \tag{B.13}$$

where $\boldsymbol{R}_k$ is the discrete-time measurement covariance and

$$\boldsymbol{H}_k = \left.\frac{\partial \boldsymbol{h}(\boldsymbol{\delta x}, \boldsymbol{x}, t)}{\partial \boldsymbol{\delta x}}\right|_{\boldsymbol{\delta x}=\boldsymbol{\delta\hat{x}}_{k|k-1}}. \tag{B.14}$$

The associated covariance update and projection are

$$\boldsymbol{P}_{k|k} = (\boldsymbol{I} - \boldsymbol{K}_k\boldsymbol{H}_k)\,\boldsymbol{P}_{k|k-1} \tag{B.15}$$

$$\boldsymbol{P}_{k|k-1} = \boldsymbol{A}_k\boldsymbol{P}_{k-1|k-1}\boldsymbol{A}_k + \boldsymbol{Q}_k, \tag{B.16}$$

with the discrete-time time-update covariance $\boldsymbol{Q}_k$ and

$$\boldsymbol{F}_{k-1} = \left.\frac{\partial \boldsymbol{f}(\boldsymbol{\delta x}, \boldsymbol{x}, \boldsymbol{u}, t)}{\partial \boldsymbol{\delta x}}\right|_{\boldsymbol{\delta x}=\boldsymbol{\delta\hat{x}}_{k|k-1}} \tag{B.17}$$

$$\boldsymbol{A}_{k-1} = \exp\left(\boldsymbol{F}_{k-1}(t_k - t_{k-1})\right), \tag{B.18}$$

where the matrix exponential approximation requires that the propagation interval is sufficiently small. It should be emphasized that the ESKF should be operating close to the linearization point to minimize non-linear effects.

The ESKF estimates are refined by Rauch-Tung-Striebel (RTS) fixed-interval smoothing [B2, B3], consisting of the forward filter pass described above, followed by a backward pass. Navigation estimates at any time-point will thereby make use of all past and future information. The backward pass is effectively running the KF backwards in time, with the a priori information coming from the forward pass. Using the measurements from $\boldsymbol{z}_1$ to $\boldsymbol{z}_n$, the optimal estimate $\boldsymbol{\delta\hat{x}}_{k|n}$ $(k < n)$ is given by

$$\boldsymbol{\delta\hat{x}}_{k|n} = \boldsymbol{\delta\hat{x}}_{k|k} + \boldsymbol{C}_k(\boldsymbol{\delta\hat{x}}_{k+1|n} - \boldsymbol{\delta\hat{x}}_{k+1|k}) \tag{B.19}$$

$$\boldsymbol{P}_{k|n} = \boldsymbol{P}_{k|k} + \boldsymbol{C}_k\left(\boldsymbol{P}_{k+1|n} - \boldsymbol{P}_{k+1|k}\right)\boldsymbol{C}_k^\top, \tag{B.20}$$

with

$$\boldsymbol{C}_k = \boldsymbol{P}_{k|k}\boldsymbol{A}_{k+1}^{\top}\boldsymbol{P}_{k+1|k}^{-1} \tag{B.21}$$

The navigational state-space model can be augmented with sensor error models. These help to better capture the uncertainties and estimate both constant and time-varying parameters in the combined system; an accelerometer comes with an inherent scale-factor error that is compensated for during factory calibration, but is also subject to a time-varying scale-factor error. A number of different sensor errors, including white and colored noise, have been rigorously modeled and evaluated against their usefulness, impact and observability. Among these errors are biases, scale-factor errors, lever-arm errors, misalignments, transponder position errors and sound-velocity errors. Aiding-sensor error-modeling is out-of-scope for this paper, but can be found in the AINS literature [B3, B6, B7]. An ESKF for AAINS can easily consist of 30–40 states.

B.2.1 Sparse SLAM LBL AAINS

The concept is to use two transponders, placed in the hubs, for "localization", while simultaneously determining their relative position. Using acoustic transponders with uncertain, but fixed, positions is a SLAM problem [B9], as known from robotics. In this framework it can be solved by picking one transponder as reference, fixing that position, and then estimating the remaining transponder positions. The result is a calibrated array, relative to the reference transponder.

The vertical datum is chosen to be the pressure depth sensor, used to aid the INS. A second pressure depth is used for metrology depth loops, by wielding it in the ROV manipulator. Hence, all transponders' vertical positions are estimated for SLAMBL while allowing for a robust vertical reference. In order for the ESKF to cope with the non-linearities in the positioning problem, the ESKF is run iteratively, correcting only the transponder position at each iteration. Iteratively correcting only the transponder states is not strictly guaranteed to converge. Carefully planning trajectories, see Section B.4, and only allowing a certain amount of transponder position uncertainty ensures convergence[3].

To ensure good relative navigation, the AAINS is aided by a Doppler velocity log (DVL), pressure depth and LBL acoustic ranges. Typical accuracies are given in table B.1.

[3] A non-linear Kalman filter or a least-squares type of method could be used to allow larger uncertainty.

Table B.1: Sensor and typical observation accuracies

Sensor	Observation	Accuracy (σ)	Unit
INS	roll and pitch	0.01	°
INS	heading	0.05[a]	°
DVL	seabed relative velocity	0.2	cm/s
LBL	range	1.5	cm
Depth	pressure depth	0.2[b]	m

[a] scales with $\sec(L)$.
[b] given as 0.01% of full scale; roughly 0.2 m for these trials.

B.3 Inferred baseline accuracy

The hub–hub baseline accuracy is derived from the ESKF covariance, employing a simple trick: similar to the measurement update in (B.13), the covariance matrix is transformed into baseline observation space. The trick is to model a pseudo measurement and derive the corresponding measurement update matrix $\boldsymbol{H}_r$ as in (B.14). $\boldsymbol{H}_r$ is similar to that of other range observations, e.g. LBL observation models [B3, B6, B8, B9, B13][4]. The estimated baseline r and corresponding variance σ_r are given by:

$$r = \|(\boldsymbol{p}_{\text{slam}} - \boldsymbol{\delta p}_{\text{slam}}) - (\boldsymbol{p}_{\text{ref}} - \boldsymbol{\delta p}_{\text{ref}})\| \tag{B.22}$$

$$\sigma_r^2 = \boldsymbol{H}_r \boldsymbol{P} \boldsymbol{H}_r^\top, \tag{B.23}$$

where

$\boldsymbol{p}_{\text{ref}}$ reference transponder position $[x_{\text{ref}}\ y_{\text{ref}}\ z_{\text{ref}}]^\top$
$\boldsymbol{p}_{\text{slam}}$ SLAM transponder position $[x_{\text{slam}}\ y_{\text{slam}}\ z_{\text{slam}}]^\top$
$\boldsymbol{\delta p}_{\text{ref}}$ reference transponder error states in local level frame $[0\ 0\ \delta z_{\text{ref}}]^\top$
$\boldsymbol{\delta p}_{\text{slam}}$ SLAM transponder error states in local level frame $[\delta x_{\text{slam}}\ \delta y_{\text{slam}}\ \delta z_{\text{slam}}]^\top$

and

$$\boldsymbol{H}_r(\boldsymbol{\delta p}_{\text{slam}}, \boldsymbol{\delta p}_{\text{ref}}) = \begin{bmatrix} \boldsymbol{e}^\top & 0 & 0 & -e_z \end{bmatrix}, \tag{B.24}$$

where $\boldsymbol{e} = \begin{bmatrix} e_x & e_y & e_z \end{bmatrix}^\top$ is the unit-vector from $\boldsymbol{p}_{\text{ref}}$ to $\boldsymbol{p}_{\text{slam}}$.

The iterative corrections, which compensate for non-linear effects, are only applied to the estimated transponder error states. As the ESKF covariance is only weakly coupled across iterations, due to non-linearities, it could be used online as an *indication* of offline baseline precision.

[4] $\boldsymbol{H}_r$, in (B.24), can be designed to output any/all of the covariances for both the slant, horizontal and vertical ranges.

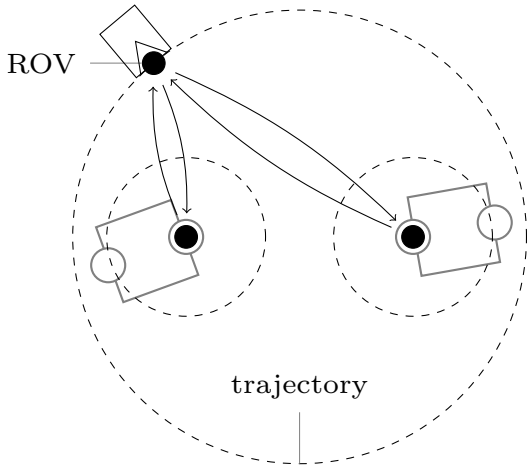

Figure B.3: Trajectory with circles around array and each transponder.

B.4 Trajectories

The ROV trajectory is important in achieving the desired accuracy, since two transponders are insufficient for static relative localization using simple trilateration. The combination of DVL-INS with ranging observations is what provides observability of the partly unknown transponder position.

Errors, e.g. a lever-arm error, can be decoupled from the baseline accuracy by carefully planning the trajectory. Since it is impossible to completely decouple errors from the hub–hub baseline estimate, some error models are still necessary.

The opposite approach is to maximize observability, allowing the error to be estimated as states in the EKF. This has the disadvantage of requiring elaborate models to attain the desired baseline accuracy. However, this approach allows for high accuracy in the presence of significant uncertainty/errors. Information of poor integrity accepted by the filter will generally "hide" in weakly observable states, due to the nature of estimation problems; including too many, or too unobservable, states might result in inferior hub–hub baseline estimate and accuracy.

Two trajectories were chosen bearing in mind both observability and practical ROV maneuvering limitations. The first is a center-facing circular trajectory around the array and around each transponder as illustrated in Fig. B.3. The acoustic transceiver and the transponders are in the same horizontal plane for the large circle; the small circles are elevated in order to make the vertical com-

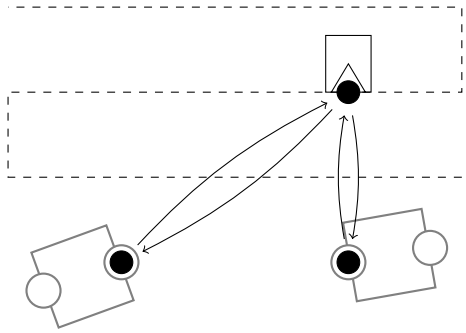

Figure B.4: Meander trajectory with constant heading.

ponent observable. The radii and depths define how observable the horizontal and vertical components are. Close proximity to other structures e.g. risers, operational procedures and control of the ROV umbilical tether can inhibit the ROV in completing a full circle.

The second trajectory is a meander as shown in Fig. B.4. The trajectory plane is placed above the array to resolve both vertical and horizontal components. As with the circular trajectory, this trajectory can be tuned by adjusting the parameters. Good acoustic line-of-sight is ensured by letting the ROV face the general direction of the transponders. The influence of sensor misalignments as well as lever-arm errors is thus minimized. A constant heading also helps the ROV operators follow the trajectory when faced with controlling the umbilical tether, countering currents, watching out for obstacles, etc. As the trajectory only operates on one side of the array, direction-dependent errors like multipath can affect the solution.

B.5 Results

Both simulated and trial data have been used to test and verify the SLAMBL method. Most importantly, the real-world practicality and accuracy have been investigated and experimentally verified. Sea trials are discussed in Section B.5.1 and simulation studies are carried out in both Section B.5.2 and Section B.5.3, regarding the influence of the number of transponders, and an error budget with common uncertainties and errors, respectively.

Figure B.5: Deploying the ROV

B.5.1 Sea trials

Sea trials were carried out for an offshore construction metrology survey in early 2013. Two similar metrologies were carried out using both the circular and meander type trajectories. Full conventional acoustic metrologies, using braced quadrilateral configurations, were performed as part as normal operations and these serve as references.

Data was collected during the offshore subsea metrology trials using a work class ROV. The ROV was equipped with a Sonardyne SPRINT system [B11]: a strap-down INS aided with pressure depth, 3D velocity from a RDI DVL and ranges from a Fusion 6G LBL system and a HiPAP ultra-short baseline (USBL) position system, used to initialize the AAINS position. Note that these trials concurrently tested the acoustic system and operational practices, and thus introduced gaps in the acoustic range data.

The ROV-piloted trajectories for the trials are shown in Figs. B.8–B.11. For the large circle, the ROV depth was kept at the same level as the transponders. The mean height above the transponders for the smaller circles was 5.7 m and 12.3 m for Trial I and II, respectively. The height above the transponders was kept constant at approximately 25 m throughout the meander trajectories. The "clutter" visible on the circular trajectories in Fig. B.8 and Fig. B.9 is due to the ROV pilot unwinding the umbilical tether. This can also be seen to a lesser extent on the meander plots in Fig. B.10 and Fig. B.11. Also, note that the ROV was controlled by different pilots under different environmental circumstances.

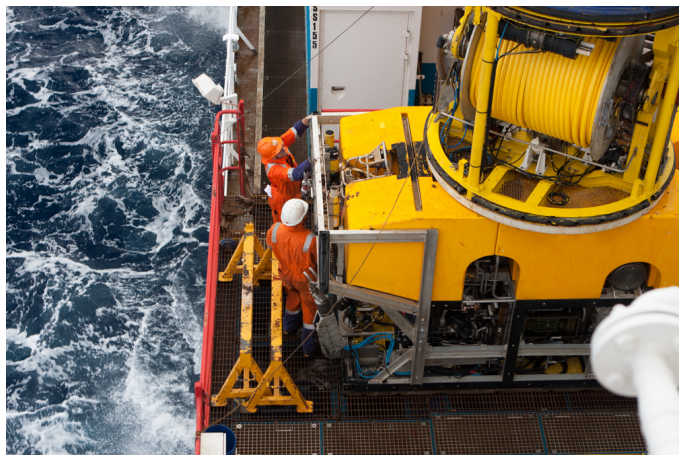

Figure B.6: ROV maintenance

All data sets are post-processed using the same system parameters, initial covariance and transponder position uncertainties. The initial transponder horizontal position uncertainty used is 1 meter distance-root-mean-square (DRMS). Initial transponder vertical position uncertainty is 0.3 meter. The reference transponder has equally uncertain vertical position, as both are fixed to the seabed, but the depth is measured relative to the surface. This gives an inherent correlation in depth between the two transponders which needs to be maintained. The results are presented in Table B.2.

B.5.2 Number of transponders

Using two transponders is the theoretical minimum for this application. Three transponders will provide more information, and with four you might as well be doing a conventional acoustic metrology—except for the cases where multiple transponders are used to overcome lack of line-of-sight.

The effect of using more than two transponders, in a braced quadrilateral configuration, with regards to the estimated baseline standard deviation is shown in Fig. B.12. This simulation was carried out using the circular trajectory with SLAMBL. The initial uncertainty of the transponders is the same as for the trial data processing. As seen, all cases end with subcentimetre std.dev., with the four-transponder solution having marginally lower std.dev.

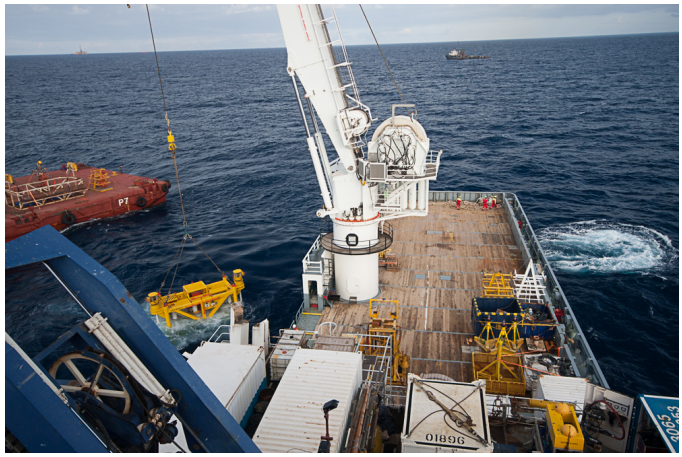

Figure B.7: Crane deploying a subsea structure

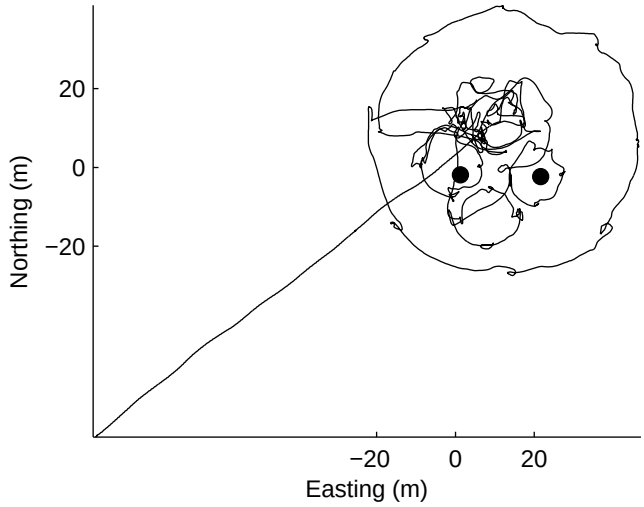

Figure B.8: Trial I circular trajectory with two transponders marked as circles.

B.5.3 Baseline error budget

The dynamics necessary for the SLAMBL to work makes the error propagation complex to grasp as compared to conventional acoustic metrology. Temporal and spatial observation densities, as well as measurement noise, lever-arm errors and misalignments affect the baseline error.

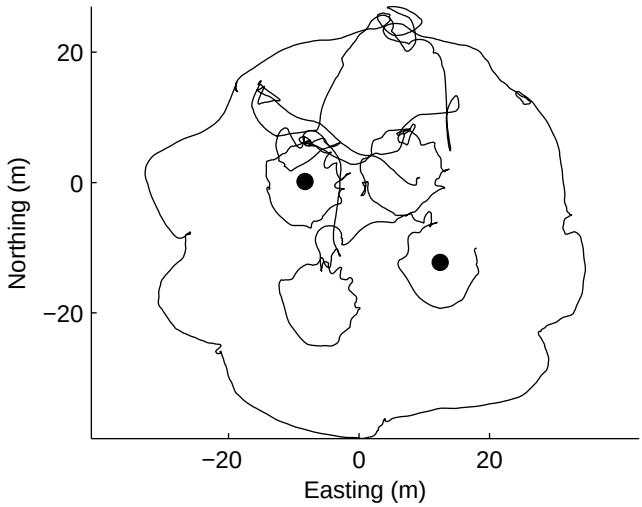

Figure B.9: Trial II circular trajectory with two transponders marked as circles.

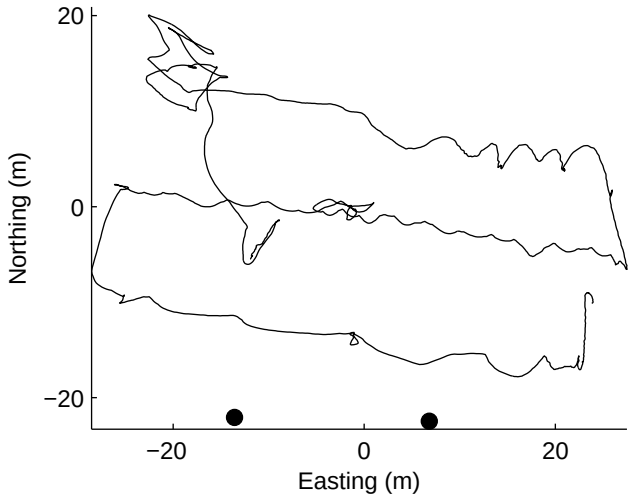

Figure B.10: Trial I meander trajectory with two transponders marked as circles.

The differences in error propagation between the two proposed trajectories are shown in the error budget in Table B.3. IMU and aiding sensor observations were synthesized with realistic noise, using the real-world trajectories from sea trial II.

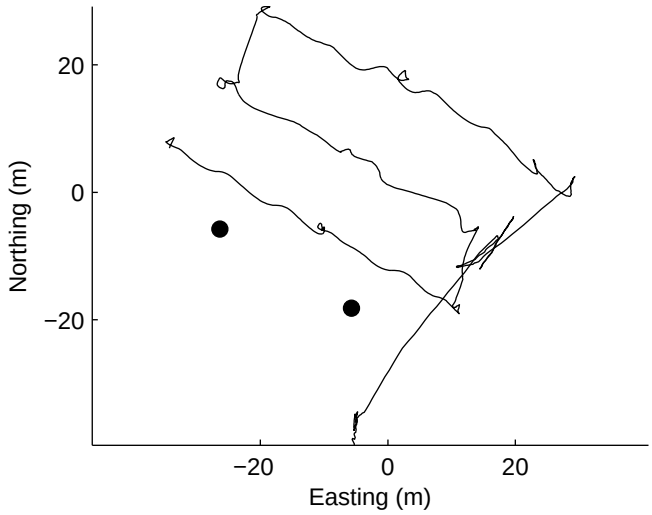

Figure B.11: Trial II meander trajectory with two transponders marked as circles.

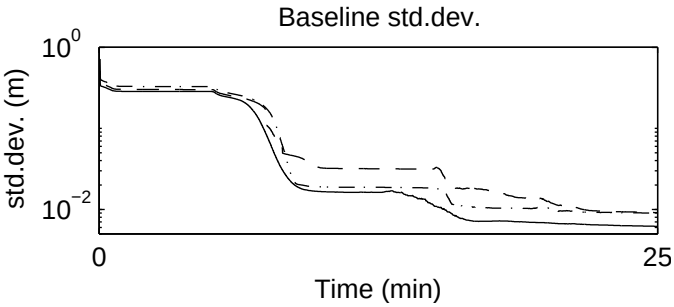

Figure B.12: The dashed, dotted-dashed and solid lines represent the slant range std.dev. for SLAM with two, three and four transponders, respectively. Y-axis is logarithmic.

The noise model parameters in Table B.3 were analyzed using covariance simulation, but have been verified by perturbing the parameters in 50 iteration Monte Carlo simulations. This result is in itself valuable as this verifies the integrity of the SLAMBL solution using realistic trajectories.

Although the resulting accuracy will vary depending on the exact trajectory and set-up, this indicates the influence for a variety of parameters. General error analysis of AINSs and aiding sensors can be found in the literature [B3, B12], and is not treated in this paper. An in-depth analysis of array geometry impact

Table B.2: SLAMBL results compared by trajectory and baseline. σ is the std.dev. of the baseline and Δ the difference between the SLAMBL and the conventional acoustic baseline. The subscripts $_{\mathrm{h}}$ and $_{\mathrm{v}}$ indicate horizontal and vertical baseline components, respectively.

	Baselines			
	Horizontal		Vertical	
Trajectory	σ_{h} (cm)	Δ_{h} (cm)	σ_{v} (cm)	Δ_{v} (cm)
		Trial I		
Circles	1.2	2.1	2.4	0.2
Meander	4.5	3.2	5.2	0.1
		Trial II		
Circles	1.2	2.3	1.8	1.0
Meander	4.4	3.4	5.9	1.3

on navigation with sparse LBL can be found in [B8].

B.6 Conclusion

This paper investigated a combination of SLAM, AAINS and Kalman smoothing (herein dubbed SLAMBL: SLAM BaseLine) for doing subsea metrology using just 2 transponders—a 50 % reduction as compared to conventional acoustic metrology. Transponder relative positions are added to the ROV AAINS Kalman filter via simple state augmentation. While maneuvering, the ROV uses an LBL acoustic transceiver to periodically measure its distance to the two transponders. This achieves "Simultaneous" navigation of the ROV ("Localization") and observability ("Mapping") of the partly unknown, but fixed, transponder position states—SLAM.

A simple and efficient method is given for deriving the transponder–transponder slant range (hub–hub baseline) accuracy from the augmented SLAM AAINS covariance matrix.

Not detailed explicitly, redundancy can be obtained by independent direct transponder–transponder acoustic distance measurement and relative depth measurement, using a pressure depth sensor carried in the ROV robotic manipulator arm.

The accuracy of both AAINS and SLAM is trajectory dependent. Two different trajectory types were suggested and evaluated: a circular trajectory, which ensures good observability of both the horizontal and vertical transponder positions, and thereby the hub–hub baseline; and a meander type trajectory for when the circular trajectory is operationally infeasible. Both trajectories can be adapted to the specific operation by tuning key parameters, such as radius, to ensure required baseline accuracy is met.

Extensive sea trials were performed in realistic full commercial operational conditions. Trusted conventional braced quadrilateral 4-transponder acoustic metrology was independently performed by a specialist survey team and the results used as reference. The accuracy of SLAMBL was experimentally validated to be consistent with simulation results and robustly within the requirements (5–15 cm). The circular trajectory performed best in the trials, achieving accuracies on the order of 2 cm (1 cm) in the horizontal (vertical). The meander trajectory performed slightly worse, as also expected from covariance simulation: ≈ 3 cm (1 cm) horizontal (vertical). Meander-type trajectory performance could likely be improved by more appropriate location of the ROV survey lines relative to the transponders.

The vertical baseline component generally showed very little difference from the reference. This may be a result of overly conservative configuration of the Kalman filter or simply chance.

The effect of using more than 2 transponders was briefly investigated and unsurprisingly accuracy improves. However, for the specific application, this holds insignificant value and saving only one or zero transponders does not justify the increased complexity of adding SLAM AAINS to a metrology solution.

Lastly, an error budget was presented. This shows how variation of key sensor performance parameters and operational conditions affect baseline accuracy. Accuracy is first and foremost dependent on LBL acoustic range measurement noise and measurement rate. The latest generation ("6G") Sonardyne acoustic instruments are easily able to meet 2 cm range noise and ≈ 1 Hz update rate specification. Very interestingly and of significant practical importance, realistic variation of sensor installation parameters (i.e. lever arms and mounting angles) and inertial sensor performance parameters (e.g. gyro/accelerometer bias and noise) show insignificant impact on baseline accuracy. This means that instrument installation tolerances and sensor performance requirements can easily be met in practice. Proprietary performance and configuration parameters for the Sonardyne "SPRINT/JANUS SLAM AAINS Metrology" system was used for generating the bottom most row of the table and can be seen to provide more than adequate accuracy ($\ll$ 5–15 cm).

Some practical remarks: The time spent on doing acoustic baseline measurements for conventional metrology has in practice become insignificant via use of the latest generations of acoustic instruments. Hence, the SLAMBL potential for saving expensive ship time stem solely from having to deploy 2 transponders less on the seabed—this may in some cases save the ROV from doing an extra deep water dive, i.e 1–3 hrs. Time taken for doing the SLAMBL trajectory is not significantly different from that of placing two extra transponders on the sea floor, excluding eventual extra dive time. When placing a transponder in a structure hub, there is risk of a slight misalignment causing an erroneous baseline to be measured. In conventional acoustic metrology this is countered by manually rotating each transponder 3 times in 90 deg increments and redoing the acoustic baseline measurements. This would not be practical for SLAMBL since the ROV trajectory would need to be repeated a total of 8 times. Hence, practical use of SLAMBL would need to be accompanied by an improved mechanical design of the transponder stab/hub interface.

It would be desirable to show estimates of the hub–hub baseline accuracy in real-time, allowing the operator to break off ROV maneuvering when sufficient data has been recorded.

[5]

References B

[B1] Frederic Auger and Keith Vickery. "The operational evaluation of an inertial navigation technique for the provision of underwater metrology surveys". In: *Underwater Technology: The International Journal of the Society for Underwater* 30.2 (Nov. 2011), pp. 103–112. ISSN: 17560543. DOI: 10.3723/ut.30.103.

[B2] Robert Grover Brown and Patrick Y. C. Hwang. *Introduction to Random Signals and Applied Kalman Filtering*. 3rd ed. Wiley, 1996, p. 496. ISBN: 0471128392.

[B3] Paul D. Groves. *Principles of GNSS, Inertial, and Multisensor Integrated Navigation Systems, Second Edition*. Artech House, 2013, p. 800. ISBN: 1608070050.

[B4] IMCA. *Guidance on Subsea Metrology*. London, 2012. URL: http://www.imca-int.com/media/70581/imcas019.pdf.

[5] Note that identifying company stickers were removed from select photos.

[B5] Bjørn Jalving et al. "DVL velocity aiding in the HUGIN 1000 integrated inertial navigation system". In: *Modeling, Identification and Control* 25.4 (2004), pp. 223–235. ISSN: 03327353. DOI: 10.4173/mic.2004.4.2.

[B6] Martin J. Jørgensen, Mikael B. Larsen, and Niels K. Poulsen. "Approaching cm-level relative accuracy in underwater navigation". unpublished. 2015.

[B7] Martin J. Jørgensen et al. "IMU calibration and validation in a factory, remote on land and at sea". In: *2014 IEEE/ION Position, Location and Navigation Symposium - PLANS 2014*. IEEE, May 2014, pp. 1384–1391. ISBN: 978-1-4799-3320-4. DOI: 10.1109/PLANS.2014.6851514.

[B8] Mikael Bliksted Larsen. "Autonomous navigation of underwater vehicles". PhD. Technical University of Denmark, 2001.

[B9] P. Newman and J. Leonard. "Pure range-only sub-sea SLAM". In: *2003 IEEE International Conference on Robotics and Automation* 2 (2003), pp. 1921–1926. ISSN: 1050-4729. DOI: 10.1109/ROBOT.2003.1241875.

[B10] A.P. Scherbatyuk. "The AUV positioning using ranges from one transponder LBL". In: *'Challenges of Our Changing Global Environment'. Conference Proceedings. OCEANS '95 MTS/IEEE*. Vol. 3. IEEE, 1995, pp. 1620–1623. ISBN: 0-933957-14-9. DOI: 10.1109/OCEANS.1995.528728.

[B11] *Sonardyne International Ltd.* URL: http://www.sonardyne.com.

[B12] David Titterton. *Strapdown Inertial Navigation Technology, 2nd Edition*. IET, 2004, p. 558. ISBN: 0863413587.

[B13] Are B. Willumsen, Oddvar Hallingstad, and Bjørn Jalving. "Integration of range, bearing and doppler measurements from transponders into underwater vehicle navigation systems". In: *Oceans 2006* Dvl (2006). DOI: 10.1109/OCEANS.2006.306851.

Table B.3: Error budget from simulation based on trial II trajectories. Accuracies are calculated from the SLAMBL solution, unless otherwise stated.

			Trajectory					
			Circles			Meander		
Parameter	Value	Unit	σ_{h} (cm)	σ_{v} (cm)	σ_{sr} (cm)	σ_{h} (cm)	σ_{v} (cm)	σ_{sr} (cm)
LBL data gap[a]	60	s	0.80	1.74	0.80	3.15	4.26	3.20
	300	s	0.92	1.83	0.90	3.49	4.63	3.54
LBL ping rate	10	s	1.49	2.40	1.46	4.47	5.78	4.46
$\sigma_{\mathrm{LBL,rms}}$	0.02	m	0.51	1.37	0.52	2.86	3.74	2.94
	0.10	m	1.36	2.29	1.34	4.16	5.07	4.16
$\sigma_{\mathrm{LBL,lev_0}}$	0.05	m	0.79	1.72	0.79	3.13	4.07	3.16
	0.10	m	0.79	1.75	0.79	3.09	4.22	3.13
$\sigma_{\mathrm{DVL,ma_0}}$	0.25	°	0.79	1.72	0.79	3.09	4.19	3.13
	2.00	°	0.80	1.72	0.79	3.06	4.09	3.10
$\sigma_{\mathrm{DVL,lev_0}}$	0.1	m	0.79	1.71	0.79	3.09	4.34	3.16
$\sigma_{\mathrm{pdepth,lev_0}}$	0.05	m	0.79	1.73	0.79	3.03	4.16	3.08
	0.1	m	0.79	1.72	0.79	3.10	4.24	3.15
$\sigma_{\mathrm{acc,rms_0}}$	25	μg	0.78	1.67	0.77	3.00	3.95	3.02
	400	μg	0.86	1.88	0.86	3.62	4.93	3.71
$\sigma_{\mathrm{acc,rw}}$	0.01	m/s/$\sqrt{\mathrm{hr}}$	0.78	1.68	0.78	3.00	4.11	3.06
	0.04	m/s/$\sqrt{\mathrm{hr}}$	0.83	1.82	0.83	3.47	4.82	3.53
$\sigma_{\mathrm{gyro,rms_0}}$	0.005	°/hr	0.79	1.72	0.79	3.08	4.15	3.13
	0.08	°/hr	0.80	1.70	0.79	3.12	4.05	3.14
$\sigma_{\mathrm{gyro,arw}}$	0.005	°/$\sqrt{\mathrm{hr}}$	0.77	1.70	0.76	2.90	4.00	2.94
	0.02	°/$\sqrt{\mathrm{hr}}$	0.84	1.78	0.83	3.48	4.46	3.54
$\sigma_{\mathrm{LBL,lev_0}}$, $\sigma_{\mathrm{DVL,lev_0}}$, $\sigma_{\mathrm{pdepth,lev_0}}$	0.05	cm	0.80	1.73	0.79	3.14	4.25	3.19
SPRINT metrology			0.79	1.73	0.79	3.12	4.00	3.16

[a] gap was uniformly distributed temporally per iteration, for 50 Monte Carlo iterations. Resulting σ is the RMS of all iterations. *Reference* refers to the outcome of a simulation with parameters identical to those used to process the real data.

[b] uniformly distributed per run.

Paper C

Approaching cm-level accuracy in underwater navigation

Authors:
Martin J. Jørgensen, Mikael B. Larsen and Niels K. Poulsen

Submitted to:
IEEE Transactions on Robotics 2015.

Approaching cm-level accuracy in underwater navigation

Martin J. Jørgensen[1], Mikael B. Larsen[2] and Niels K. Poulsen[1]

Abstract

This paper treats an element in realizing cm level accuracy of hybrid subsea navigation systems: automatic parameter estimation of sensor latency, lever arms and mounting angles. Real-Time Kinematic (RTK) GNSS/INS provides cm-level dynamic accuracy for land and aerial surveying. High-frequency electromagnetic signals do not penetrate seawater to an appreciable extent and so subsea navigation is GNSS denied and remains a considerable challenge. Subsea hybrid Acoustically Aided Inertial Navigation Systems (AAINS) routinely achieves decimeter level relative navigation accuracy. Insight suggests potential for future AAINS reaching cm level accuracy via the utilization of modern wideband range/Doppler acoustic signal processing and careful (ultra) tight integration with high performance INS. If made practical, this technology is likely to foster a paradigm shift within subsea survey and construction same as lidar GNSS/INS did for land/air.

The "Work class" Remotely Operated Vehicle (ROV) is used for a host of different tasks, hence payload and sensors are frequently changed. This poses a major challenge since hybrid cm-level accuracy requires very accurate knowledge of individual sensor lever arms and mounting angles. At present, these parameters are often measured manually at sea using ad-hoc tools in a stressed working environment. This paper investigates automated indirect parameter estimation as a means to: improve accuracy, reduce risk of blunders, enhance usability and save ship time. Limited accuracy and reliability in current systems is in part managed by overly conservative tuning of the core AAINS sensor fusion algorithms (Kalman filter). Reliable parameter estimation will hence also indirectly improve navigation accuracy by allowing sharper tuning without risk of loosing filter integrity.

[1]Department of Applied Mathemantics and Computer Science, Technical University of Denmark, DK-2800 Kgs. Lyngby, Denmark

[2]Sonardyne International Ltd., Yateley, United Kingdom

Automated AAINS sensor configuration parameter estimation is investigated using a mixture of non-linear optimization and classic Kalman filter state augmentation. Positive findings are supported by high-fidelity simulation and important experimental validation using data from sea trials performed in representative offshore operational conditions.

C.1 Introduction

UNDERWATER acoustic ranging systems have in recent years advanced into using spread-spectrum[C9, C11], also known as wide-band, signal processing techniques. Current long baseline (LBL) systems state ranging precision of better than 1.5 cm. Similar accuracy depends on knowledge of speed of sound along the acoustic path, and interference/multipath, both are generally low. The focus of this paper is on subsea surveying applications, in which high relative accuracy is required. Cm-level static accuracy have been operational accessible for ages. Dynamic applications are trickier as with movement compensation/resolution, trajectory and timing all are important, as well as the speed of sound along the path and interference may change.

The difficulty increases when trying to aid an inertial navigation system (INS) on a remotely operated vehicle (ROV), equipped with a LBL transceiver ranging to transponders on the seabed. In this scenario, the lever arm from the INS to the transceiver, as well as the transponder positions, must be known. Conventional noise models[C6, C7] are conservative to accommodate robust LBL-aided INS (AINS) navigation, putting more emphasis on the INS than the LBL, leading to decimetric navigation accuracy. Improved error modeling of the entire AAINS is required to achieve centimetric-level relative navigation accuracy. Offshore ROVs often change tools, up to multiple times per day; the crew is limited by both time, tools and weather to correctly measure lever arms and mounting angles. Blunders can easily happen and operators can not be expected nor required to be experts in trouble-shooting Kalman filters.

This paper investigates how to operationally estimate aiding sensor parameters: lever arms, mounting angles and latency. The ROV is equipped with an INS, a pressure depth sensor, a Doppler velocity log (DVL) and a LBL transceiver. The aiding sensors relative placements to the INS are assumed to be unknown. Following the parameter estimation, centimetric-level navigation is shown to be feasible using a two-transponder array, i.e. “sparse” or “synthetic” LBL [C6, C7, C10, C14]. Sparse LBL array calibration is treated in [C4]. Additionally,

the slightly different scenario wherein the DVL and the INS are co-located and pre-calibrated is also treated.

A thorough description of the investigated method is given in Section C.2. Section C.3 describes the AAINS framework, followed by sensor specific modeling in Sections C.5, C.6 and C.7, for pressure depth, DVL, and LBL, respectively. Results are presented in Section C.8. Finally, a conclusion is given in Section C.9 along with a discussion of the results.

C.2 Method overview

We seek to automatically calibrate aiding sensor: estimating lever arms, mounting angles and latency, assuming no prior knowledge of these parameters. The work strives to use only the aiding sensor itself and the IMU for calibration as real-life multi-sensor navigation systems are complex to troubleshoot. Typical accuracies for sensors used in this paper are listed in Table C.1.

Navigation from multi-sensor fusion has been tremendously successful since it combines complementary sensor properties in a single enhanced solution. However, this strength has a very serious associated weakness in that an error in any one sensor can lead to loss of integrity of the combined solution and even more importantly in practice, the root cause can often be extremely difficult to identify even for a navigation specialist. For example, an unidentified timing error in an aiding sensor may lead to the AAINS Kalman filter falsely estimating a large inertial sensor bias. In this case the root cause will not be intuitive to the average operator. In order to reduce these cross-sensor failure modes, the work herein strives to segregate aiding-sensors during parameter estimation, i.e. using only the IMU, the sensor data and other trusted sources (sensors) if applicable.

As the calibration problem is non-linear in nature, a two step approach is used: coarse parameters are estimated using a non-linear least-squares algorithm, which are then used to "warm-start" a state-augmented AAINS Kalman filter that refines the estimates. We use robust relative navigation with as few sensors as possible as input to the coarse estimation: IMU data, "zero updates" (e.g. "measuring" zero velocity) and sensor data itself (note that it is uncalibrated, and not to be completely trusted). From this relative navigation expected observations are derived and compared to the sensor data. The AAINS Kalman filter uses state augmentation to estimate the parameters. This is repeated for each sensor to be calibrated: pressure depth, DVL and LBL. The exact approach for each sensor is given Sections C.5, C.6 and C.7, respectively. The IMU is considered to be factory calibrated [C5], but run-time calibration

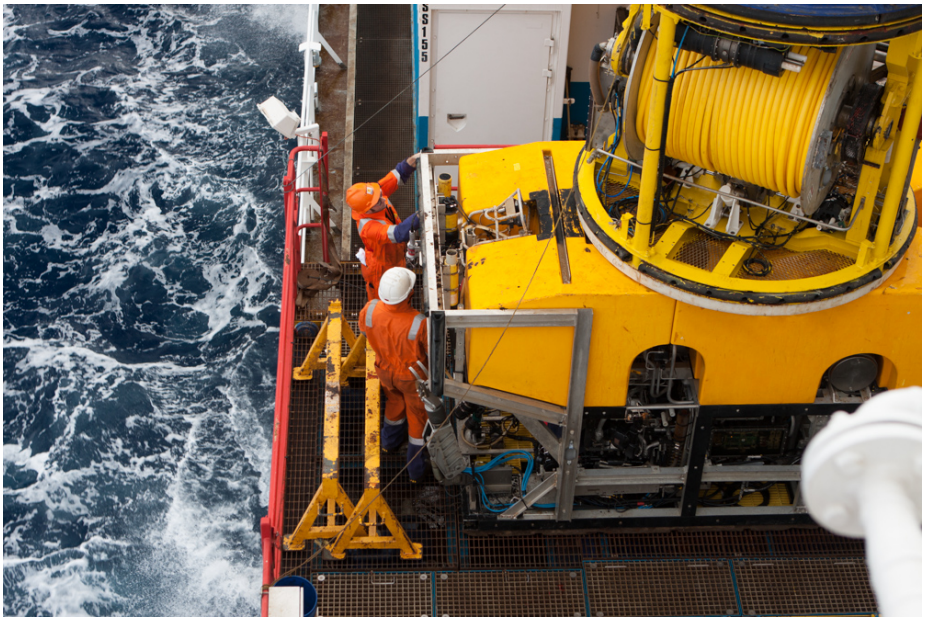

Figure C.1: Work-class ROV with the Tether Management System (TMS), i.e the umbilical cable spool, on-top. The yellow top-part of the vehicle is the buoyancy shell.

of inertial sensor biases, see Section C.3.1, is performed with every run of the AAINS.

For the parameters to be observable, a series of maneuvers must be undertaken. These are highly subject to the vehicle used; general purpose work-class ROVs, see Fig. C.1, are neutrally buoyant, have plenty of thrust and might be over-actuated. Neutral buoyancy is achieved mainly by a flotation top-cap—a buoyancy shell. This "top-light" construction makes it hard to pitch and roll, but easy to keep the ROV leveled. Interviewing a group of experienced ROV pilots and by experimental validation ± 10 deg roll/pitch is the highest the authors have seen in any data set and ROV pilots stated that this was the highest, with few unlikely exceptions, that they had seen to date; and is far beyond the normal operation envelope. This is not optimal for parameter estimation purposes, as the estimation accuracy will be somewhat limited.

Centimetric-level navigation performance is demonstrated using a consolidated AAINS, i.e. using all available aiding-sensors, with the parameters previously estimated.

Table C.1: Sensor and typical observation accuracies

Sensor	Observation	Accuracy (σ)	Unit
INS	roll and pitch	0.01	°
INS	heading	0.05[a]	°
DVL	seabed relative velocity	0.2	cm/s
LBL	range	1.5	cm
Depth	pressure depth	0.2[b]	m

[a] scales with $\sec(L)$.
[b] given as 0.01% of full scale; roughly 0.2 m for the sensor used in these trials.

C.3 Conventional strapdown AAINS mechanization

An INS is a dead-reckoning system that allows any vehicle to be positioned, in the short term, accurately without having to rely on models of vehicle dynamic. Motion is sensed by three accelerometers and three gyroscopes inside the INS, referred to as an inertial measurement unit (IMU). In a strapdown system the IMU follows the motion of the vehicle, i.e. unlike stable-platform mechanical gyroscopes. Throughout this paper the notation $(\cdot)^{\mathrm{i}}_{\mathrm{en}}$ means that the quantity of n-frame with respect to e-frame, expressed in i-frame—unless otherwise stated—with the relevant reference frames:

inertial	Earth centered inertial (ECI) frame, with the z-axis coincident with Earth's polar axis.
earth	Earth centered Earth fixed (ECEF) frame, same as ECI, both rotates at a rate Ω about the z-axis, with respect to the i-frame. X-axis goes through the intersection of the equatorial plane and the Greenwich meridian.
navigation	Local-level North–East–Down (NED) frame.
body	Frame with axes coinciding with the INS housing axes; x: forward, y: starboard and z: down.
sensor	Frame with axes coinciding with the aiding sensor's axes.

Linear acceleration and angular rate measured by the IMU is integrated to velocity $\boldsymbol{v}$, position $\boldsymbol{p}$ and orientation $\mathrm{C}_{\mathrm{b}}^{\mathrm{n}}$ according to e.g. [C3, C12]:

$$\dot{\boldsymbol{v}}_{\mathrm{eb}}^{\mathrm{n}} = \underbrace{\mathrm{C}_{\mathrm{b}}^{\mathrm{n}} \boldsymbol{f}_{\mathrm{ib}}^{\mathrm{b}}}_{\text{inertial}} - \underbrace{(2\boldsymbol{\omega}_{\mathrm{ie}}^{\mathrm{n}} + \boldsymbol{\omega}_{\mathrm{en}}^{\mathrm{n}}) \times \boldsymbol{v}_{\mathrm{eb}}^{\mathrm{n}}}_{\text{Coriolis}} + \underbrace{\boldsymbol{g}_{\mathrm{l}}^{\mathrm{n}}}_{\text{gravity}} \tag{C.1}$$

$$\dot{\boldsymbol{p}}_{\mathrm{e}}^{\mathrm{n}} = \begin{bmatrix} \frac{v_{\mathrm{N}}}{R_{\mathrm{N}} - d} & \frac{v_{\mathrm{E}} \sec L}{R_{\mathrm{E}} - d} & v_{\mathrm{D}} \end{bmatrix}^{\top} \tag{C.2}$$

$$\dot{\mathrm{C}}_{\mathrm{b}}^{\mathrm{n}} = \mathrm{C}_{\mathrm{b}}^{\mathrm{n}} \boldsymbol{\Omega}_{\mathrm{ib}}^{\mathrm{b}} - \boldsymbol{\Omega}_{\mathrm{in}}^{\mathrm{n}} \mathrm{C}_{\mathrm{b}}^{\mathrm{n}} \,, \tag{C.3}$$

following the notation of [C3, C12], with

v_{N}	velocity in North direction
v_{E}	velocity in East direction
v_{D}	velocity in down direction
$\boldsymbol{v}_{\mathrm{eb}}^{\mathrm{n}}$	navigation frame velocity vector: $\begin{bmatrix} v_{\mathrm{N}} & v_{\mathrm{E}} & v_{\mathrm{D}} \end{bmatrix}^{\top}$
$\boldsymbol{f}_{\mathrm{ib}}^{\mathrm{b}}$	specific force as measured by the accelerometers
$\boldsymbol{p}_{\mathrm{e}}^{\mathrm{n}}$	position vector $\begin{bmatrix} L & \ell & d \end{bmatrix}^{\top}$
L	latitude
ℓ	longitude
d	depth
$\mathrm{C}_{\mathrm{b}}^{\mathrm{n}}$	platform orientation, direction-cosine matrix (DCM) representation of the rotation sequence from body-frame to navigation-frame
$\boldsymbol{\omega}_{\mathrm{ie}}^{\mathrm{n}}$	turn rate of Earth with respect to inertial frame $\begin{bmatrix} \Omega \cos L & 0 & -\Omega \sin L \end{bmatrix}^{\top}$
$\boldsymbol{\omega}_{\mathrm{en}}^{\mathrm{n}}$	turn rate of the navigation frame with respect to the Earth frame, also called transport rate $\begin{bmatrix} \dot{\ell} \cos L & -\dot{L} & -\dot{\ell} \sin L \end{bmatrix}^{\top}$
$\boldsymbol{\Omega}_{\mathrm{ib}}^{\mathrm{b}}$	body rate measured by the gyroscopes
$\boldsymbol{\Omega}_{\mathrm{in}}^{\mathrm{n}}$	skew-symmetric form of the turn rate of the navigation frame with respect to inertial frame $\boldsymbol{\omega}_{\mathrm{in}}^{\mathrm{n}} = \boldsymbol{\omega}_{\mathrm{ie}}^{\mathrm{n}} + \boldsymbol{\omega}_{\mathrm{en}}^{\mathrm{n}}$
$\boldsymbol{g}_{\mathrm{l}}^{\mathrm{n}}$	local gravity vector. Often simplified to $[0 \; 0 \; g(L,d)]^{\top}$,

and $R_{\mathrm{N}} = \frac{R(1-e^2)}{(1-e^2 \sin^2 L)^{3/2}}$, $R_{\mathrm{E}} = \frac{R}{(1-e^2 \sin^2 L)^{1/2}}$ with semi-major axis length R and eccentricity of the ellipsoid e, both given by the geodetic model, e.g. WGS-84 [C2].

Inertial navigation inhibits poor long term accuracy and will eventually drift off due to sensor errors, modeling errors, initial errors, etc. In an AINS the complementary properties of inertial navigation and other navigation sensors are combined to obtain navigation with good accuracy and bounded error. The framework used to fuse the external aiding sensors with INS is shown in Fig. C.2. Since INS errors are evolving much slower than the navigational dynamics, it makes sense to make the computationally harder estimation task only track errors. This is the main idea behind the error-state Kalman filter (ESKF) [C1, C3, C12].

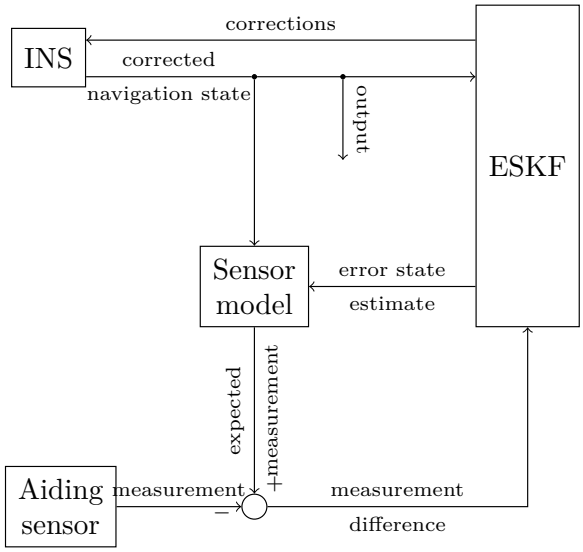

Figure C.2: General AINS framework. The corrections are either fed back to the INS, or alternatively applied to the INS output. If the former is true, the error state must be reset for each feedback. INS output is the *navigation state*: position, velocity, orientation, turn rate and acceleration.

The states in the ESKF are models of errors, instead of the full states e.g. *estimated depth error* compared to *estimated depth*. This set-up allows the ESKF to have a slower update rate than the INS, relaxing both hardware and algorithm requirements, while allowing aiding sensor latency to be handled. The estimated navigation state, as well as inertial observations, are defined as

$$\hat{\boldsymbol{v}}^{\mathrm{n}}_{\mathrm{eb}} = \boldsymbol{v}^{\mathrm{n}}_{\mathrm{eb}} + \boldsymbol{\delta v}^{\mathrm{n}}_{\mathrm{eb}} \tag{C.4}$$

$$\hat{\boldsymbol{p}}^{\mathrm{n}}_{\mathrm{eb}} = \boldsymbol{p}^{\mathrm{n}}_{\mathrm{eb}} + \boldsymbol{\delta p}^{\mathrm{n}}_{\mathrm{eb}} \tag{C.5}$$

$$\hat{\mathrm{C}}^{\mathrm{n}}_{\mathrm{b}} = (\boldsymbol{I} - \boldsymbol{\Psi})\,\mathrm{C}^{\mathrm{n}}_{\mathrm{b}} \tag{C.6}$$

$$\hat{\boldsymbol{f}}^{\mathrm{b}} = \boldsymbol{f}^{\mathrm{b}} + \boldsymbol{\delta f}^{\mathrm{b}} \tag{C.7}$$

$$\hat{\boldsymbol{\omega}}^{\mathrm{b}}_{\mathrm{ib}} = \boldsymbol{\omega}^{\mathrm{b}}_{\mathrm{ib}} + \boldsymbol{\delta\omega}^{\mathrm{b}}_{\mathrm{ib}}\ , \tag{C.8}$$

where

$\boldsymbol{\delta v}^{\mathrm{n}}_{\mathrm{e}}$ velocity error
$\boldsymbol{\delta p}^{\mathrm{n}}_{\mathrm{e}}$ position error
$\boldsymbol{\Psi}$ matrix form of the platform misalignment using a small angle approximation, $[\boldsymbol{\delta\psi}\times]$

$[\boldsymbol{\lambda}\times]$ skew-symmetric form of the vector $\boldsymbol{\lambda}$
$\boldsymbol{\delta\psi}$ platform misalignment vector $\begin{bmatrix}\delta\alpha & \delta\beta & \delta\gamma\end{bmatrix}^\top$
$\boldsymbol{\delta f}^{\mathrm{b}}$ accelerometer measurement error
$\boldsymbol{\delta\omega}^{\mathrm{b}}_{\mathrm{ib}}$ gyroscope measurement error.

Substituting (C.4)–(C.6) into (C.1)–(C.3) yields the navigation error equations, which describes how errors propagate and build up over time

$$\dot{\boldsymbol{\delta\psi}} = -\boldsymbol{\omega}^{\mathrm{n}}_{\mathrm{in}} \times \boldsymbol{\delta\psi} + \boldsymbol{\delta\omega}^{\mathrm{n}}_{\mathrm{in}} - \mathrm{C}^{\mathrm{n}}_{\mathrm{b}}\boldsymbol{\delta\omega}^{\mathrm{b}}_{\mathrm{ib}} \tag{C.9}$$

$$\begin{aligned}\dot{\boldsymbol{\delta v}}^{\mathrm{n}}_{\mathrm{e}} = {}& [\boldsymbol{f}^{\mathrm{n}}\times]\boldsymbol{\delta\psi} + \mathrm{C}^{\mathrm{n}}_{\mathrm{b}}\boldsymbol{\delta f}^{\mathrm{b}} - (2\boldsymbol{\omega}^{\mathrm{n}}_{\mathrm{ie}} + \boldsymbol{\omega}^{\mathrm{n}}_{\mathrm{en}}) \times \boldsymbol{\delta v}^{\mathrm{n}}_{\mathrm{e}} \\ & - (2\boldsymbol{\delta\omega}^{\mathrm{n}}_{\mathrm{ie}} + \boldsymbol{\delta\omega}^{\mathrm{n}}_{\mathrm{en}}) \times \boldsymbol{v}^{\mathrm{n}}_{\mathrm{e}} - \boldsymbol{\delta g}^{\mathrm{n}}_{\mathrm{l}}\end{aligned} \tag{C.10}$$

$$\dot{\boldsymbol{\delta p}}^{\mathrm{n}}_{\mathrm{e}} = \boldsymbol{\delta v}^{\mathrm{n}}_{\mathrm{e}} \ , \tag{C.11}$$

where $\boldsymbol{\delta\omega}^{\mathrm{n}}_{\mathrm{ie}}$ is the error in Earth's spin rate, which is negligible for navigation purposes, and $\boldsymbol{\delta g}^{\mathrm{n}}_{\mathrm{l}}$ the error in the local gravity. The estimated navigational state errors are used as corrections and are fed back to the INS.

The ESKF dynamic system model and measurement model are

$$\dot{\boldsymbol{\delta x}}(t) = \boldsymbol{f}(\boldsymbol{\delta x}, \boldsymbol{x}, \boldsymbol{u}, t) + \boldsymbol{g}(\boldsymbol{w}, t) \tag{C.12}$$

$$\boldsymbol{z}(t) = \boldsymbol{h}(\boldsymbol{\delta x}, \boldsymbol{x}, t) + \boldsymbol{v}(t) \ , \tag{C.13}$$

with state $\boldsymbol{x}$ (position, velocity, orientation), error-state $\boldsymbol{\delta x}$, stochastic forcing function $\boldsymbol{w}$ from the inertial sensors, deterministic forcing function $\boldsymbol{u}$ from inertial measurements and aiding sensor measurement $\boldsymbol{z}$ with noise $\boldsymbol{v}$. The non-linear functions $\boldsymbol{f}$ and $\boldsymbol{g}$ are given by (C.9)–(C.11); $\boldsymbol{h}$ depends on the aiding sensor(s). As in a regular extended Kalman filter (EKF) the state vector estimate is propagated by

$$\boldsymbol{\delta\hat{x}}_{k|k-1} = \boldsymbol{\delta\hat{x}}_{k-1|k-1} + \int_{t_{k-1}}^{t_k} \boldsymbol{f}(\boldsymbol{\delta\hat{x}}(t), \hat{\boldsymbol{x}}(t), \boldsymbol{u}(t), t)\,\mathrm{d}t \tag{C.14}$$

and measurement update

$$\boldsymbol{\delta\hat{x}}_{k|k} = \boldsymbol{\delta\hat{x}}_{k|k-1} + \boldsymbol{K}_k\left(\boldsymbol{z}_k - \boldsymbol{h}(\boldsymbol{\delta\hat{x}}_{k|k-1}, \hat{\boldsymbol{x}}_k, t_k)\right) \tag{C.15}$$

with Kalman gain

$$\boldsymbol{K}_k = \boldsymbol{P}_{k|k-1}\boldsymbol{H}_k^\top\left(\boldsymbol{H}_k\boldsymbol{P}_{k|k-1}\boldsymbol{H}_k^\top + \boldsymbol{R}_k\right)^{-1} \tag{C.16}$$

where $\boldsymbol{R}_k$ is the discrete-time measurement covariance and

$$\boldsymbol{H}_k = \left.\frac{\partial \boldsymbol{h}(\boldsymbol{\delta x}, \boldsymbol{x}, t)}{\partial \boldsymbol{\delta x}}\right|_{\boldsymbol{\delta x}=\boldsymbol{\delta\hat{x}}_{k|k-1}} . \tag{C.17}$$

The associated covariance update and projection are

$$\boldsymbol{P}_{k|k} = (\boldsymbol{I} - \boldsymbol{K}_k \boldsymbol{H}_k)\, \boldsymbol{P}_{k|k-1} \tag{C.18}$$

$$\boldsymbol{P}_{k|k-1} = \boldsymbol{A}_k \boldsymbol{P}_{k-1|k-1} \boldsymbol{A}_k + \boldsymbol{Q}_k, \tag{C.19}$$

with the discrete-time time-update covariance $\boldsymbol{Q}_k$ and

$$\boldsymbol{F}_{k-1} = \left. \frac{\partial \boldsymbol{f}(\boldsymbol{\delta x}, \boldsymbol{x}, \boldsymbol{u}, t)}{\partial \boldsymbol{\delta x}} \right|_{\boldsymbol{\delta x} = \boldsymbol{\delta \hat{x}}_{k|k-1}} \tag{C.20}$$

$$\boldsymbol{A}_{k-1} = \exp\big(\boldsymbol{F}_{k-1}(t_k - t_{k-1})\big), \tag{C.21}$$

where the matrix exponential approximation requires that the propagation interval is sufficiently small. It should be emphasized that the ESKF should be operating close to the linearization point to minimize non-linear effects.

The ESKF estimates are refined by Rauch-Tung-Striebel (RTS) fixed interval smoothing [C1, C3], consisting of the forward filter pass describe above followed by a backward pass. Navigation estimates at any time-point will make use of all past and future information. The backward pass is effectively running the KF backwards in time, with the a priori information coming from the forward pass. Using the measurements from $\boldsymbol{z}_1$ to $\boldsymbol{z}_n$ the optimal estimate $\boldsymbol{\delta \hat{x}}_{k|n}$ $(k < n)$ is given by

$$\boldsymbol{\delta \hat{x}}_{k|n} = \boldsymbol{\delta \hat{x}}_{k|k} + \boldsymbol{C}_k(\boldsymbol{\delta \hat{x}}_{k+1|n} - \boldsymbol{\delta \hat{x}}_{k+1|k}) \tag{C.22}$$

$$\boldsymbol{P}_{k|n} = \boldsymbol{P}_{k|k} + \boldsymbol{C}_k \left(\boldsymbol{P}_{k+1|n} - \boldsymbol{P}_{k+1|k}\right) \boldsymbol{C}_k^\top, \tag{C.23}$$

with

$$\boldsymbol{C}_k = \boldsymbol{P}_{k|k} \boldsymbol{A}_{k+1}^\top \boldsymbol{P}_{k+1|k}^{-1} \tag{C.24}$$

The navigational state-space model is augmented with sensor error models. These help to better capture the uncertainties and estimate both constant and time-varying parameters in the combined system; an accelerometer comes with an inherent bias error that is compensated for during factory calibration, but is also subject to a time-varying bias error. The ESKF is augmented accordingly by

$$\boldsymbol{\delta x}' = \begin{bmatrix} \boldsymbol{\delta x}_{\text{nav}} \\ \hline \boldsymbol{\delta x}_{\text{sens}} \end{bmatrix} \tag{C.25}$$

$$\boldsymbol{\delta \dot{x}}'(t) = \boldsymbol{f}'(\boldsymbol{\delta x}'(t)) + \boldsymbol{g}'(\boldsymbol{u}'(t)) \ , \tag{C.26}$$

where prime, $'$, denotes augmented quantities. Gauss-Markov processes are commonly used for error modeling in ESKFs as they only require a single state, are

easy to implement and versatile. A first order Gauss–Markov process, with time-constant τ and variance σ^2, is exponentially-correlated and can be described by the system

$$x(0) \sim \mathcal{N}_{\text{iid}}(0, \sigma^2) \tag{C.27}$$

$$\dot{x}(t) = -\frac{1}{\tau}x(t) + \sqrt{\frac{2\sigma^2}{\tau}}u(t) \ , \tag{C.28}$$

where $u(t)$ is unity white noise. This allows modeling the errors as anything from a random constant, $\tau = \infty$, to almost zero time auto-correlation for $\tau \to 0$ i.e., every sample independently and identically Gaussian-distributed (iid).

C.3.1 IMU error model

High-end IMUs are factory calibrated [C5], so only the IMU biases are generally estimated online. The inertial sensors are modeled with biases as first order Gauss–Markov processes, with magnitude and time constant dependent on the sensors. The estimated specific force is defined as:

$$\boldsymbol{\delta f}^{\text{b}} = \boldsymbol{\delta f}^{\text{b}}_{\text{bias}} \quad \text{and} \quad \boldsymbol{\delta f}^{\text{b}}_{\text{bias}} \sim \mathcal{N}_{\text{iid}}(0, \boldsymbol{I}\sigma^2_{\text{abias}}) \ . \tag{C.29}$$

The states in (C.25) are augmented with (C.28). The coupling into the navigation states are found by applying the sensor error model to the navigation error equations. From (C.10) and (C.29) the relevant state transition matrix part is derived:

$$\boldsymbol{F}\big(\boldsymbol{\delta f}^{\text{b}}\big) = \text{C}^{\text{n}}_{\text{b}} \tag{C.30}$$

Similarly, the gyroscope sensor error model only contains bias error:

$$\boldsymbol{\delta\omega}^{\text{b}}_{\text{ib}} = \boldsymbol{\delta\omega}^{\text{b}}_{\text{ib,bias}} \ , \quad \text{and} \quad \boldsymbol{\delta\omega}^{\text{b}}_{\text{ib,bias}} \sim \mathcal{N}_{\text{iid}}(0, \boldsymbol{I}\sigma^2_{\text{gbias}}) \ , \tag{C.31}$$

with the state transition matrix is derived from (C.9) and (C.31):

$$\boldsymbol{F}\big(\boldsymbol{\delta\omega}^{\text{b}}_{\text{ib}}\big) = -\text{C}^{\text{n}}_{\text{b}} \tag{C.32}$$

The similarity between (C.30) and (C.32) is expected since the sensor models are identical and both couple sensor errors directly into identical state dynamics i.e., accelerometer to velocity and gyroscope to orientation.

C.4 Zero velocity update

As mentioned in Section C.2 the relative navigation solution used during coarse estimation can rely on “zero” observations: if completely stationary, an obser-

vation of zero velocity relative to Earth, is a good approximation. This is also known as zero velocity update (ZUPT). The measured zero velocity is simply

$$\tilde{\boldsymbol{z}} = \tilde{\boldsymbol{v}}^{\mathrm{n}}_{\mathrm{en}} + \boldsymbol{\epsilon}_{\mathrm{zupt}} = \mathbf{0} + \boldsymbol{\epsilon}_{\mathrm{zupt}}, \tag{C.33}$$

with measurement noise $\boldsymbol{\epsilon}_{\mathrm{zupt}} \sim \mathcal{N}_{\mathrm{iid}}(0, \boldsymbol{I}\sigma^2_{\mathrm{zupt}})$ and the expected observation

$$\hat{\boldsymbol{z}} = \hat{\boldsymbol{v}}^{\mathrm{n}}_{\mathrm{en}} = \mathbf{0} + \boldsymbol{\delta v}^{\mathrm{n}}_{\mathrm{en}} \ . \tag{C.34}$$

The observable difference is

$$\begin{aligned} \boldsymbol{\delta z} &= \hat{\boldsymbol{z}} - \tilde{\boldsymbol{z}} \\ &= (\mathbf{0} + \boldsymbol{\delta v}^{\mathrm{n}}) - \mathbf{0} \\ &= \boldsymbol{\delta v}^{\mathrm{n}} \ , \end{aligned} \tag{C.35}$$

and the observation matrix,

$$\boldsymbol{H}(\boldsymbol{\delta v}^{\mathrm{n}}) = \frac{\partial \boldsymbol{\delta v}^{\mathrm{n}}}{\partial \boldsymbol{\delta x}} = \boldsymbol{I} \ . \tag{C.36}$$

As seen from (C.35) and (C.36) the ESKF estimate is directly the estimation error, with corresponding measurement noise.

C.5 Pressure depth sensor

Latency and lever arm are the two parameters that are relevant for pressure depth aiding. The lever arm from the INS to the pressure depth sensor is given by $\boldsymbol{r}_{\mathrm{bp}} = \begin{bmatrix} r_{\mathrm{bp},x} & r_{\mathrm{bp},y} & r_{\mathrm{bp},z} \end{bmatrix}^\top$. Empirical data suggests that the time-stamped[3] measurements are often time-lagged or low-pass filtered. This could simply be due to "long" sample intervals, ca. 1 s, which would resemble a constant time-lag. For certain highly dynamic trajectories and sensor configurations, time-lagged depth observations was found to be the root-cause of ill-estimated inertial sensor parameters.

Since the sensor only observes the vertical component in the navigation frame, the measurement model, $\tilde{z}_{\mathrm{pd}}(t)$, is given by

$$\tilde{z}_{\mathrm{pd}}(t) = \boldsymbol{q}\tilde{\boldsymbol{p}}^{\mathrm{n}}_{\mathrm{ep}}(t - \tau_{\mathrm{pd}}) + \epsilon_{\mathrm{pd}}(t) \tag{C.37}$$

$$\approx \boldsymbol{q}\left(\tilde{\boldsymbol{p}}^{\mathrm{n}}_{\mathrm{ep}}(t) - \tau_{\mathrm{pd}}\boldsymbol{v}^{\mathrm{n}}_{\mathrm{ep}}(t)\right) + \epsilon_{\mathrm{pd}}(t), \tag{C.38}$$

[3] pressure depth sensors commonly don't output timestamped data; this have to be done at the receiving side.

with time-lag τ_{pd}, $\boldsymbol{q} = \begin{bmatrix} 0 & 0 & 1 \end{bmatrix}$, measurement noise $\epsilon_{\text{pd}} \sim \mathcal{N}_{\text{iid}}(0, \sigma_{\text{pd}}^2)$ and

$$\tilde{\boldsymbol{p}}_{\text{ep}}^{\text{n}} = \boldsymbol{p}_{\text{eb}}^{\text{n}} + \boldsymbol{M}\mathrm{C}_{\text{b}}^{\text{n}}\boldsymbol{r}_{\text{bp}}^{\text{b}} + \begin{bmatrix} 0 & 0 & \boldsymbol{\delta d}_{\text{ep}}^{\text{n}} \end{bmatrix}^{\top}, \tag{C.39}$$

where $\boldsymbol{\delta d}_{\text{ep}}^{\text{n}}$ is a pressure depth bias or offset, e.g. when using the LBL array as vertical datum, and the conversion to curvilinear coordinates is

$$\boldsymbol{M} = \begin{bmatrix} \frac{1}{R_{\text{N}} - d} & 0 & 0 \\ 0 & \frac{\sec L}{R_{\text{E}} - d} & 0 \\ 0 & 0 & 1 \end{bmatrix}. \tag{C.40}$$

The expected observation $\hat{z}_{\text{pd}}$ is

$$\hat{z}_{\text{pd}}(t) = \boldsymbol{q}\hat{\boldsymbol{p}}_{\text{ep}}^{\text{n}}(t), \tag{C.41}$$

with

$$\hat{\boldsymbol{p}}_{\text{ep}}^{\text{n}} = \hat{\boldsymbol{p}}_{\text{eb}}^{\text{n}} + \boldsymbol{M}\hat{\mathrm{C}}_{\text{b}}^{\text{n}}\hat{\boldsymbol{r}}_{\text{bp}}^{\text{b}}, \tag{C.42}$$

with the lever arm error modeled as $\hat{\boldsymbol{r}}_{\text{bp}}^{\text{b}} = \boldsymbol{r}_{\text{bp}}^{\text{b}} + \boldsymbol{\delta r}_{\text{bp}}^{\text{b}}$. The observable difference, δz_{pd}, is formed:

$$\delta z_{\text{pd}}(t) = \hat{z}_{\text{pd}}(t) - \tilde{z}_{\text{pd}}(t), \tag{C.43}$$

which expands to:

$$\begin{aligned} \delta z_{\text{pd}} \approx \boldsymbol{q}\Big(&\boldsymbol{\delta p}_{\text{eb}}^{\text{n}} + \left[\boldsymbol{r}_{\text{pd}}^{\text{n}}\times\right]\boldsymbol{\delta\psi} + \boldsymbol{v}_{\text{ep}}^{\text{n}}\tau_{\text{pd}} \\ &\boldsymbol{M}\boldsymbol{\delta\psi} \times \mathrm{C}_{\text{b}}^{\text{n}}\boldsymbol{\delta r}_{\text{bp}}^{\text{b}} + \mathrm{C}_{\text{b}}^{\text{n}}\boldsymbol{\delta r}_{\text{bp}}^{\text{b}} - \begin{bmatrix} 0 & 0 & \boldsymbol{\delta d}_{\text{ep}}^{\text{n}} \end{bmatrix}^{\top}\Big), \end{aligned} \tag{C.44}$$

omitting t for brevity. The corresponding measurement update matrix is derived from (C.44) with respect to the state vector, augmented with latency and lever arm errors:

$$\boldsymbol{H}_{\text{pd}} = \left.\frac{\partial \delta z_{\text{pd}}}{\partial \boldsymbol{\delta x}_{\text{pd}}'}\right|_{\boldsymbol{\delta x}_{\text{pd}}' = \boldsymbol{0}}. \tag{C.45}$$

Ignoring states with zero contribution gives and products of errors:

$$\begin{aligned} &\boldsymbol{H}_{\text{pd}}\left(\boldsymbol{\delta p}; \boldsymbol{\delta\psi}; \boldsymbol{\delta r}_{\text{bp}}^{\text{b}}; \tau_{\text{pd}}; \boldsymbol{\delta d}_{\text{ep}}^{\text{n}}\right) \\ &\qquad \approx \boldsymbol{q}\begin{bmatrix} \boldsymbol{I} & \left[\boldsymbol{r}_{\text{bp}}^{\text{n}}\times\right] & \mathrm{C}_{\text{b}}^{\text{n}} & \boldsymbol{v}_{\text{ep}}^{\text{n}} & -\begin{bmatrix} 0 & 0 & 1 \end{bmatrix}^{\top} \end{bmatrix}. \end{aligned} \tag{C.46}$$

Note that the approximation starts to break down when the combination of angular acceleration, lever arm and latency becomes too large. This can to some extent be mitigated by appropriate KF tuning techniques.

A non-linear least-squares solver is used to coarsely estimate the parameters,

$$\hat{\boldsymbol{\theta}}_{\mathrm{pd}} = \underset{\boldsymbol{\theta}_{\mathrm{pd}} \in \Lambda_{\mathrm{pd}}}{\arg\min} \left(\hat{z}_{\mathrm{pd}}(t) - \tilde{z}_{\mathrm{pd}}(t)\right)^2, \tag{C.47}$$

$$\Lambda_{\mathrm{pd}} = \left\{ \boldsymbol{r}^{\mathrm{b}}_{\mathrm{bp}}, \tau_{\mathrm{pd}} \;\middle|\; -5 \leq \tau_{\mathrm{pd}} \leq 5 \right\}, \tag{C.48}$$

where the estimated value, $\hat{z}$, is formed from a relative navigation solution and $\tilde{z}$ is the observation.

The parameters' observability depends entirely on trajectory dynamics: latency is observable by having dynamics in the vertical channel of the navigation frame, e.g. rapid step-wise depth changes; the lever arm is observable during rotation.

The lever arm error effect on the pressure depth error in (C.44) can be expanded to

$$\begin{aligned} \boldsymbol{q}\mathrm{C}^{\mathrm{n}}_{\mathrm{b}}\boldsymbol{\delta r}^{\mathrm{b}}_{\mathrm{bp}} &= -\sin(p)\delta r_{\mathrm{bp},x} + \sin(r)\cos(p)\delta r_{\mathrm{bp},y} \\ &\quad + \cos(r)\cos(p)\delta r_{\mathrm{bp},z} \end{aligned} \tag{C.49}$$

$$\approx -p\delta r_{\mathrm{bp},x} + r\delta r_{\mathrm{bp},y} + \delta r_{\mathrm{bp},z}, \tag{C.50}$$

where INS roll and pitch is given by r and p. Due to the ROV roll and pitch limitations it is infeasible to estimate the vertical component of the lever arm. Assuming a 1 cm maximum acceptable pressure depth measurement error and maximum roll/pitch of 5 deg, the required horizontal lever arm accuracy, $\delta r_{\mathrm{bp},x}$ and $\delta r_{\mathrm{bp},y}$ becomes

$$\delta r_{\mathrm{bp},x} < \frac{\mathrm{roll}_{\max}}{\delta z_{\mathrm{pd},\max}} = \frac{5\pi/180}{0.01 \text{ m}} \approx 10 \text{ cm}, \tag{C.51}$$

see Fig. C.3. The lever arm can likely be estimated using IMU and ZUPTs or DVL aided INS: If a co-located and/or pre-calibrated DVL-INS is used, the relative navigation solution is straight forward; alternatively, if the vehicle can touch-down on the sea-bed, ZUPT aiding will suffice by letting the ROV come to a complete stop in-between dynamic maneuvers. The time between ZUPTs should be short enough for the INS to not drift too far. This period can be expanded with coarse position aiding, i.e. large measurement noise, to help keep the AAINS more stable. The relative navigation required for (C.47) was never realized as the limitations of the real-world dynamic trajectory (which did not touch-down on the seabed), meant that no lever arms were estimated and coarse estimation was not necessary for latency estimation using AAINS.

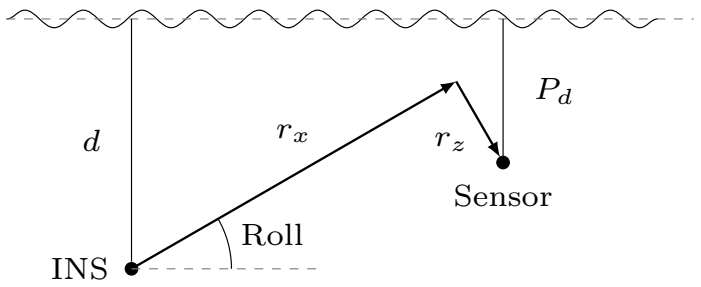

Figure C.3: Simplified side-view drawing of ROV with INS–pressure depth lever arm

C.6 Doppler velocity log

The DVL measures the sensor velocity relative to the sea floor in sensor frame, $\boldsymbol{v}^{\mathrm{d}}_{\mathrm{ed}}$. Latency, scale-factor, lever arm and orientation relative to the INS are the parameters sought to be calibrated. The measurement model is

$$\tilde{\boldsymbol{z}}_{\mathrm{dvl}} = (1+k)\boldsymbol{v}^{\mathrm{d}}_{\mathrm{ed}}(t-\tau_{\mathrm{dvl}}) + \boldsymbol{\epsilon}_{\mathrm{dvl}} \tag{C.52}$$

$$\approx (1+k)\left(\boldsymbol{v}^{\mathrm{d}}_{\mathrm{ed}}(t) - \tau_{\mathrm{dvl}}\boldsymbol{a}^{\mathrm{d}}_{\mathrm{ed}}(t)\right) + \boldsymbol{\epsilon}_{\mathrm{dvl}}\ , \tag{C.53}$$

with measurement noise $\boldsymbol{\epsilon}_{\mathrm{dvl}} \sim \mathcal{N}_{\mathrm{iid}}(0, \boldsymbol{I}\sigma^2_{\mathrm{dvl}})$, scale-factor k, and the velocity of the DVL with respect to sea-bed in DVL frame:

$$\boldsymbol{v}^{\mathrm{d}}_{\mathrm{ed}} = \mathrm{C}^{\mathrm{d}}_{\mathrm{b}}\left(\boldsymbol{v}^{\mathrm{b}}_{\mathrm{en}} + \boldsymbol{\omega}^{\mathrm{b}}_{\mathrm{eb}} \times \boldsymbol{r}^{\mathrm{b}}_{\mathrm{bd}}\right) \tag{C.54}$$

and the corresponding acceleration:

$$\boldsymbol{a}^{\mathrm{d}}_{\mathrm{ed}} = \mathrm{C}^{\mathrm{d}}_{\mathrm{b}}\left(\boldsymbol{a}^{\mathrm{b}}_{\mathrm{eb}} + \boldsymbol{\omega}^{\mathrm{b}}_{\mathrm{eb}} \times \left(\boldsymbol{\omega}^{\mathrm{b}}_{\mathrm{eb}} \times \boldsymbol{r}^{\mathrm{b}}_{\mathrm{bd}}\right) + \dot{\boldsymbol{\omega}}^{\mathrm{b}}_{\mathrm{eb}} \times \boldsymbol{r}^{\mathrm{b}}_{\mathrm{bd}}\right), \tag{C.55}$$

where $\boldsymbol{a}^{\mathrm{b}}_{\mathrm{eb}} = \mathrm{C}^{\mathrm{b}}_{\mathrm{n}}\dot{\boldsymbol{v}}^{\mathrm{n}}_{\mathrm{eb}}$, from (C.1). The angular acceleration $\dot{\boldsymbol{\omega}}^{\mathrm{b}}_{\mathrm{eb}}$ can be expressed as:

$$\dot{\boldsymbol{\omega}}^{\mathrm{b}}_{\mathrm{eb}} = \dot{\boldsymbol{\omega}}^{\mathrm{b}}_{\mathrm{ib}} + \left[\boldsymbol{\omega}^{\mathrm{b}}_{\mathrm{eb}}\times\right]\mathrm{C}^{\mathrm{b}}_{\mathrm{n}}\boldsymbol{\omega}^{\mathrm{n}}_{\mathrm{ie}}, \tag{C.56}$$

with

$$\boldsymbol{\omega}^{\mathrm{n}}_{\mathrm{ie}} = w_{\mathrm{ie}}\begin{bmatrix}\cos L\\ 0\\ -\sin L\end{bmatrix}. \tag{C.57}$$

The expected-measurement model is:

$$\hat{\boldsymbol{z}}_{\mathrm{dvl}} = \hat{\boldsymbol{v}}^{\mathrm{d}}_{\mathrm{ed}}(t) = \hat{\mathrm{C}}^{\mathrm{d}}_{\mathrm{b}}\left(\left[\hat{\mathrm{C}}^{\mathrm{n}}_{\mathrm{b}}\right]^{\top}\hat{\boldsymbol{v}}^{\mathrm{n}}_{\mathrm{en}} + \boldsymbol{\omega}^{\mathrm{b}}_{\mathrm{eb}} \times \hat{\boldsymbol{r}}^{\mathrm{b}}_{\mathrm{bd}}\right), \tag{C.58}$$

with the lever arm is modeled as $\hat{\boldsymbol{r}}^{\mathrm{b}}_{\mathrm{dvl}} = \boldsymbol{r}^{\mathrm{b}}_{\mathrm{dvl}} + \boldsymbol{\delta r}^{\mathrm{b}}_{\mathrm{dvl}}$ and the DVL Euler misalignment angles $\boldsymbol{\delta\psi}_{\mathrm{d}} = \begin{bmatrix}\alpha_{\mathrm{d}} & \beta_{\mathrm{d}} & \gamma_{\mathrm{d}}\end{bmatrix}^{\top}$ by $\hat{\mathrm{C}}^{\mathrm{d}}_{\mathrm{b}} = (\boldsymbol{I} - \boldsymbol{\Psi}_{\mathrm{d}})\,\mathrm{C}^{\mathrm{d}}_{\mathrm{b}}$, where $\boldsymbol{\Psi}_{\mathrm{d}} = [\boldsymbol{\psi}_{\mathrm{d}}\times]$, $\hat{\boldsymbol{v}}^{\mathrm{n}}_{\mathrm{en}}$ and $\hat{\mathrm{C}}^{\mathrm{n}}_{\mathrm{b}}$ from (C.4) and (C.6), respectively. The observable difference is formed

$$\boldsymbol{\delta z}_{\mathrm{dvl}} = \hat{\boldsymbol{z}}_{\mathrm{dvl}} - \tilde{\boldsymbol{z}}_{\mathrm{dvl}}\ , \tag{C.59}$$

from which the DVL measurement update matrix is derived according to

$$\boldsymbol{H}_{\mathrm{dvl}} = \left.\frac{\partial \boldsymbol{\delta z}_{\mathrm{dvl}}}{\partial \boldsymbol{\delta x}'_{\mathrm{dvl}}}\right|_{\boldsymbol{\delta x}'_{\mathrm{dvl}}=\boldsymbol{0}}\ , \tag{C.60}$$

yielding

$$\begin{aligned}\boldsymbol{H}_{\mathrm{dvl}}\left(\boldsymbol{\delta\psi}; \boldsymbol{\delta v}^{\mathrm{n}}_{\mathrm{en}}; \boldsymbol{\delta r}^{\mathrm{b}}_{\mathrm{bd}}; k; \boldsymbol{\delta\psi}_{\mathrm{d}}; \tau_{\mathrm{dvl}}\right) = \\ \begin{bmatrix}-\mathrm{C}^{\mathrm{d}}_{\mathrm{n}}[\boldsymbol{v}^{\mathrm{n}}_{\mathrm{eb}}\times] & \mathrm{C}^{\mathrm{d}}_{\mathrm{n}} & \mathrm{C}^{\mathrm{d}}_{\mathrm{b}}[\boldsymbol{\omega}^{\mathrm{b}}_{\mathrm{eb}}\times] & -\boldsymbol{v}^{\mathrm{d}}_{\mathrm{ed}} & \begin{bmatrix}\boldsymbol{v}^{\mathrm{d}}_{\mathrm{ed}}\times\end{bmatrix} & \boldsymbol{a}^{\mathrm{d}}_{\mathrm{ed}}\end{bmatrix}.\end{aligned} \tag{C.61}$$

A non-linear least-squares solver is used to coarsely estimate the parameters,

$$\hat{\boldsymbol{\theta}}_{\mathrm{dvl}} = \underset{\boldsymbol{\theta}_{\mathrm{dvl}} \in \Lambda_{\mathrm{dvl}}}{\arg\min}\ \left(\hat{z}_{\mathrm{dvl}} - \tilde{z}_{\mathrm{dvl}}\right)^2, \tag{C.62}$$

$$\Lambda_{\mathrm{dvl}} = \left\{\ \boldsymbol{r}^{\mathrm{b}}_{\mathrm{dvl}}, \boldsymbol{\psi}_{\mathrm{d}}, k, \tau_{\mathrm{dvl}}\ \middle|\ -0.02 \leq k \leq 0.02, -5 \leq \tau_{\mathrm{dvl}} \leq 5\ \right\}, \tag{C.63}$$

where the estimated value, $\hat{z}$, is formed from a relative navigation solution and $\tilde{z}$ is the observation. The relative navigation emerges from a ZUPT aided AINS. We apply a simple trick to detect zero-velocity: ZUPT is activated only when the measured (uncalibrated) DVL speed is below a certain threshold, and the measurement noise matrix $\boldsymbol{R}_{\mathrm{zupt}}$ is formed from the measured DVL speed

$$\boldsymbol{R}_{\mathrm{zupt}} = \boldsymbol{I}\left(|\tilde{\boldsymbol{v}}^{\mathrm{d}}_{\mathrm{en}}|\sqrt{3}\right)^2\ , \tag{C.64}$$

where $\sqrt{3}$ was chosen to keep the resulting speed variance close to the measured speed.

Identical to the pressure depth sensor, the DVL lever arm $\boldsymbol{r}^{\mathrm{b}}_{\mathrm{dvl}}$ is made observable by rotation. Dually, the DVL orientation $\boldsymbol{\psi}_{\mathrm{d}}$ is made observable by translation. Note that both orientation and translation should be sufficiently exited, in multiple dimensions, for all parameters to be observable. Velocity changes makes the scale factor k and latency τ_{dvl} observable.

C.7 Long baseline

An LBL system measures the two-way travel-time between the transceiver and one or more transponders. Owing to the speed of sound in seawater c, which is

roughly between 1400–1600 m/s, and of distances of up to 3000 m, the travel-time is typically measured in seconds. Included implicitly in the two-way travel-time is a transponder turn-around-time T_{tat}, that is practically used to ensure that all responses do not arrive at the exact same time. This is on the scale of hundreds of milliseconds.

Given the transmission time t_{t} and reception time t_{r}, the measurement can be modeled:

$$\tilde{z}_{\text{lbl}} = t_{\text{twt}}(t_{\text{t}}, t_{\text{r}}) + \epsilon_{\text{lbl}} \tag{C.65}$$

$$\approx \frac{\|\boldsymbol{R}(t_{\text{t}})\| + \|\boldsymbol{R}(t_{\text{r}})\|}{c} + T_{\text{tat}} + \epsilon_{\text{lbl}} \tag{C.66}$$

$$\approx \frac{2}{c}\|\boldsymbol{M}^{-1}\left(\boldsymbol{p}^{\text{n}} - \boldsymbol{p}^{\text{n}}_{\text{tpdr}}\right) + \mathrm{C}^{\text{n}}_{\text{b}}\boldsymbol{r}^{\text{b}}_{\text{lbl}}\| + T_{\text{tat}} + \epsilon_{\text{lbl}} \ , \tag{C.67}$$

with measurement noise $\epsilon_{\text{lbl}} \sim \mathcal{N}_{\text{iid}}(0, \sigma^2_{\text{lbl}})$, $\boldsymbol{R}$ being the range vector from LBL transceiver to transponder, each transponder position is given in navigation frame: $\boldsymbol{p}^{\text{n}}_{\text{tpdr}} = \begin{bmatrix} L_{\text{tpdr}} & \ell_{\text{tpdr}} & d_{\text{tpdr}} \end{bmatrix}^\top$, $\boldsymbol{r}^{\text{b}}_{\text{lbl}}$ is the lever arm from INS to LBL. The transformation matrix from curvilinear to Cartesian frame is given by

$$\boldsymbol{M}^{-1} = \begin{bmatrix} R_{\text{N}} - d & 0 & 0 \\ 0 & \frac{R_{\text{E}} - d}{\sec L} & 0 \\ 0 & 0 & 1 \end{bmatrix} . \tag{C.68}$$

The $t_{\text{t}} \approx t_{\text{r}}$ assumption in (C.67) is only used to derive the measurement update matrix in (C.75); elsewhere the form in (C.66) is used to properly correct for vehicle movement.

The lever arm is estimated with $\hat{\boldsymbol{r}}^{\text{b}}_{\text{lbl}} = \boldsymbol{r}^{\text{b}}_{\text{lbl}} + \boldsymbol{\delta r}^{\text{b}}_{\text{lbl}}$; transponder positions and speed of sound likewise: $\hat{\boldsymbol{p}}^{\text{n}}_{\text{tpdr}} = \boldsymbol{p}^{\text{n}}_{\text{tpdr}} + \boldsymbol{\delta p}^{\text{n}}_{\text{tpdr}}$ and $\hat{c} = c + \delta c$, respectively. The expected observation is

$$\hat{z}_{\text{lbl}} = \hat{t}_{\text{twt}}(t_{\text{t}}, t_{\text{r}}) \tag{C.69}$$

$$\approx \frac{\|\hat{\boldsymbol{R}}(t_{\text{t}})\| + \|\hat{\boldsymbol{R}}(t_{\text{r}})\|}{\hat{c}} + T_{\text{tat}} \tag{C.70}$$

$$\approx \frac{2}{\hat{c}}\|\boldsymbol{M}^{-1}\left(\hat{\boldsymbol{p}}^{\text{n}} - \hat{\boldsymbol{p}}^{\text{n}}_{\text{tpdr}}\right) + \hat{\mathrm{C}}^{\text{n}}_{\text{b}}\hat{\boldsymbol{r}}^{\text{b}}_{\text{lbl}}\| + T_{\text{tat}} \tag{C.71}$$

$$\begin{aligned} \approx \frac{2}{c + \delta c}\|&\boldsymbol{M}^{-1}\left(\boldsymbol{p}^{\text{n}} - \boldsymbol{p}^{\text{n}}_{\text{tpdr}}\right) + \boldsymbol{M}^{-1}\left(\boldsymbol{\delta p}^{\text{n}} - \boldsymbol{\delta p}^{\text{n}}_{\text{tpdr}}\right) \\ &+ \mathrm{C}^{\text{n}}_{\text{b}}\boldsymbol{r}^{\text{b}}_{\text{lbl}} + \mathrm{C}^{\text{n}}_{\text{b}}\boldsymbol{\delta r}^{\text{b}}_{\text{lbl}} - \boldsymbol{\Psi}\mathrm{C}^{\text{n}}_{\text{b}}\boldsymbol{r}^{\text{b}}_{\text{lbl}} + \boldsymbol{\Psi}\mathrm{C}^{\text{n}}_{\text{b}}\boldsymbol{\delta r}^{\text{b}}_{\text{lbl}}\| + T_{\text{tat}} \ . \end{aligned} \tag{C.72}$$

The observable difference,

$$\delta z_{\text{lbl}} = \hat{z}_{\text{lbl}} - \tilde{z}_{\text{lbl}} \ , \tag{C.73}$$

can written as:

$$\delta z_{\text{lbl}} \approx \frac{2}{c+\delta c}\|\boldsymbol{R} + \boldsymbol{M}^{-1}\left(\boldsymbol{\delta p}^{\text{n}} - \boldsymbol{\delta p}^{\text{n}}_{\text{tpdr}}\right) + \mathrm{C}^{\text{n}}_{\text{b}}\boldsymbol{\delta r}^{\text{b}}_{\text{lbl}} - \boldsymbol{\Psi}\mathrm{C}^{\text{n}}_{\text{b}}\boldsymbol{r}^{\text{b}}_{\text{lbl}}\| \quad \text{(C.74)}$$

with $\boldsymbol{R} = \boldsymbol{M}^{-1}\left(\boldsymbol{p}^{\text{n}} - \boldsymbol{p}^{\text{n}}_{\text{tpdr}}\right) + \mathrm{C}^{\text{n}}_{\text{b}}\boldsymbol{r}^{\text{b}}_{\text{lbl}}$ and by ignoring products of errors. The LBL measurement update matrix is derived from (C.74):

$$\boldsymbol{H}(\boldsymbol{\delta p}; \boldsymbol{\psi}; \boldsymbol{\delta p}^{\text{n}}_{\text{tpdr}}; \boldsymbol{\delta r}^{\text{b}}_{\text{lbl}}, \delta c) = \frac{2}{c}\frac{\boldsymbol{R}}{\|\boldsymbol{R}\|}\begin{bmatrix}\boldsymbol{M}^{-1} & [\boldsymbol{r}^{\text{n}}_{\text{lbl}}\times]^{\top} & -\boldsymbol{M}^{-1} & \mathrm{C}^{\text{n}\top}_{\text{b}} & -\frac{1}{c}\frac{\|\boldsymbol{R}\|^2}{\boldsymbol{R}}\end{bmatrix}. \quad \text{(C.75)}$$

Using acoustic transponders with uncertain, but fixed, position is a SLAM problem [C7], as known from robotics. For relative navigation, one transponder is picked as reference, fixing that position, while estimating other transponders' positions. The result is a calibrated array, relative to the reference transponder. Since the vertical position is tied to the pressure depth sensor, all transponders vertical position is estimated making the pressure depth sensor the reference.

A non-linear least-squares solver is used to coarsely estimate the parameters,

$$\hat{\boldsymbol{\theta}}_{\text{lbl}} = \underset{\boldsymbol{\theta}_{\text{lbl}} \in \Lambda_{\text{lbl}}}{\arg\min}\left(\hat{z}_{\text{lbl}} - \tilde{z}_{\text{lbl}}\right)^2, \quad \text{(C.76)}$$

$$\Lambda_{\text{lbl}} = \left\{\, \boldsymbol{r}^{\text{b}}_{\text{lbl}}, {}_2\boldsymbol{p}^{\text{n}}_{\text{tpdr}}, \cdots, {}_m\boldsymbol{p}^{\text{n}}_{\text{tpdr}} \,\right\}, \quad \text{(C.77)}$$

where ${}_i\boldsymbol{p}^{\text{n}}_{\text{tpdr}}$ indicates the i-th transponder. Since we are interested in relative navigation, one of the transponders horizontal position is fixed. The vertical component is not, since the pressure depth sensor acts as datum for the vertical position. Note that neither the sound velocity or sound velocity error is estimated in the coarse estimation. The speed of sound is calculated, per observation, from the LBL system as speed-over-range and is generally considered to be good, and is therefore only included in the AAINS when seeking to improve accuracy or robustness.

For the LBL parameters to be observable both the trajectory and the geometry[C6] of the transponders and transceiver over time, must be considered.

The DVL-INS navigation solution is used as relative navigation for coarse parameter estimation if it can be trusted i.e., mechanically integrated or co-located and pre-calibrated. Contrarily, without the DVL, generating the relative navigation is not straight forward. As with the pressure depth sensor, ZUPTs can be used if the vehicle can touch-down on the sea-bed, but even more so with LBL: the dynamics needed to enable coarse estimation might take too long–resulting

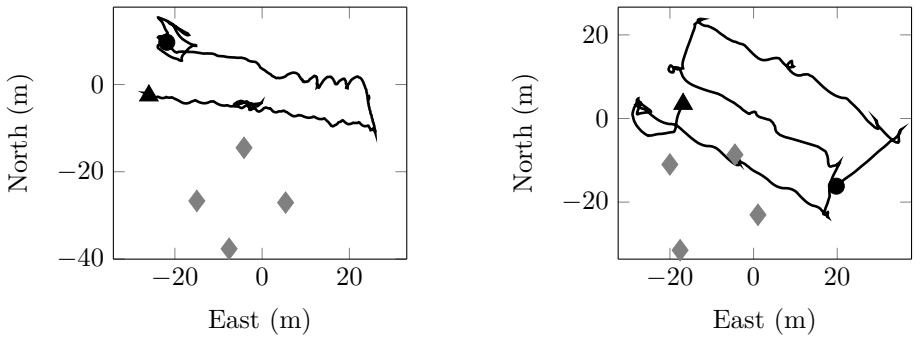

(a) Trial I survey

(b) Trial II survey trajectory.

Figure C.4: Trial survey trajectories. Begins at the circle and ends at the triangle. Transponder positions are marked with diamonds.

in large INS drift. The authors advice is to use a trusted DVL if coarse parameter estimation is necessary; otherwise, carefully measuring the lever arm and doing a relative array calibration will work.

C.8 Results

Sea trials were carried out in early 2013 for two offshore subsea construction surveys, using a work-class ROV. The ROV was equipped with a Sonardyne SPRINT system [C11]: a strap-down INS aided with pressure depth, 3D velocity from an RDI DVL and ranges from a Fusion LBL system and a Ranger 2 ultra-short baseline (USBL) position system, used to initialize the AAINS position; with accuracies similar to those given in Table C.1. Note that these trials concurrently tested the acoustic system and operational practices, and thus introduced gaps in the acoustic range data. The ROV piloted survey trajectories for the trials are shown in Fig. C.4. Occasionally the ROV pilots would unwind the umbilical tether by quickly counter-rotating the ROV, which is visible in both trajectories.

At the end of both surveys the ROV pilots were asked to excite the system as much as possible by completing a set of tasks, including:

- High-dynamic rotary motion
- High-dynamic linear translation
- A full 360 deg heading rotation step-wise, in 90 deg steps, with a pause

between steps
- Step-wise altitude change, with pauses
- Step-wise altitude change, completing a full 360 deg heading rotation step-wise, in 90 deg step, with pauses.

In-between tasks the ROV moves back at reference depth and orientation. Fig. C.5 show the resulting high-dynamic trajectories.

The parameter estimation method is verified in Section C.8.1 with simulation using realistic dynamics from the sea-trials, before the calibration is applied to real data in Section C.8.2.

C.8.1 Method verification using simulation

Realistic dynamics from the trials is used in a Monte Carlo simulation (sample size of 50) to verify the parameter estimation method presented in this paper. Each sample represents a sensor configuration. For each configuration, each aiding sensor was individually calibrated according to the previously described methods. The high-dynamics part of the trajectory was used for parameter estimation (Fig. C.5b), while the survey part was used to assess the navigation error (Fig. C.4b) after all aiding sensor were calibrated. Noisy aiding sensor data was synthesized with Gaussian distributed values according to Table C.1 and uniformly distributed errors: $\tau_{\text{dvl}} \in [0, 0.3]\,\text{s}$, $\text{Var}\left(\boldsymbol{\delta r}^{\text{b}}_{\text{bd}}\right) = \boldsymbol{I}(2\,\text{m})^2$, $\delta\alpha_{\text{d}} \in [0, 2\pi[$, $\delta\beta_{\text{d}} \in [-\frac{\pi}{2}, \frac{\pi}{2}]$, $\delta\gamma_{\text{d}} \in [0, 2\pi[$, $\tau_{\text{pdepth}} \in [0, 3]\,\text{s}$, $\text{Var}\left(\boldsymbol{\delta r}^{\text{b}}_{\text{bl}}\right) = \boldsymbol{I}(2\,\text{m})^2$.

Table C.2 summarizes the sensor calibration errors over the 50 simulation runs. Four transponders were used during the LBL calibration to be comparable with trial results. The radial horizontal navigation error is graphed in Fig. C.6 along with expected 1-DRMS from the ESKF, for navigation using four or two transponders.

C.8.2 Applying calibration to sea trials data

Each aiding sensor was individually calibrated using the previously described methods, for both sea trial data sets. The same system parameters and initial covariance was used for both data sets in the aiding sensor calibration. The initial transponder horizontal and vertical position uncertainty was set to 0.3 cm to SLAM the transponders and to account for the fact that the vertical datum was the AAINS.

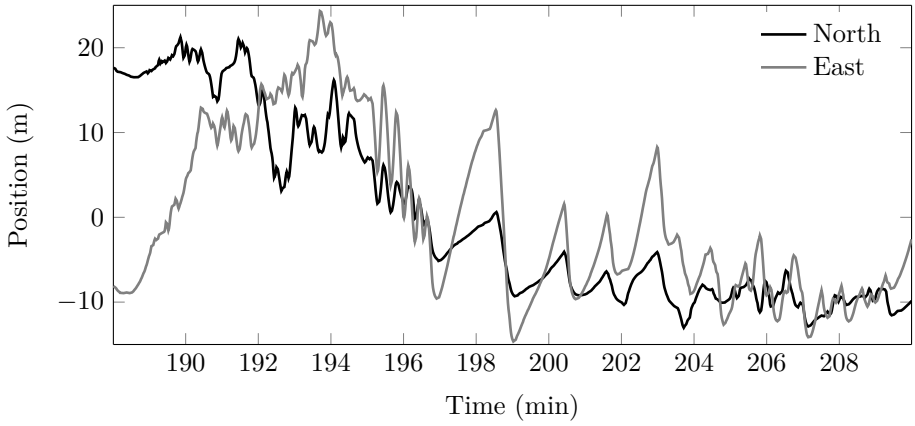

(a) Trial I high-dynamics

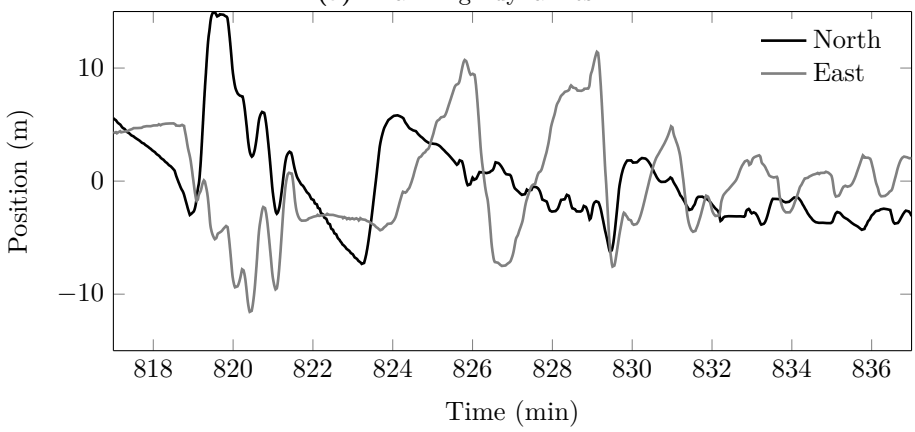

(b) Trial II high-dynamics

Figure C.5: Trial high-dynamics trajectories plotted as time-series.

Table C.2: Parameter estimation root-mean-square error (RMSE) from 50 simulation runs. The parameter accuracy σ_{RMS} is taken as root-mean-square across all runs.

Parameter	RMSE	σ_{RMS}	Unit
τ_{pd}	0.32	0.09	s
τ_{dvl}	0.17	0.01	s
$r^{\mathrm{b}}_{\mathrm{dvl,x}}$	2.11	1.68	cm
$r^{\mathrm{b}}_{\mathrm{dvl,y}}$	3.66	1.53	cm
$r^{\mathrm{b}}_{\mathrm{dvl,z}}$	11.11	1.79	cm
k	0.81	0.32	%
α_{dvl}	0.42	0.25	°
β_{dvl}	0.18	0.24	°
γ_{dvl}	0.39	0.30	°
$r^{\mathrm{b}}_{\mathrm{lbl,x}}$	0.22	0.22	cm
$r^{\mathrm{b}}_{\mathrm{lbl,y}}$	0.19	0.19	cm
$r^{\mathrm{b}}_{\mathrm{lbl,z}}$	1.28	0.91	cm

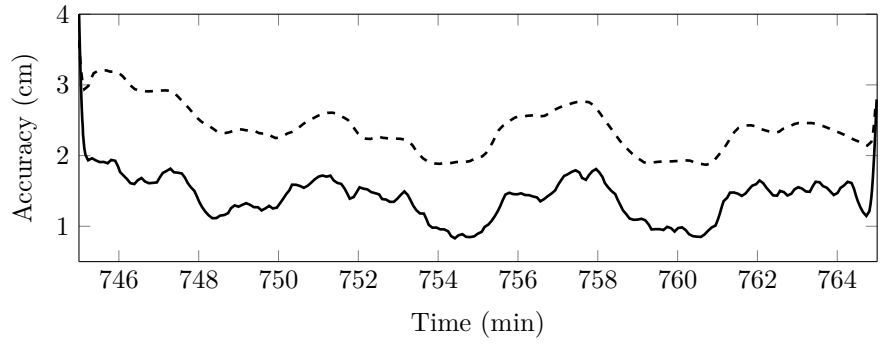

(a) Four transponders used for aiding

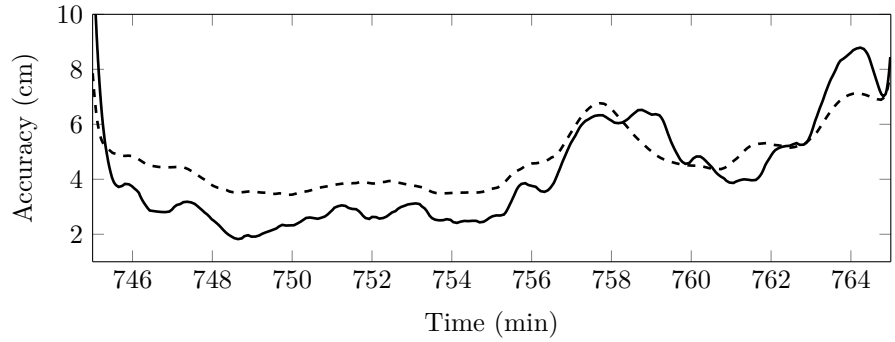

(b) Two transponders used for aiding

Figure C.6: Radial navigation error over 50 simulation runs. Solid lines are the RMS of the relative radial error and the dashed lines the RMS of the expected 1-DRMS.

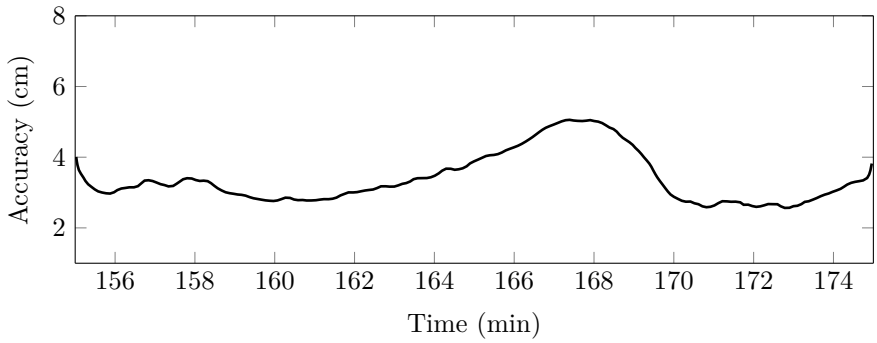

(a) Trial I.

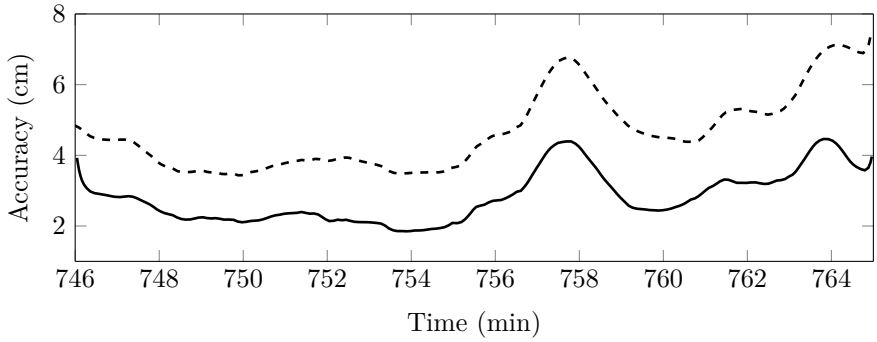

(b) Trial II. The dashed line is the RMS of the expected 1-DRMS for the 50 simulation runs from Fig. C.6.

Figure C.7: Navigation expected 1-DRMS accuracy for trials data.

Table C.3 lists the difference between the parameter estimation and measured parameters. Unfortunately, due to variable sound velocity, LBL array depth discrepancies and acoustic system testing, establishing reliable reference trajectories was not possible. But as our simulation framework is well tested, and is verified for these real-life dynamics (Fig. C.6b), the expected 1-DRMS is regarded as more than just a qualified guess, but likely to reflect real-world accuracy. The 1-DRMS for Trial I and II are shown in Fig. C.7; note that Trial II is compared to the Monte Carlo simulation in Fig. C.7b.

Table C.3: Trial I and II, difference $\Delta\theta = \hat{\theta} - \tilde{\theta}$, between the estimated and measured parameters. Estimation std.dev. σ is taken from the AAINS.

	Trial I		Trial II		
Parameter	$\lvert\Delta\theta\rvert$	σ	$\lvert\Delta\theta\rvert$	σ	Unit
${\tau_{\text{pd}}}^{*}$	0.22	0.08	0.23	0.09	s
${\tau_{\text{dvl}}}^{*}$	2.31	0.93	0.25	0.89	ms
${r^{\text{b}}_{\text{dvl,x}}}^{\dagger}$	0.22	0.44	0.27	0.46	cm
${r^{\text{b}}_{\text{dvl,y}}}^{\dagger}$	0.58	0.43	0.23	0.45	cm
${r^{\text{b}}_{\text{dvl,z}}}^{\dagger}$	10.45	1.35	10.69	0.99	cm
k^{*}	0.09	0.12	0.10	0.15	%
${\alpha_{\text{dvl}}}^{\dagger}$	0.10	0.09	0.02	0.11	$^{\circ}$
${\beta_{\text{dvl}}}^{\dagger}$	0.02	0.09	0.01	0.11	$^{\circ}$
${\gamma_{\text{dvl}}}^{\dagger}$	0.07	0.07	0.01	0.09	$^{\circ}$
${r^{\text{b}}_{\text{lbl,x}}}^{\ddagger}$	4.55	0.30	3.31	0.35	cm
${r^{\text{b}}_{\text{lbl,y}}}^{\ddagger}$	3.33	0.27	2.45	0.29	cm
${r^{\text{b}}_{\text{lbl,z}}}^{\ddagger}$	3.36	0.99	4.55	1.70	cm

* measured quantity assumed zero.
† measured quantity from schematic.
‡ measured with hand held laser ranger.

C.9 Conclusion

This paper investigates automated indirect parameter estimation as a means to: improve accuracy, reduce risk of blunders and enhance usability and save ship time. Automated AAINS sensor configuration parameter estimation is investigated using a mixture of non-linear optimization and classic Kalman filter state augmentation. Positive findings are supported by high-fidelity simulation and important experimental validation using data from sea trials performed under representative offshore operational conditions. Limited accuracy and reliability in current systems is in part managed by overly conservative tuning of the core AAINS sensor fusion algorithms (Kalman filter). Reliable parameter estimation will hence also indirectly improve navigation accuracy by allowing sharper tuning without risk of loosing filter integrity. Cross-sensor failure-modes are reduced by striving to allow only the IMU and individual sensor data for calibration. A highly dynamic trajectory is needed for the parameters to be observable. While this is beyond typical ROV operations, it is operational feasible to execute.

Table C.4 sums up conclusions of which parameters that can be estimated with different combinations of input data to the calibration routines. A significant finding of this paper is that in practice work-class ROVs have limited roll/pitch maneuverability, which directly inhibits estimation of the vertical lever arm component for both the DVL and pressure depth sensor. A significant difference between the estimated and measured vertical DVL lever arm is present in both sea trials results. Since the DVL was mechanically co-located with the INS and the measurement came from an assembly schematic, this difference is regarded as an estimation error. The large estimation error also noticeable in the Monte Carlo simulation results has not been investigated in depth due to complexity of the whole system, but is was observed that the not all cases were estimated wrongly, but this is hidden in the squared nature of the RMSE metric. The difference in LBL lever arms is on the order of 3–5 cm; which is within the authors' expected measuring accuracy on this ROV set-up.

Unsurprisingly, using 4 transponders results in impeccable centimetric-level relative navigation accuracy. This demonstrates the feasibility of using the automatic aiding sensor calibration with a full LBL array, achieving accuracy that would otherwise require expert-level manually tuning. It also shows that in this case the AAINS is slightly conservative. The integrity, for this trajectory, is like-wise verified using a sparse 2-transponder array. The simulation demonstrates centimetric-level relative navigation, using 2 transponders, although the trajectory is not optimal for sparse LBL navigation. Without a reliable reference, the sea trial navigation error could not be robustly assessed. An indication of performance is given by the AAINS covariance, which has been verified using Monte Carlo simulation. The expected 1-DRMS for both trials hints that

Table C.4: Reliable observability of aiding sensor parameters for different combinations of data input, i.e. IMU only, or DVL + IMU. ✓means that the parameter can be estimated, (✓) is borderline observable, - indicates that we did not test and x means that the parameter is incorrectly estimated or that the ESKF became overconfident in the estimate.

	Pressure depth			DVL					LBL
	r_{xy}	r_z	τ_{pd}	r_{xy}	r_z	τ_{dvl}	ψ_{d}	k	r_{xyz}
IMU	x	x	✓	✓	x	x	✓	(✓)	*
IMU + DVL	-	-	-	not applicable					✓

* Could not test, see conclusion.

centimetric-level relative navigation is practically feasible.

The authors believe that this application would benefit from employing a second-order non-linear Kalman filter such as the Unscented Kalman filter (UKF) [C13] or the Divided-Difference (DD2) filter[C8] in future work. Furthermore, auto-calibrating ultra-short baseline (USBL) responder/transceiver horizontal lever arms should be possible, and would be worth investigating. Likewise, concurrent sparse LBL array calibration and transceiver parameter estimation should be possible with a suitable trajectory and a pre-calibrated DVL/INS.

[4]

References C

[C1] Robert Grover Brown and Patrick Y. C. Hwang. *Introduction to Random Signals and Applied Kalman Filtering*. 3rd ed. Wiley, 1996, p. 496. ISBN: 0471128392.

[C2] *Department of Defense World Geodetic System 1984, Its Definition and Relationships With Local Geodetic Systems*. Tech. rep. National Imagery and Mapping Agency, 2004. DOI: TR8350.2.

[C3] Paul D. Groves. *Principles of GNSS, Inertial, and Multisensor Integrated Navigation Systems, Second Edition*. Artech House, 2013, p. 800. ISBN: 1608070050.

[4] Note that identifying company stickers were removed from select photos.

[C4] Martin Juhl Jørgensen, Mikael Bliksted Larsen, and Niels K. Poulsen. "Subsea Metrology Using SLAM sparse LBL Acoustically Aided INS". unpublished. 2015.

[C5] Martin J. Jørgensen et al. "IMU calibration and validation in a factory, remote on land and at sea". In: *2014 IEEE/ION Position, Location and Navigation Symposium - PLANS 2014*. IEEE, May 2014, pp. 1384–1391. ISBN: 978-1-4799-3320-4. DOI: 10.1109/PLANS.2014.6851514.

[C6] Mikael Bliksted Larsen. "Autonomous navigation of underwater vehicles". PhD. Technical University of Denmark, 2001.

[C7] P. Newman and J. Leonard. "Pure range-only sub-sea SLAM". In: *2003 IEEE International Conference on Robotics and Automation* 2 (2003), pp. 1921–1926. ISSN: 1050-4729. DOI: 10.1109/ROBOT.2003.1241875.

[C8] M Norgaard, NK Poulsen, and Ole Ravn. "Advances in derivative-free state estimation for nonlinear systems". In: *Automatica* (2000).

[C9] Alejandro Palmeiro et al. "Underwater radio frequency communications". In: *OCEANS 2011 IEEE - Spain*. IEEE, June 2011, pp. 1–8. ISBN: 978-1-4577-0086-6. DOI: 10.1109/Oceans-Spain.2011.6003580.

[C10] A.P. Scherbatyuk. "The AUV positioning using ranges from one transponder LBL". In: *'Challenges of Our Changing Global Environment'. Conference Proceedings. OCEANS '95 MTS/IEEE*. Vol. 3. IEEE, 1995, pp. 1620–1623. ISBN: 0-933957-14-9. DOI: 10.1109/OCEANS.1995.528728.

[C11] *Sonardyne International Ltd.* URL: http://www.sonardyne.com.

[C12] David Titterton. *Strapdown Inertial Navigation Technology, 2nd Edition*. IET, 2004, p. 558. ISBN: 0863413587.

[C13] E.A. Wan and R. Van Der Merwe. "The unscented Kalman filter for nonlinear estimation". In: *Proceedings of the IEEE 2000 Adaptive Systems for Signal Processing, Communications, and Control Symposium (Cat. No.00EX373)*. IEEE, 2000, pp. 153–158. ISBN: 0-7803-5800-7. DOI: 10.1109/ASSPCC.2000.882463.

[C14] Are B. Willumsen, Oddvar Hallingstad, and Bjørn Jalving. "Integration of range, bearing and doppler measurements from transponders into underwater vehicle navigation systems". In: *Oceans 2006* Dvl (2006). DOI: 10.1109/OCEANS.2006.306851.

Paper D

3D subsea mapping from lidar and acoustically aided INS

Authors:
Martin J. Jørgensen, Jimmie Borch, Mikael B. Larsen and Niels K. Poulsen

Submitted to:
IEEE Journal of Oceanic Engineering 2015.

3D subsea mapping from lidar and acoustically aided INS

Martin J. Jørgensen[1], Jimmie Borch[1], Mikael B. Larsen[2] and Niels K. Poulsen[1]

Abstract

This paper investigates a time efficient approach to high accuracy 3D subsea mapping using a Remotely Operated Vehicle (ROV). The ROV is equipped with a high resolution (mapping) sensor (lidar, stereo vision, high-resolution sonar, etc.) and a highly optimized acoustically aided inertial navigation system (AAINS). Mapping is achieved via vehicle motion across the area of interest and combining sensor data with dynamic position/orientation data. The concept of operation is widely used in lidar-GNSS/INS based land survey. We treat the plethora of challenges imposed by the GNSS denied subsea domain and application for subsea metrology: AAINS and sensor calibration ("patch test"), simultaneous localization and mapping (SLAM) sparse Long BaseLine (LBL) and 6DOF feature matching. Unique experimental results obtained from a state-of-the-art instrumented work-class ROV operated in 2800m water depth are presented and demonstrate practical accuracy and resolution to the cm level.

D.1 Introduction

TECHNOLOGICAL advances within terrestrial navigation systems and mapping sensors have revolutionized land surveying. Anyone can take accessible commercial off-the-shelf integrated 3D mapping system, including vehicle—aerial drones are popular—and start producing high-resolution and high-accuracy georeferenced 3D maps. This can largely be attributed to cheap survey grade Global Navigation Satellite Systems (GNSS) and micro-electromechanical system (MEMS) based Inertial Navigation Systems (INS). Mapping sensors, e.g.

[1]Department of Applied Mathematics and Computer Science, Technical University of Denmark, DK-2800 Kgs. Lyngby, Denmark
[2]Sonardyne International Ltd., Yateley, United Kingdom

lidar [D22], multibeam sonar echo sounder (MBES), stereo camera, structured light camera systems, etc., are not new to the field of subsea mapping, but a paradigm shift has yet to happen for everyday subsea survey operations. A lack of robust high accuracy navigation have made current methods either require a considerable amount of post-processing time [D19] or apply only to static applications [D1, D2]. High resolution MBESs are widely used, but so far cm-level map resolution has only been achieved on a regular basis with surface vessels and survey grade GNSS navigation. Recent advances have been made with both lidar, MBES and photogrammetry [D5, D8].

This paper investigates a time efficient approach to high accuracy 3D subsea mapping using an ROV. The vehicle is equipped with a high resolution (mapping) sensor and a highly optimized AAINS. Mapping is achieved through vehicle motion across the area of interest and combining sensor data with dynamic navigation (position, orientation and velocity) data. We consider the subsea survey problem *metrology* [D3, D13] where the distance between two objects (baseline), their relative orientation and the seabed profile along the baseline are of interest.

We treat the many challenges imposed by the GNSS denied subsea domain and application for subsea metrology: AAINS and sensor calibration, SLAM sparse LBL navigation with uncertain acoustic transponder positions. Our method estimates the position and orientation of (parts of) the subsea structures by fitting a known 3D model of the objects to the 3D point cloud. The baseline and relative orientation are derived from the estimated target poses, and the seabed profile along the baseline can be extracted from the point cloud. This method qualifies as "contactless metrology", i.e. since there is no physical contact with the structures, minimizing risk of damage.

Following the pattern from land/aerial survey, application of the technology, once proven, is expected to spread into the subsea domain. Beyond fast 3D high-resolution and high-accuracy mapping, routine but time-consuming tasks like asset monitoring and metrology can easily be developed. In a not-so-distant future, integration between a real-time 3D world and the ROV pilots can increase the operational envelope, as is in military aircrafts and helicopters.

Section D.2 introduces the AAINS and framework. Mapping sensors are discussed in section D.3 and the metrology application in section D.4. Section D.5 applies our method to a full metrology set-up, in simulation. Initial field testing results using the proposed method is given in section D.6, followed by a conclusion in section D.7.

D.2 Navigation

An INS is a dead-reckoning system that allows any vehicle to be positioned, in the short term, accurately without having to rely on models of vehicle dynamic. Motion is sensed by three accelerometers and three gyroscopes inside the INS, referred to as the inertial measurement unit (IMU). In a strapdown system the IMU follows the motion of the vehicle, i.e. unlike stable-platform mechanical gyroscopes. Throughout this paper the notation $\boldsymbol{r}^{\mathrm{c}}_{\mathrm{ab}}$ means the vector from point b to point a expressed in c-frame, (or $\boldsymbol{r}^{\mathrm{c}}_{\mathrm{b}}$ if a is implicitly given) and the direction cosine matrix (DCM) $\mathrm{C}^{\mathrm{c}}_{\mathrm{b}}$ is the rotation from b-frame to c-frame, with the relevant reference frames:

navigation	Local-level North–East–Down (NED) frame.
body	Frame with axes coinciding with the IMU axes.
sensor	Frame with axes coinciding with the aiding sensor's axes.
map	A local-level Cartesian mapping frame.
intersection	The frame coincident with the intersection of a beam and the environment, e.g. target subsea structure.

To enhance accuracy, the AAINS is aided by measurements from a Doppler velocity log (DVL), pressure depth and acoustic LBL ranges. Typical sensor accuracies are given in Table D.1. A centralized error-state Kalman filter (ESKF) [D9, D28] is fusing the INS dead-reckoning navigation with the aiding observations, as shown in Fig. D.1. Error-state means that the ESKF states are estimated INS navigation errors, i.e. *depth error* as compared to *depth*. Applying the error-states to the INS gives the estimated AAINS navigation solution. The widely used, and domain standard, extended Kalman filter (EKF) [D7, D9, D27] is used. Navigation estimates are improved by applying a Rauch-Tung-Striebel (RTS) [D7, D25] fixed-interval Kalman smoother. Kalman smoothing both improves the estimated mean and covariance, but also smooth out the jagged ESKF corrections. For mapping, smooth navigation is preferred as vehicle motion is continuous, not discrete, thus a jump in the map should be physical and and not an artifact of navigation.

The IMU is calibrated during manufacturing [D17]. In addition, AINSs estimates certain residual IMU errors such as scale-factor and biases in real-time.

Subsea AAINS for survey is typically aided with velocity from a DVL [D9, D14, D15, D20, D29]. DVL measured velocity is expressed in the DVL frame so knowledge of bore-sight alignment and scale-factor is necessary and often included in error models.

LBL measures the acoustic two-way travel-time, the round-trip time, between

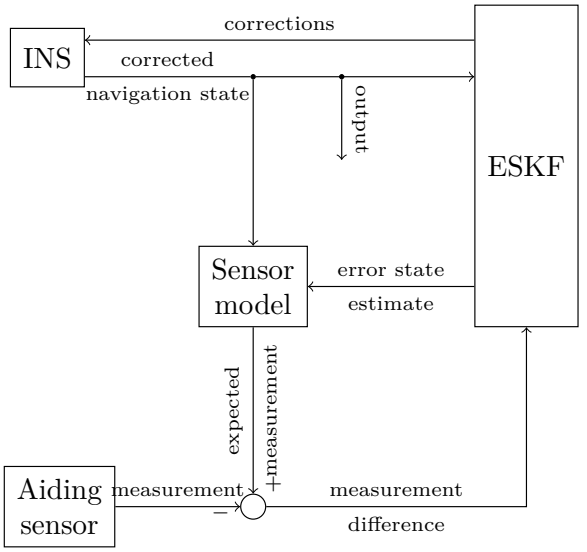

Figure D.1: General AINS framework. The corrections are either fed back to the INS, or alternatively applied to the INS output. If the former is true, the error state must be reset for each feedback. INS output is the *navigation state*: position, velocity, orientation, turn rate and acceleration.

the transceiver and one or more (seabed) transponders [D9, D20]. The sound velocity along the acoustic baseline is required for accurate navigation. The number of transponders is reduced, and thus costly deployment time, by using Sparse LBL [D20, D23, D26] i.e., substituting transponders with measurements from different positions. As the metrology outcome is relative and not absolute georeferenced [D13], the LBL array does not need to be accurately calibrated from a surface vessel. Since transponders with uncertain positions can be used for accurate relative navigation by augmenting the AAINS [D16, D23, D30], deployment time is further reduced.

To achieve high accuracy the lever arms and mounting angles of the aiding sensors must be known accurately. For work offshore this is often cumbersome and error-prone. Using a co-located and pre-calibrated INS/DVL solution helps, but the LBL transceiver lever arm needs to be known accurately also. Parameter estimation techniques can be employed [D15] to either estimate a completely unknown parameter or to refine measured quantities.

Table D.1: Sensor and typical observation accuracies

Sensor	Observation	Accuracy (σ)	Unit
INS	roll and pitch	0.01	°
INS	heading	0.05[a]	°
DVL	seabed relative velocity	0.2	cm/s
LBL	range	1.5	cm
Depth	pressure depth	0.2[b]	m
Lidar	range	0.6	cm

[a] scales with $\sec(L)$.
[b] given as 0.01% of full scale; roughly 0.2 m for these trials.

D.3 3D mapping sensor

A point sensor measurement ℓ can in its simplest form be defined by a range and a direction:

$$\ell = (t, \rho, \boldsymbol{u}) \,, \tag{D.1}$$

where t denotes the time of measurement, ρ denotes the range to the target, and $\boldsymbol{u}$ is the unit vector from the reference point of the sensor to the target. The direction $\boldsymbol{u}$ is reported by the point sensor in a format that may vary from sensor to sensor. For a lidar [D24] and a MBES [D12] this direction is typically defined by one or two angles, e.g. determined by the orientation of two internal mirrors inside the lidar sensor. Additional measures may be reported by the sensor. Most point sensors will report the strength of the return signal (amplitude/intensity). This measure provides information about the target and may be useful in classification of the 3D point target.

The generation of the point cloud itself is straight forward, assuming the system parameters, lever arm $\boldsymbol{l}_{\mathrm{b}}^{\mathrm{s}}$ and orientation $\mathrm{C}_{\mathrm{b}}^{\mathrm{s}}$, are known. The beam foot print, or world intersection, relative to the navigation frame $\boldsymbol{r}_{\mathrm{int}}^{\mathrm{n}}$, is given by

$$\begin{aligned} \boldsymbol{r}_{\mathrm{int}}^{\mathrm{n}} &= \boldsymbol{r}_{\mathrm{s}}^{\mathrm{n}} + \mathrm{C}_{\mathrm{b}}^{\mathrm{n}} \mathrm{C}_{\mathrm{s}}^{\mathrm{b}} \boldsymbol{u} \rho & \text{(D.2)} \\ &= \boldsymbol{r}_{\mathrm{b}}^{\mathrm{n}} + \mathrm{C}_{\mathrm{b}}^{\mathrm{n}} \left[\mathrm{C}_{\mathrm{s}}^{\mathrm{b}} \boldsymbol{u} \rho + \boldsymbol{l}_{\mathrm{s}}^{\mathrm{b}} \right] & \text{(D.3)} \end{aligned}$$

here n denotes coordinates in a local Cartesian reference frame, and $\boldsymbol{r}_{\mathrm{b}}^{\mathrm{n}}$ and $\mathrm{C}_{\mathrm{b}}^{\mathrm{n}}$ is, respectively, the position and orientation of the vehicle delivered by the navigation system. Time-synchronization between the point sensor and the navigation system is critical to ensure that the point cloud is correctly resolved.

D.3.1 Point sensor calibration

Sensor calibration in this paper is referring to calibrating the point sensor to the navigation system, unless otherwise stated. High resolution and high accuracy mapping necessitate well known lever arm and mounting angle. The effect of error range from from outright wrongful to loss of detail in the resolved point cloud. Calibration routines are needed as accurately measuring all six degrees-of-freedom can be challenging if not impractical. This sensor calibration is typically realized by a *patch test* [D4, D10, D18]. Elegant and more elaborate techniques exists for 3D scanners, as they provide more abundant information than 2D scanners, such as auto-calibration and/or exploiting return-signal amplitude/intensity/remittance/reflectivity [D21] for calibration.

For all 6-DOF to be determined the combination of data and navigation must excite all parameters, which can include calibration targets with known geometry, e.g. "reflective" spheres [D2]. For a planar patch sufficient trajectory dynamics must include translation to make mounting angles observable, and rotation to make the lever arm observable.

D.4 Contactless Metrology

The concept of operation is to map the structures and seabed of interest in a single pass, using a mapping sensor and an AAINS. Position and orientation from AAINS is used to resolve the mapping sensor data to a 3D point cloud. Known 3D models of the targets, or parts of them, are fitted to the point cloud to more accurately estimate their position and orientation. This is all the information needed to derive the metrology metrics: baseline, relative orientation and the seabed profile.

With the AAINS and mapping sensor calibrated, a simple straight line trajectory, directly above the targets, is all that is required for this contactless metrology method. A second pass in opposite direction is advised for quality control purposes. This straight line trajectory reduces influence of numerous error sources, e.g. heading error, lever arm errs, etc.

With a resolved 3D point cloud available, a qualified starting guess for the feature can either be automated or an operator can approximate location and orientation. Global matching is a task that humans inherently do well, but is challenging for a computer. The coarse estimates are refined using an iterative algorithm. From the the optimized estimates the metrology baseline, relative

orientation and seabed profile can be extracted.

Feature matching is solved by employing a variation of the iterative closest point (ICP) algorithm [D6]. ICP is often used for the problem of consistently aligning various 3D point cloud data views into a complete model, known as registration. In this work a method utilizing the precise description of the model as a triangle mesh is used, by minimizes the point-to-triangle normal distance. Inspired by [D11], this technique matches a data point q_i to a triangle in the model if the normal distance is the shortest, and the projection of the point p_i onto the plane of the triangle lies inside the triangle. Given a 3D point cloud and a 3D triangular mesh model, the algorithm will iteratively minimize any disparity between the observations and model. In each iteration, each point in the point cloud, q_i, is matched to a triangle in the 3D model, and the error metric

$$E_k = \sum_{i=1}^{N} |\mathrm{C}_{\mathrm{k}}^{\mathrm{k}^*} p_i + \boldsymbol{r}_{\mathrm{k}}^{\mathrm{k}^*} - q_i|^2 \tag{D.4}$$

is minimized to obtain the Euclidean translation $\boldsymbol{r}_{\mathrm{k}}^{\mathrm{k}^*}$ and rotation given by the DCM $\mathrm{C}_{\mathrm{k}}^{\mathrm{k}^*}$ for the k-th feature. The feature is then updated accordingly in mapping frame

$$\mathrm{C}_{\mathrm{k}^*}^{\mathrm{m}} = \mathrm{C}_{\mathrm{k}}^{\mathrm{m}} \mathrm{C}_{\mathrm{k}^*}^{\mathrm{k}} \tag{D.5}$$

$$\boldsymbol{r}_{\mathrm{k}^*}^{\mathrm{m}} = \boldsymbol{r}_{\mathrm{k}}^{\mathrm{m}} + \boldsymbol{r}_{\mathrm{k}^*}^{\mathrm{k}} \tag{D.6}$$

with position $\boldsymbol{r}_{\mathrm{k}}^{\mathrm{m}}$ and orientation $\mathrm{C}_{\mathrm{k}}^{\mathrm{m}}$ for the k-th feature.

For planning subsea piping installation an obvious choice for a feature might be the flange, hub or even the entire structure. For subsea construction a 3D computer-aided design (CAD) model will most likely be available. Alternatively, it is feasible to 3D scan part of the structure, even offshore, with available modern technology.

After matching all features, the metrology baseline ζ and the structure relative orientation (Euler angles) $\boldsymbol{\psi} = \begin{bmatrix} \alpha & \beta & \gamma \end{bmatrix}^\top$ are derived:

$$\zeta_{ij} = \|\boldsymbol{r}_j - \boldsymbol{r}_i\|_2 \tag{D.7}$$

$$[\boldsymbol{\psi_{ij}}\times] = \mathrm{C}_{\mathrm{m}}^{\mathrm{j}} \mathrm{C}_{\mathrm{i}}^{\mathrm{m}}, \tag{D.8}$$

where $[(\cdot)\times]$ denotes skew-symmetric form. The seabed profile is not considered here as it is trivial to extract it from the resolved 3D point cloud: it is literally the entire sea bed between the two structures, in the point cloud.

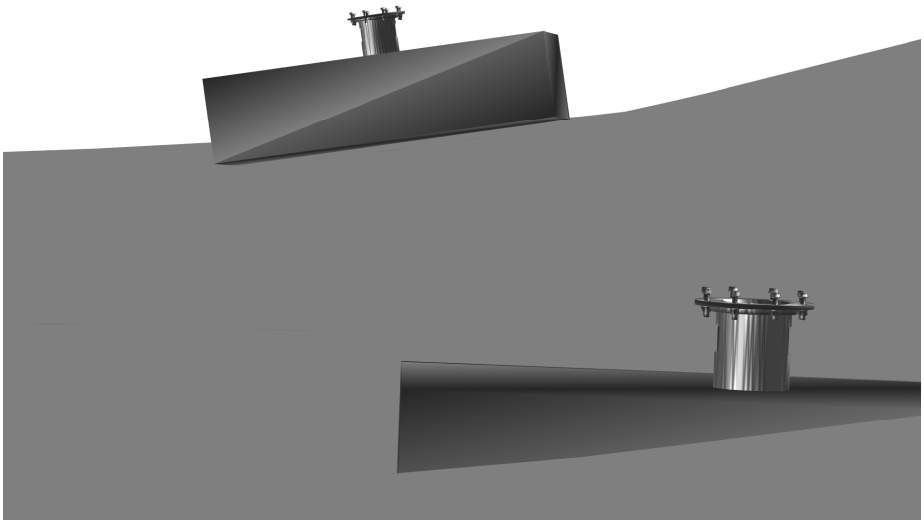

Figure D.2: 3D simulation world with two structures placed 50 meter apart, with different orientations. Each structure features a flange aligned to the surface normal.

D.5 Simulation Study

The accuracy of our contactless metrology method is investigated in a small simulation study. We created a 3D environment with a seabed and two subsea structures shown in Fig. D.2. The seabed was taken from a MBES survey and scaled to match the desired resolution of a lidar. A reference survey trajectory, Fig. D.3, was chosen such that most of structures were swiped by the mapping sensor as well as the seabed between them. From this truth model IMU, pressure depth, DVL, LBL and lidar data was simulated with characteristics as those listed in Table D.1.

Processing the IMU and aiding data yields a smoothed AAINS navigation solution using sparse LBL, as described in Section D.2. Navigation estimation error and accuracy are given in Fig. D.4.

Two scenarios are investigated: an error-free case with perfect knowledge of the extrinsic mapping sensor parameters, with navigation errors still present; and a scenario with realistic parameter uncertainty from measurements or from a patch-test. In the latter case the point sensor lever arm had a std.dev. of 5

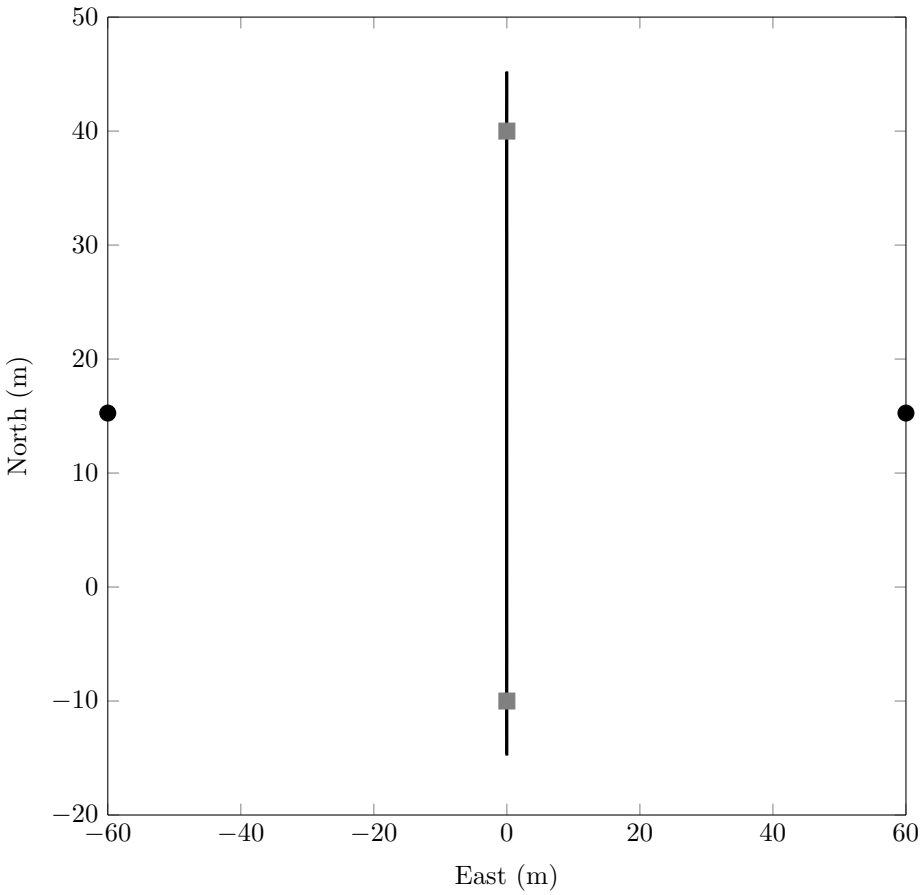

Figure D.3: Simulation trajectory, 5 min initialization, followed by two passes, in opposite directions. Transponders are marked with black circles, structures with gray boxes.

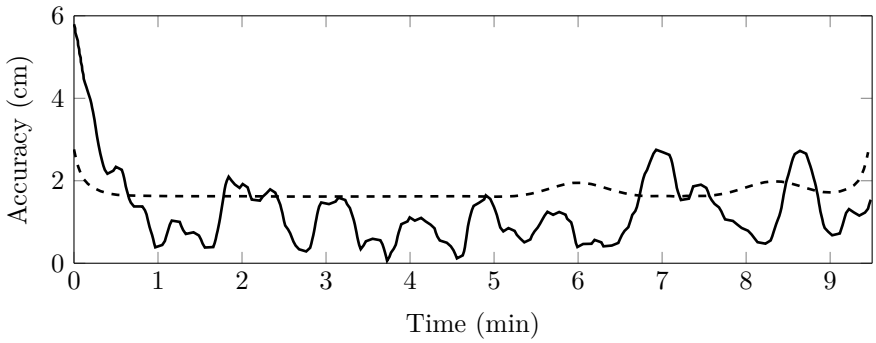

Figure D.4: Radial navigation error for simulation. Solid line is the relative radial error and the dashed line the 1-DRMS. 5 min initialization, followed by two passes, in opposite directions.

cm in each axis, mounting angle error of std.dev. 5 deg around each axis and a latency of std.dev. 0.1 s. Since manual interaction is required to select coarse guesses a limited number of 10 simulations were carried out.

The investigated method requires a 3D model of a target object. For this study we picked a "standard-sized" subsea flange as the target. Fig. D.5 shows the final fit of the cloud point to the flange model, for one of the two targets. Similar correspondence was achieved for the second target. The metrology baseline error $\delta\zeta$ and relative orientation error $\boldsymbol{\delta\psi} = \begin{bmatrix}\delta\alpha & \delta\beta & \delta\gamma\end{bmatrix}^\top$ derived from the estimated poses of the two flanges are listed in Table D.2, for each pass. Only the two angular errors, $\delta\alpha$ and $\delta\beta$, relevant for vertical metrology are listed since the flange is rotation symmetric around γ[3]. The discrepancy between the two passes can be explained by the fact that they are not independent, but correlated. While Kalman smoothing improves the whole navigation, trajectory dependent navigation errors will still be present.

D.6 Sea trial

We investigated lidar-metrology during a sea trial, in cooperation with Monterey Bay Aquarium Research Institute (MBARI), in depths of approximately 2800 meter in the Monterey Bay Canyon. In a unique experiment the MBARI ROV Doc Ricketts was fitted with state-of-the-art navigation and mapping equip-

[3]The small "windows" in the cylinder seen in Fig. D.5, is not detected with a down-ward pointing mapping sensor.

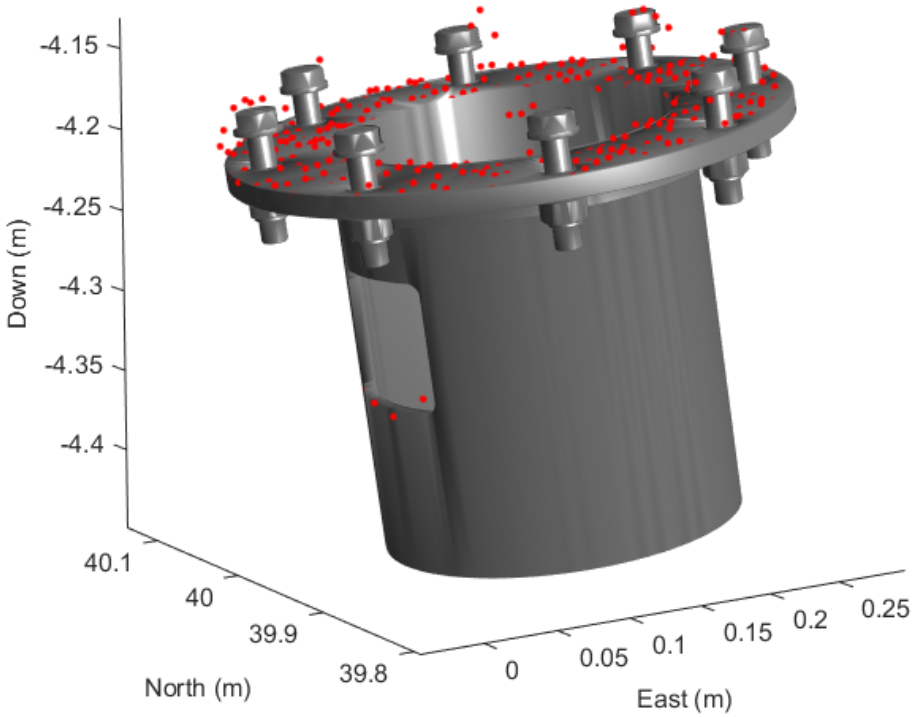

Figure D.5: 3D CAD model of a standard subsea construction flange, used as target, matched to part of point cloud

Table D.2: Simulation study metrology baseline error $\delta\zeta$ and relative orientation error components $\delta\alpha$ and $\delta\beta$, for each pass in opposite direction. The error scenario was repeated 10 times with the mean and worst case highlighted here.

Scenario	$\delta\zeta$ (cm)	$\delta\alpha$ (°)	$\delta\beta$ (°)
1st pass			
No error (mean)	3.82	0.23	0.25
No error (worst)	6.44	0.60	0.66
Error (mean)	4.68	0.22	0.25
Error (worst)	9.81	0.45	0.49
2nd pass			
No error (mean)	4.40	0.22	0.62
No error (worst)	7.32	0.36	0.98
Error (mean)	4.67	0.35	0.73
Error (worst)	11.30	0.70	1.02

ment, including subsea lidar, stereo camera, MBES, AAINS with DVL and LBL, as depicted in Fig. D.6. Sensor mounts were precision-machined and all lever arms were meticulously measured and triple-checked, ensuring that the nominal extrinsic sensor parameters were well known. The ROV was kept leveled, i.e. minimal roll and pitch, and maintained at 3 m altitude above the sea-bed throughout the trial. Fig. D.7 shows the trajectory. Cruising at 0.1 m/s, the lidar was pointing nominally down and set to profile mode, i.e. line scan, and configured for 1 cm spacing across and along track at 0.1 m/s, 3 m off the bottom. A calibrated array of three mini LBL transponders, as depicted in Fig. D.8, approximately 10 cm in diameter and 50 cm tall, was deployed with the geometry shown in Fig. D.7.

Lidar data was filtered for disturbances in the water, e.g. fish, using a simple approach:

$$\left.\begin{aligned} &|\rho_i - \rho_{i-1}| > \epsilon\rho_{i-1} \\ \text{and}\quad &|\rho_i - \rho_{i+1}| > \epsilon\rho_{i+1} \end{aligned}\right\} \Rightarrow i \text{ is outlier}, \tag{D.9}$$

with $\epsilon = 10\%$. Considering the likely dense nature of the data this approach should not cause significant gaps in the data. A smoothed two-transponder sparse LBL AAINS solution was used to resolve the lidar data into a 3D point cloud. Transponders 1 and 2 served as metrology targets, with the calibrated

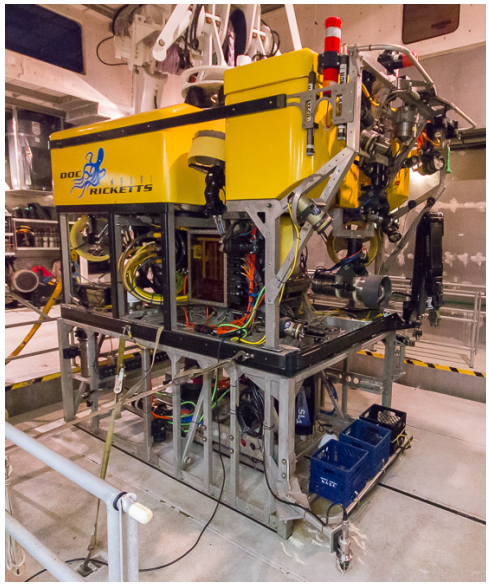

Figure D.6: ROV Doc Ricketts, onboard the R/V Western Flyer, with exceptionally tall toolsled.

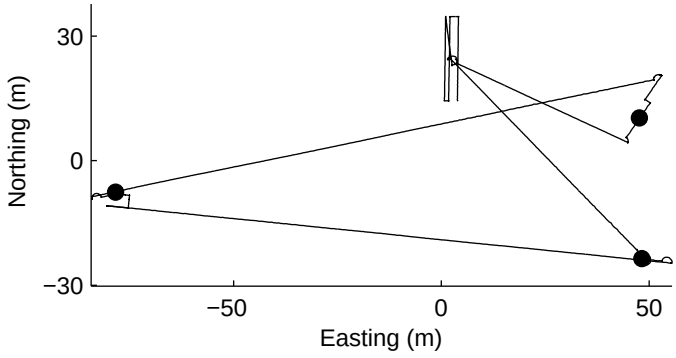

Figure D.7: Sea trial trajectory. Mini transponders are marked with circles.

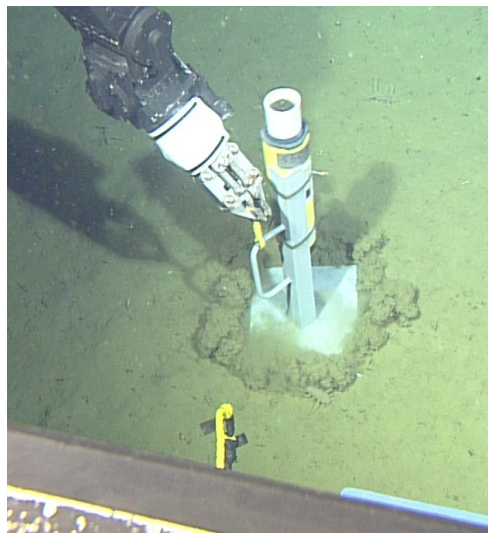

Figure D.8: Mini transponder deployment with ROV manipulator. Image courtesy of MBARI.

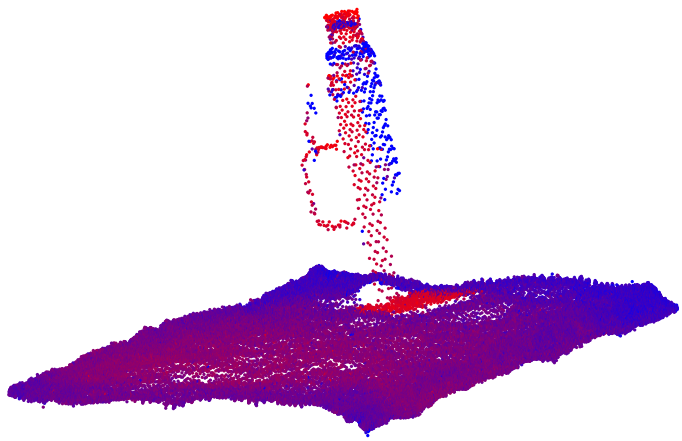

Figure D.9: Lidar point cloud of transponder 2 colored by the amplitude of the return signal, from a single pass. Redder equals higher amplitude. Notice how the metal stand and bright plastic area have the highest amplitude and the rubber sleeve (yellow part in Fig. D.8) has the lowest.

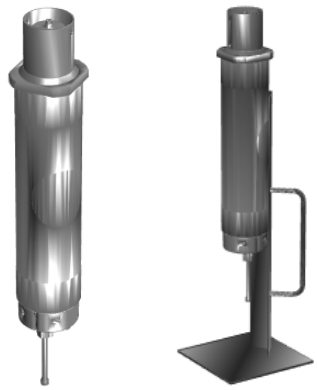

Figure D.10: 3D model used for matching (left) and with added stand used for simulation (right).

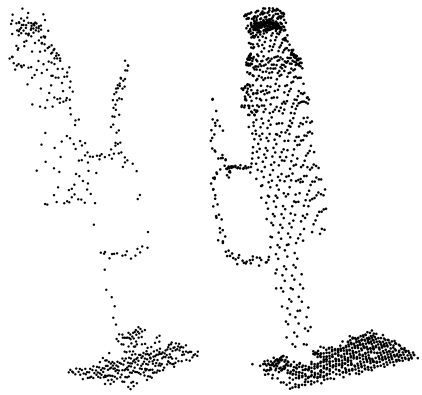

Figure D.11: Lidar point cloud of transponder 1 (left) and transponder 2 (right).

LBL array providing an accurate reference baseline[4]. The transponder–transponder relative orientation and the seabed profile between them are omitted as no references were available. The 3D model of the transponders, as shown in Fig. D.10 was used for model matching. Points from the cloud were manually selected as input to the model matching. We experimented with a few different approaches for automatic selection: selecting everything above seabed, and selection based on the lidar amplitude information (see Fig. D.9). Since the environment was flat and mostly natural—as compared to man-made—these all yielded similar results. In a commercial offshore environment these automatic selection techniques may not be as applicable.

Data from the ROV hovering above a transponder resulted in a blob of points instead of a "crisp" transponder. Investigating this issue revealed an unexpected latency to be the largest error contribution—similar blurriness was obtained by simulating latency between the navigation system and the lidar. The latency δt was recovered by minimizing the point-to-point difference between matching pairs in two clouds: The green point cloud is iteratively matched to the closest point in the red point cloud (see Fig. D.12), a similar approach is used in the ICP algorithm, minimizing the objective function

$$\min_{\delta t} \sum_{(A,B)\in\mathcal{M}} \|f(\delta t, \ell_A) - f(\delta t, \ell_B)\|_2, \tag{D.10}$$

where $f(t, \ell)$ resolves the lidar measurement ℓ with latency t into the point cloud, and $\mathcal{M}$ is the set of matches between the two point clouds A and B. This optimization yields a latency of $\delta t = 0.266\,\mathrm{s}$ and results in the point cloud shown in Fig. D.12.

A simulation of the trial was carried out to serve as a benchmark, a lower boundary for what to expect from the trial data. An optimized and smoothed AAINS reference solution was derived using the full LBL array. A reference 3D world was created with the transponder truth model shown in Fig. D.10. Using this reference 3D world and navigation as ground truth, aiding and lidar data were simulated according to Table D.1. Both the simulated and trial data were processed identically, both in terms of navigation and point-cloud processing. Metrology simulation and trial results are given in Tabel D.3.

[4]The reference baseline has a "standard deviation" that is measured in mm, derived from repeated measurements from their static positions.

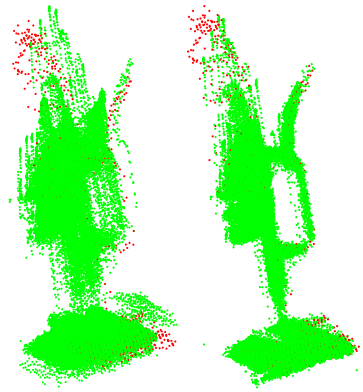

Figure D.12: Point clouds of two passes of transponder 1 before (left) and after (right) latency calibration.

D.7 Conclusion

This paper proposed, investigated and experimentally validated a new and extremely time efficient methodology for ultra high accuracy contactless seabed and structure mapping and metrology: A survey instrumented vehicle (ROV, AUV, ...) travels across the area of interest. A map is created by combining data from a high-resolution 3D point sensor with time-synchronized navigation data (sensor position and orientation) from a high-accuracy navigation system, e.g. an AAINS. The "3D point sensor" can be e.g. a lidar, laser striper/camera combination (structured light), MBES or a photogrammetry system variant, e.g. synthetic/structure from motion or stereo camera system or any other type of mapping sensor. Accurate and time efficient navigation is performed from a combination of some or all of the following sensors and navigation techniques: IMU, AHRS, (Acoustically Aided) INS, ZUPT, pressure depth, DVL (beam or body frame velocity), LBL (sparse and/or SLAM and/or range/pseudo range), USBL, sound velocity, tide, auto calibration of lever arms, mounting angles and other inertial, aiding or point sensor parameters and post-processing (forwards-backwards Kalman smoothing).

The metrology parameters (slant ranges and orientations) may be derived from the generated 3D point cloud and can be enhanced using 3D point cloud processing techniques to precisely fit known 3D models of the sought after flanges/hubs/structures, e.g. variants of the ICP algorithm.

Unique experimental validation results were obtained from a state-of-the-art instrumented work-class ROV operated in 2800 meter water depth. A con-

Table D.3: MBARI metrology trial results. The baseline difference $\Delta\zeta$ is derived from the LBL reference for trial data and from the truth model for the simulation scenario.

Scenario	$\Delta\zeta$ (cm)
Nominal parameters	-1.4
Latency corrected	-3.6
Simulation	1.4

ventional calibrated LBL seabed transponder array was used as both position reference and targets for metrology. SLAM sparse LBL with post-processing (Kalman smoothing) was performed using 2 of the array transponders and treating their positions unknown. The baseline difference (1.4–3.6 cm) demonstrates practical feasibility of contactless metrology using lidar on a rover. A significant latency (0.266 s) was exposed in the raw data, but this goes to show the robustness of the method with regards to latency.

Practically attainable contactless metrology accuracies for baseline (2–4 cm) and relative orientation (0.1–1.4 deg) is suggested by a simulation study, using only a flange as target. Orientation accuracy can be increased by using a larger target, i.e. the whole structure, but as the simulation study shows the accuracy using a flange should suffice. The seabed profile is not treated in detail as this is simply a matter of extracting the information from the 3D point cloud.

The proposed method requires a 3D model of (a part of) the structure which should be readily available, or easily obtained. Matching works even with partly obscured objects, as results from the sea trial show. The 3D point cloud itself could be the end result to the surveyors, but having a computer assisted semi-automated tool simply removes a handful of manual steps. Moreover, the 3D point cloud is still available should trouble arise.

The simple line trajectory chosen for metrology in this paper is robust regarding the accuracy of the mapping sensor lever arm, mounting angles and latency. General high resolution and high accuracy 3D mapping epitomize the need for extrinsic mapping-sensor calibration, as small errors will be highly visible as artifacts in generated 3D maps. Dealing with the navigation problem and mapping

problem separately cause the sensor calibration to include navigation error. This might be mitigated by solving the navigation and calibration problem simultaneous, using techniques from simultaneous localization and mapping (SLAM).

Acknowledgment

The authors would like to thank MBARI, and especially S. Etchemendy and Dr. D. Caress, for the opportunity to collaborate on this sea trial. A thanks also goes out to Dr. G. Troni, to H. Thomas for his hard work and assistance, to the ROV pilots K. Brekke, M. Talkovic, R. Prickett, B. Schaefer, and B. Erwin and to the rest of the skilled crew of the R/V Western Flyer.

References D

[D1] 2G Robotics. *Spool Metrology with 2G Robotics' ULS-500*. 2015. URL: http://www.2grobotics.com/spool-metrology-with-2g-robotics-uls-500/ (visited on 09/06/2015).

[D2] 3D at Depth. *Laser Metrology*. URL: http://www.3datdepth.com/laser-metrology/ (visited on 09/06/2015).

[D3] Frederic Auger and Keith Vickery. "The operational evaluation of an inertial navigation technique for the provision of underwater metrology surveys". In: *Underwater Technology: The International Journal of the Society for Underwater* 30.2 (Nov. 2011), pp. 103–112. ISSN: 17560543. DOI: 10.3723/ut.30.103.

[D4] Ki-In Bang. "Alternative Methodologies for LiDAR System Calibration". PhD. University of Calgary, 2010.

[D5] Katherine Bell and Sarah Fuller. "New Frontiers in Ocean Exploration: The E/V Nautilus 2010 Field Season". In: *Oceanography* 24.1 (Mar. 2011), pp. 1–40. ISSN: 10428275. DOI: 10.5670/oceanog.24.1.supplement. URL: http://digitalcommons.uri.edu/gsofacpubs/13.

[D6] P.J. Besl and H.D. McKay. "A method for registration of 3-D shapes". In: *IEEE Transactions on Pattern Analysis and Machine Intelligence* 14.2 (1992), pp. 239–256. ISSN: 01628828. DOI: 10.1109/34.121791.

[D7] Robert Grover Brown and Patrick Y. C. Hwang. *Introduction to Random Signals and Applied Kalman Filtering*. 3rd ed. Wiley, 1996, p. 496. ISBN: 0471128392.

[D8] D.W. Caress et al. *Repeat 1-cm Resolution Topographic And 2.5-mm Resolution Photomosiac Surveys Of A Chemosynthetic Clam Community In Monterey Canyon*. 2014.

[D9] Paul D. Groves. *Principles of GNSS, Inertial, and Multisensor Integrated Navigation Systems, Second Edition*. Artech House, 2013, p. 800. ISBN: 1608070050.

[D10] D. Gueriot et al. "The patch test: a comprehensive calibration tool for multibeam echosounders". In: *OCEANS 2000 MTS/IEEE Conference and Exhibition. Conference Proceedings (Cat. No.00CH37158)*. Vol. 3. IEEE, 2000, pp. 1655–1661. ISBN: 0-7803-6551-8. DOI: 10.1109/OCEANS.2000.882178. URL: http://ieeexplore.ieee.org/lpdocs/epic03/wrapper.htm?arnumber=882178.

[D11] Ayman F. Habib et al. "Automatic surface matching for the registration of LIDAR data and MR imagery". In: *ETRI Journal* 28.2 (2006), pp. 162–174. ISSN: 12256463. DOI: 10.4218/etrij.06.0105.0107.

[D12] Laurent Hellequin, Jean Marc Boucher, and Xavier Lurton. "Processing of high-frequency multibeam echo sounder data for seafloor characterization". In: *IEEE Journal of Oceanic Engineering* 28.1 (2003), pp. 78–89. ISSN: 03649059. DOI: 10.1109/JOE.2002.808205.

[D13] IMCA. *Guidance on Subsea Metrology*. London, 2012. URL: http://www.imca-int.com/media/70581/imcas019.pdf.

[D14] Bjørn Jalving et al. "DVL velocity aiding in the HUGIN 1000 integrated inertial navigation system". In: *Modeling, Identification and Control* 25.4 (2004), pp. 223–235. ISSN: 03327353. DOI: 10.4173/mic.2004.4.2.

[D15] Martin J. Jørgensen, Mikael B. Larsen, and Niels K. Poulsen. "Approaching cm-level relative accuracy in underwater navigation". unpublished. 2015.

[D16] Martin Juhl Jørgensen, Mikael Bliksted Larsen, and Niels K. Poulsen. "Subsea Metrology Using SLAM sparse LBL Acoustically Aided INS". unpublished. 2015.

[D17] Martin J. Jørgensen et al. "IMU calibration and validation in a factory, remote on land and at sea". In: *2014 IEEE/ION Position, Location and Navigation Symposium - PLANS 2014*. IEEE, May 2014, pp. 1384–1391. ISBN: 978-1-4799-3320-4. DOI: 10.1109/PLANS.2014.6851514.

[D18] Ana Paula Kersting et al. "Automated approach for rigorous light detection and ranging system calibration without preprocessing and strict terrain coverage requirements". In: *Optical Engineering* 51.7 (2012), p. 076201. ISSN: 00913286. DOI: 10.1117/1.OE.51.7.076201.

[D19] Tom Kwasnitschka et al. "Doing fieldwork on the seafloor: Photogrammetric techniques to yield 3D visual models from ROV video". In: *Computers & Geosciences* 52 (Mar. 2013), pp. 218–226. ISSN: 00983004. DOI: 10.1016/j.cageo.2012.10.008. URL: http://www.sciencedirect.com/science/article/pii/S0098300412003482.

[D20] Mikael Bliksted Larsen. "Autonomous navigation of underwater vehicles". PhD. Technical University of Denmark, 2001.

[D21] Jesse Levinson and Sebastian Thrun. "Unsupervised Calibration for Multi-beam Lasers". In: *Experimental Robotics*. Ed. by Oussama Khatib, Vijay Kumar, and Gaurav Sukhatme. Vol. 79. Springer Tracts in Advanced Robotics. Berlin, Heidelberg: Springer Berlin Heidelberg, 2014, pp. 179–193. ISBN: 978-3-642-28571-4. DOI: 10.1007/978-3-642-28572-1. URL: http://link.springer.com/10.1007/978-3-642-28572-1.

[D22] Eric L. Morris. *Lidar vs. LiDAR vs. LIDAR vs. LADAR: Letter Case Matters*. 2014. URL: https://geozoneblog.wordpress.com/2014/04/09/lidar-case-matters/.

[D23] P. Newman and J. Leonard. "Pure range-only sub-sea SLAM". In: *2003 IEEE International Conference on Robotics and Automation* 2 (2003), pp. 1921–1926. ISSN: 1050-4729. DOI: 10.1109/ROBOT.2003.1241875.

[D24] Gordon Petrie and Charles K. Toth. "Introduction to Laser Ranging, Profiling, and Scanning". In: *Topographic Laser Ranging and Scanning* (2008), pp. 1–27. DOI: 10.1201/9781420051438.ch1. URL: http://dx.doi.org/10.1201/9781420051438.ch1.

[D25] H. E. RAUCH, C. T. STRIEBEL, and F. TUNG. "Maximum likelihood estimates of linear dynamic systems". In: *AIAA Journal* 3.8 (Aug. 1965), pp. 1445–1450. ISSN: 0001-1452. DOI: 10.2514/3.3166.

[D26] A.P. Scherbatyuk. "The AUV positioning using ranges from one transponder LBL". In: *'Challenges of Our Changing Global Environment'. Conference Proceedings. OCEANS '95 MTS/IEEE*. Vol. 3. IEEE, 1995, pp. 1620–1623. ISBN: 0-933957-14-9. DOI: 10.1109/OCEANS.1995.528728.

[D27] Gerald L. Smith, Stanley F. Schmidt, and Leonard A. McGee. *Application of Statistical Filter Theory to the Optimal Estimation of Position and Velocity on Board a Circumlunar Vehicle*. 1962. (Visited on 05/30/2015).

[D28] David Titterton. *Strapdown Inertial Navigation Technology, 2nd Edition*. IET, 2004, p. 558. ISBN: 0863413587.

[D29] Giancarlo Troni and Louis L. Whitcomb. "Experimental evaluation of new methods for in-situ calibration of attitude and doppler sensors for underwater vehicle navigation". In: *2011 IEEE/RSJ International Conference on Intelligent Robots and Systems*. IEEE, Sept. 2011, pp. 3722–3727. ISBN: 978-1-61284-456-5. DOI: 10.1109/IROS.2011.6094942.

[D30] Are B. Willumsen, Oddvar Hallingstad, and Bjørn Jalving. "Integration of range, bearing and doppler measurements from transponders into underwater vehicle navigation systems". In: *Oceans 2006* Dvl (2006). DOI: 10.1109/OCEANS.2006.306851.